Part IV
The Earth Supersystem

In order to gain a good working knowledge of the Earth and its processes, we need to understand the interaction not only between systems but also between and among the various scales of activity of the many systems.

Schneider (2000)

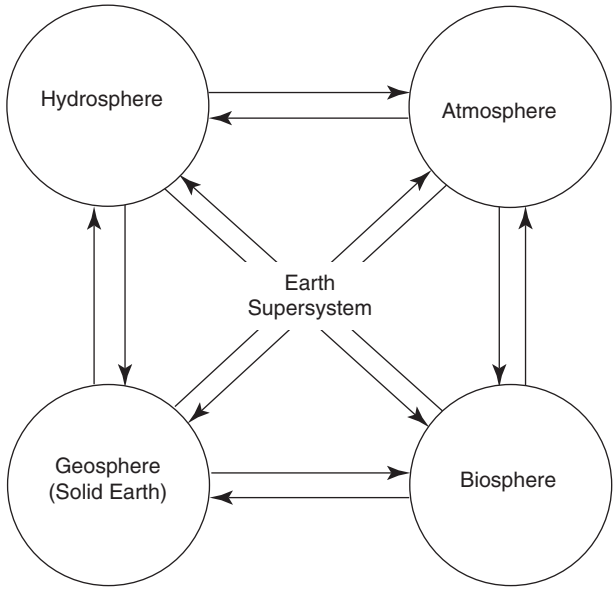

12 The Core–Mantle–Crust System

The questions of origin, composition and evolution of the Earth require input from astronomy, cosmochemistry, meteoritics, planetology, geology, petrology, mineralogy, crystallography, materials science and seismology, at a minimum. To a student of the Earth, these are artificial divisions, however necessary they are to make progress on a given front.

Anderson (1989)

A system is defined as a group of components (parts) that interact and function as a whole. A component can be a reservoir of matter (described by its mass and volume), a reservoir of energy (described by temperature, for example), an attribute of the system (such as body temperature or pressure), or a subsystem (such as the cardiovascular system, one of the interlinked subsystems of the human body) (Kump *et al*., 2004). The Earth may be viewed as a supersystem composed of four interacting systems: (i) the *geosphere* (or solid Earth), which is divisible into three major units – the core, mantle, and crust (see section 12.2.1); (ii) the *hydrosphere*, which comprises the various reservoirs of water, including ice; (iii) the *atmosphere*, the thin envelope of gases that surround the Earth; and (iv) the *biosphere*, which consists of all living organisms. In this chapter and the next we apply the principles we have learned in the previous chapters to understand some of the geochemical processes that have shaped the evolution of the various Earth systems to their current states.

We will start at the very beginning when the universe suddenly came into existence, and then discuss the origin of elements, the birth of the Solar System (including planet Earth), the differentiation of the Earth into mantle and core, the formation of the atmosphere and the oceans, and later addition of the crust. As geochemical interactions between mantle and crust occur largely through magmatism, we will briefly dwell on the processes of partial melting that generate magmas and crystallization of magmas that produce igneous rocks, and some techniques that can be used to infer the tectonic settings of ancient basaltic volcanic suites.

12.1 Cosmic perspective

The Earth is a very small part of the Solar System and only a tiny fraction of the universe, but it is a very special celestial body. In addition to being the planet we live on and the only entity in the universe with known life, the Earth has a unique composition. One of the fundamental factors that govern the Earth's geochemical processes and products is its composition on different scales. The unique composition of the Earth is a product of three sets of processes: the synthesis of elements (*nucleosynthesis*); the creation of the Solar System; and the formation and evolution of the Earth itself.

12.1.1 The Big Bang: the beginning of the universe

How and when did the universe come into existence? The most popular model at present for the origin of the universe is the *Big Bang theory*, which attributes the creation of the universe to very rapid (almost instantaneous), exponential expansion of an infinitely small, very hot, and infinitely dense phase. An analogy may the instantaneous expansion of an infinitely small balloon to the size of the universe, not an explosion like the bursting of a balloon, a common misconception. This event, in

Introduction to Geochemistry: Principles and Applications, First Edition. Kula C. Misra.

cosmological parlance, is known as a "singularity," a term used to describe the mind-boggling concept that an infinitely large amount of matter was gathered at a single point in space–time. Theoretical calculations by different authors indicate that this event occurred about 13 to 15 billion years ago. Prior to this event, nothing existed – not space, or time, or matter, or energy – and suddenly there was our universe, which had all of the mass and energy it contains today! We do not know where this dense starting material came from or why this "big bang" occurred. All that we can argue is that the model is compatible with three key astronomical observations as described below.

(1) Galaxies (massive, gravitationally bound systems consisting of stars, an interstellar medium of gas and dust, and dark matter) appear to be receding from the Earth. (The familiar Milky Way galaxy, to which our Solar System belongs, is only one of some 10^{11} galaxies, each ranging in size from 80,000 to 150,000 light years in diameter and containing in the order of 10^{11} stars. 1 light year is the distance light travels in a year $\approx 10^{13}$ km.) This expansion of the universe is documented by red-shifting of the light waves emitted from the galaxies, a consequence of the *Doppler effect*, the change in frequency and wavelength of a wave as perceived by an observer moving relative to the source of the wave (see Box 12.1).

Box 12.1 The Doppler effect

It is a familiar experience that the pitch of an ambulance's siren becomes higher as the vehicle moves towards you and then becomes lower as it moves past you. This change in pitch results from a shift in the frequency of sound waves as perceived by an observer when the source of the waves is moving relative to the observer. The phenomenon is known as the *Doppler effect* in honor of the Austrian mathematician–physicist Christian Doppler (1803–1853) who discovered it. As the ambulance approaches, the sound waves from its siren are compressed towards the observer and the intervals between waves diminish, which translates into an increase in frequency or pitch. As the ambulance moves away, the sound waves are stretched relative to the observer, causing the siren's frequency to decrease. This Doppler shift can also be described in terms of wavelength because of the inverse relationship between frequency and wavelength. It is possible to determine if the ambulance is approaching you or speeding away from you by the change in the siren's frequency (or wavelength), and to estimate the ambulance's speed from the rate of change of the frequency (or wavelength).

The Doppler effect is also recorded in the spectra of moving astronomical bodies that emit electromagnetic radiation. Light coming from stars and galaxies is *red-shifted* (i.e., it appears more red because the wavelengths are shifted towards the red end of the visible spectrum), indicating that they are receding from us. If the galaxies were moving towards us, the light emitted would be *blue-shifted* (i.e., it would appear more blue because of the shifting of the wavelengths towards the blue end of the visible spectrum). If they were stationery, there would be no shifting of wavelengths.

The recessional velocity of a galaxy, v (in km s^{-1}), can be calculated using *Hubble's Law*, so named after the American astronomer Edwin Hubble (1889–1953), who established the following linear relationship:

$$v = H_0 d \tag{12.1}$$

where d is the distance of the galaxy from the Earth in 10^6 light years, and H_0 is the *Hubble constant* (expressed in units of km s^{-1} per megaparsec; 1 megaparsec (Mpc) = 3.26 million light years). The direct proportionality between v and d – i.e., the greater the distance to a galaxy, the greater the red-shift in its spectral lines – indicates that farther galaxies are receding with higher velocities. The importance of the Hubble constant is that it expresses the rate at which the universe is expanding, from which it is possible to calculate the time when all galaxy trajectories would converge to the initial condition – the age of the universe. The value of H_0 is still being debated, but the accepted range lies between 64 to 72 (km/s)/Mpc. For $H_0 = 68$ (km/s)/Mpc, the age of the universe works out to be 13.4×10^9 years (Lineweaver, 1999), and for $H_0 = 71$ (km/s)/Mpc, the age is 13.7×10^9. How long the universe will continue to expand cannot be predicted without a more detailed knowledge about the objects in the universe.

(2) There is a pervasive presence of *cosmic background radiation* in the universe. This radiation, with a maximum wavelength of about 2 mm, which is in the microwave range of the electromagnetic spectrum, has all the characteristics of radiant heat, the same kind of radiant heat as emitted by a blackbody with a temperature of about 3 K. Some theoretical physicists had predicted the pervasive existence of such radiation if the universe began with a hot Big Bang. In 1965, Arno Penzias and Robert Wilson of the Bell Telephone Laboratories in New Jersey confirmed the prediction by documenting the existence of background cosmic radiation, which led to their sharing the Nobel prize in Physics in 1978.

By about 300,000 years after the Big Bang, the temperature of the universe had dropped sufficiently for protons and electrons to combine into hydrogen atoms ($p^+ + e^- \Rightarrow {}^1_1\mathrm{H}$), and the interaction between radiation and the background gas became ineffective; this background radiation has propagated freely over the entire universe ever since. The background radiation has been losing energy because its wavelength is stretched by the expansion of the universe, and its temperature has dropped to about 3 K, and will eventually cool to 0 K.

(3) The abundance of the light elements such as hydrogen and helium in the observable universe is consistent with the Big Bang model (see section 12.1.3).

12.1.2 Nucleosynthesis: creation of the elements

Nucleosynthesis is the process of creating new atomic nuclei from preexisting nucleons (protons and neutrons). Our understanding of nucleosynthesis is based on three sets of observations: (i) the abundance of elements (and their isotopes) in the cosmos; (ii) experimental data on the probability of specific nuclear reactions occurring under specified conditions; and (iii) inferences about the existence of appropriate sites for nucleosynthesis. The nucleosynthesis is believed to have occurred in four phases: (i) *Big Bang* (or *cosmogenic*) *nucleosynthesis* (BBN), which occurred immediately after the Big Bang; (ii) *stellar nucleosynthesis* in the interior of larger stars during the process of stellar evolution; (iii) *explosive nucleosynthesis* in supernovae; and (iv) *galactic nucleosynthesis* (*cosmic ray spallation*) in interstellar space. These processes are described below briefly; a detailed treatment of the topic can be found, for example, in Meyer and Zinner (2006).

Big Bang nucleosynthesis

Initially, the universe was very, very hot ($>10^{27}$ K). As the universe expanded, it cooled, and eventually matter formed and coalesced together by gravity to form various celestial bodies. After about 10^{-32} s of the Big Bang, the universe had expanded to 30 cm in diameter, but the pressure and temperature (10^{27} K) were still so high that matter existed only as a quark–gluon plasma, consisting of (almost) free quarks and gluons, which are the basic building blocks of matter. In 10^{-26} s, the universe had attained a size comparable to that of the Solar System, temperature had cooled to about 10^{13} K, and a radical transition led to the formation of protons and neutrons (within the first second after the Big Bang), which became the common state of matter. The temperature at this stage was too high for the formation of more complex matter.

Free neutrons and protons are less stable than helium nuclei. So they have a strong tendency to form ${}^4_2\mathrm{He}$, but the formation of ${}^4_2\mathrm{He}$ requires the formation of deuterium (${}^2_1\mathrm{H}$ or D) as an intermediate step. At very high temperatures, the mean energy per particle is greater than the binding energy of ${}^2_1\mathrm{H}$, so that any ${}^2_1\mathrm{H}$ nuclei formed would be immediately destroyed. However, the temperature of the universe dropped to about 10^9 K within 3 min of its beginning, and protons (p) and neutrons (n) began to react with each other to form deuterium nuclei(${}^2\mathrm{H}$ or D):

$$p + n \Rightarrow {}^2_1\mathrm{H} + \gamma \tag{12.2}$$

It took about 300,000 years after the Big Bang for the universe to cool to about 3000 K, cool enough for electrons to be bound to nuclei, forming whole H and He atoms, and for photons to separate from matter causing light to burst forth for the first time. Further reactions such as those listed below produced tritium (${}^3_1\mathrm{H}$), the radioactive isotope of hydrogen, along with the isotopes of helium, ${}^3_2\mathrm{He}$ and ${}^4_2\mathrm{He}$:

$${}^2_1\mathrm{H} + n \Rightarrow {}^3_1\mathrm{H} + \gamma \tag{12.3}$$

$${}^3_1\mathrm{H} + p \Rightarrow {}^4_2\mathrm{He} + \gamma \tag{12.4}$$

$${}^2_1\mathrm{H} + p \Rightarrow {}^3_2\mathrm{He} + \gamma \tag{12.5}$$

$${}^3_2\mathrm{He} + n \Rightarrow {}^4_2\mathrm{He} + \gamma \tag{12.6}$$

Although ${}^4_2\mathrm{He}$ continues to be produced by other mechanisms (such as stellar fusion and α decay), and trace amounts of ${}^1_1\mathrm{H}$ by *spallation* (an atomic nucleus splitting into three or more fragments due to interaction with energetic particle) and certain types of radioactive decay (proton emission and neutron emission), the abundances of these light isotopes (${}^1_1\mathrm{H}$, ${}^2_1\mathrm{H}$, ${}^3_2\mathrm{He}$, and ${}^4_2\mathrm{He}$) in the universe are believed to have been determined primarily by the Big Bang nucleosynthesis. A few helium nuclei also combined into heavier nuclei, producing trace amounts (on the order of 10^{-10}%) of Li, Be, and B (Meyer and Zinner, 2006). No heavier elements could be formed because of the very short duration of the Big Bang nucleosynthesis, which came to an end when, due to continued expansion and cooling of the universe, its temperature and density fell below what was required for nuclear fusion. Any free neutrons decayed away because neutrons outside the nucleus are unstable (having a half-life of only 10 min). Thus, the Big Bang created only two elements in any abundance, hydrogen and helium, and trace amounts of three very light elements, lithium, beryllium, and boron. The agreement between the abundance observed and that predicted by theoretical calculations is good for ${}^4_2\mathrm{He}$, and even better for ${}^3_2\mathrm{He}$ and ${}^2_1\mathrm{H}$ (whose abundances can be measured with greater accuracy). The predicted and observed values, however, differ by a factor of two for ${}^7_3\mathrm{Li}$, most likely because of the uncertainties in the reconstruction of the primordial ${}^7_3\mathrm{Li}$ abundance. Elements formed during this time were in the plasma state and did not cool to the state of neutral atoms until much later. Carbon (${}^{12}_6\mathrm{C}$) and elements with atomic numbers greater than that of carbon came into existence only after the formation of stars by various nuclear processes in their hot interiors.

Stellar nucleosynthesis

Stellar nucleosynthesis occurs in stars during the process of stellar evolution. Inhomogeneities in the hot gas, which was the state of the universe for quite some time after the Big Bang, led to the formation of proto-galaxies (perhaps about 0.5 Gyr after the Big Bang) through a process of gravitational attraction and collapse, and collapse due to instabilities within the proto-galaxies led to the formation of stars.

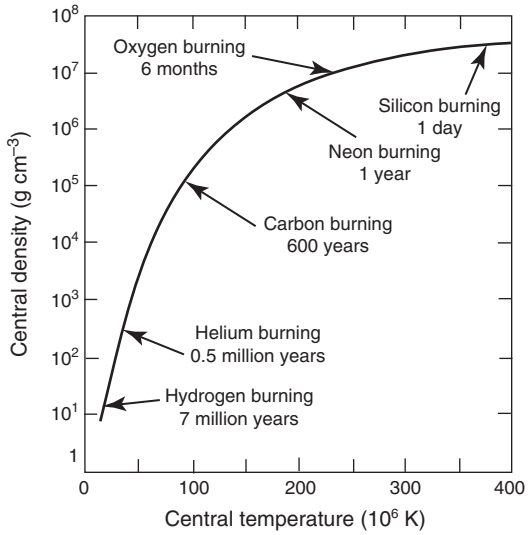

Fig. 12.1 Evolutionary path of the core of a massive star of 25 solar masses (after Bethe and Brown, 1985). The period spent in each step of the nuclear fusion process depends on the mass of the star; more massive stars would evolve more rapidly. For most of the star's lifetime the primary energy source is the fusion of hydrogen nuclei to form helium. The final stage of silicon fusion yields a core of iron, from which no further energy can be extracted by nuclear reactions. The iron core cannot resist gravitational collapse, leading to a supernova explosion.

Table 12.1 Successive stages of stellar nucleosynthesis.

Process	Approximate duration	Fuel for the process	Important products
Hydrogen burning	7×10^6 yr	H	$^4_2$He, $^{14}_7$N, $^{17}_8$O, $^{26}_{13}$Al
Helium burning	0.5×10^6 yr	He	$^{12}_6$C, $^{16}_8$O, $^{18}_8$O, $^{22}_{10}$Ne, $^{25}_{12}$Mg, *s-process* isotopes*
Carbon burning	600 yr	C	$^{20}_{10}$Ne, $^{23}_{11}$Na, $^{24}_{12}$Mg
Neon burning	1 yr	Ne	$^{16}_8$O, $^{24}_{12}$Mg
Oxygen burning	6 months	O	$^{28}_{14}$Si, $^{31}_{15}$P, $^{32}_{16}$S
Silicon burning	1 day	Mg to Si	Fe–peak isotopes; $^{56}_{26}$Fe, $^{54}_{26}$Fe

*Isotopes formed by nucleosynthesis involving slow capture of neutrons.
Source of data: Bethe and Brown (1985) and Meyer and Zinner (2006).

Subsequent nucleosynthesis of elements (from carbon to nickel) occurred primarily within the core regions of stars that pre-dated the Solar System, either by nuclear fusion or by nuclear fission operating in different environments and at different times, with hydrogen as the sole starting material. This view of nucleosynthesis, called the *polygenetic hypothesis*, which can account for the observed abundances of the elements in the Solar System and in nearby stars, was first proposed by E.M. Burbridge, G.R. Burbridge, W.A. Fowler, and F. Hoyle (1957) in a classic paper commonly referred to as B^{2}FH. A strong argument in favor of this hypothesis is the fact that such nuclear transformations are currently taking place inside stars in the course of their evolution. The successive nuclear fusion processes, each of which occurs inside stars at specific temperatures, are referred to as *hydrogen burning*, *helium burning*, *carbon burning*, *neon burning*, *oxygen burning*, and *silicon burning* (Fig. 12.1; Table 12.1), the ashes from one burning stage providing the fuel for the next and the conversion of gravitational energy into thermal energy providing the automatic temperature rise. Several of these reactions may occur simultaneously in the core and outer shell of a massive star, resulting in a core of different composition compared to its outer shell. Moreover, every star does not experience all of these nuclear reactions; that is why other stars in the Milky Way galaxy do not have the same composition as the Sun. The above mentioned fusion processes are able to create elements up to iron ($Z = 26$) and nickel ($Z = 28$), the region of the isotopes having the highest binding energy per nucleon. Heavier elements can be synthesized within stars by processes involving neutron capture. The products of stellar nucleosynthesis are generally distributed into the universe as planetary nebulae or through the *solar wind* (streams of high-energy atomic particles).

Hydrogen burning. In hydrogen burning, which starts when the gravitational collapse of a star has proceeded to the point where density reaches 6 g cm^{-3} and temperature reaches 10×10^6 to 20×10^6 K, fusion of protons forms $^4_2$He (see Box 12.2). Much of the helium produced is consumed in later stages of stellar evolution or is locked up in stars of lower masses that never reach the temperature required for helium burning. In stars of 1.2 or less solar masses (M_0), this process occurs via the proton–proton chain, the only source of nuclear energy for the first-generation stars that formed from the primordial mixture of hydrogen and helium after the Big Bang. Some stars run through their evolution relatively rapidly (in millions of years) and produce nearly all the heavier elements by various nuclear processes in their hot interiors. The life of such stars ends in a gigantic explosion as a supernova when it runs out of nuclear fuel. The core collapses in milliseconds, and the subsequent "bounce" of the core generates a shock wave so intense that it blows off most of the star's mass (Bethe and Brown, 1985). The newly formed elements within the star are expelled into the interstellar medium, where they are mixed with interstellar gas and ultimately incorporated into next-generation stars. The material in the Milky Way galaxy underwent several such cycles before our Solar System was born.

In more massive, second and higher generation stars, in which the central temperatures exceed 2×10^7 K and which contain carbon ($^{12}_6$C) synthesized by ancestral stars, hydrogen burning is also accomplished via another process, the

Box 12.2 Nuclear reactions associated with hydrogen burning

The net result of hydrogen burning (or fusion of protons) is the production of helium, which can be accomplished by the following two mechanisms:

(1) Proton–proton chain (Burbridge *et al.*, 1957)

$$^{1}_{1}\mathrm{H} + {}^{1}_{1}\mathrm{H} \Rightarrow {}^{2}_{1}\mathrm{H} + \beta^{+} + \nu\,(\text{neutrino}) + 0.422\,\text{MeV} \quad (12.7)$$

$$\beta^{+} + \beta^{-} \Rightarrow 1.02\,\text{MeV}\,(\text{annihilation}) \quad (12.8)$$

$$^{2}_{1}\mathrm{H} + {}^{1}_{1}\mathrm{H} \Rightarrow {}^{3}_{2}\mathrm{He} + \gamma + 5.493\,\text{MeV} \quad (12.9)$$

$$^{3}_{2}\mathrm{He} + {}^{3}_{2}\mathrm{He} \Rightarrow {}^{4}_{2}\mathrm{He} + {}^{1}_{1}\mathrm{H} + {}^{1}_{1}\mathrm{H} + 12.859\,\text{MeV} \quad (12.10)$$

(2) CNO cycle (Bethe, 1968)

$$^{12}_{6}\mathrm{C} + {}^{1}_{1}\mathrm{H} \Rightarrow {}^{13}_{7}\mathrm{N} + \gamma \quad (12.11)$$

$$^{13}_{7}\mathrm{N} \Rightarrow {}^{13}_{6}\mathrm{C} + \beta^{+} + \nu \quad (12.12)$$

$$^{13}_{6}\mathrm{C} + {}^{1}_{1}\mathrm{H} \Rightarrow {}^{14}_{7}\mathrm{N} + \gamma \quad (12.13)$$

$$^{14}_{7}\mathrm{N} + {}^{1}_{1}\mathrm{H} \Rightarrow {}^{15}_{8}\mathrm{O} + \gamma \quad (12.14)$$

$$^{15}_{8}\mathrm{O} \Rightarrow {}^{15}_{7}\mathrm{N} + \beta^{+} + \nu \quad (12.15)$$

$$^{15}_{7}\mathrm{N} + {}^{1}_{1}\mathrm{H} \Rightarrow {}^{12}_{6}\mathrm{C} + {}^{4}_{2}\mathrm{He} \quad (12.16)$$

The end result is that four $^{1}_{1}$H nuclei fuse to form one nucleus of $^{4}_{2}$He and release a large amount of energy. Note that the nucleus of $^{12}_{6}$C works as a sort of catalyst, so it can be used again and again for starting fresh CNO cycles. The C-cycle reaction also provides a mechanism for the production of $^{14}_{7}$N in the star.

carbon–nitrogen–oxygen (CNO) cycle (Bethe, 1968; see Box 12.2). Most stars in the Milky Way galaxy, including the Sun, are at least second-generation stars because only the very small first-generation stars could have survived in this very old galaxy. At present, the Sun is burning only hydrogen, but it contains heavier elements inherited from earlier-generation stars. The energy released as a result of the conversion of hydrogen to helium is the source of the Sun's temperature and luminosity.

When the hydrogen fuel is exhausted in the core region of the star, hydrogen fusion is switched to a shell outside the core. This is the *red giant* phase of a star's evolution. Helium produced by hydrogen fusion cannot be burned immediately due to the larger nuclear charge of helium, which produces a much higher Coulomb barrier against fusion. So, the helium accumulates in the core, increasing its density and causing it to contract and get hotter. The increase in the core temperature results in an expansion of the envelope and a lowering of the surface temperature, which causes the color to turn red. How soon this would happen depends on the mass of the star.

Helium burning. Helium burning begins in a star if it is massive enough for temperatures to reach 10^{8}K and the core density to reach 10^{4}g cm^{-3}. The critical reaction in this stage is the triple-alpha process in which three $^{4}_{2}$He nuclei (i.e., three α particles) fuse to form the nucleus of $^{12}_{6}$C through $^{8}_{4}$Be as a very unstable intermediate product (half-life of $^{8}_{4}$Be = 10^{-16} s):

$$^{4}_{2}\mathrm{He} + {}^{4}_{2}\mathrm{He} \Rightarrow {}^{8}_{4}\mathrm{Be} \quad (12.17)$$

$$^{8}_{4}\mathrm{Be} + {}^{4}_{2}\mathrm{He} \Rightarrow {}^{12}_{6}\mathrm{C} + \gamma \quad (12.18)$$

Another important product of helium burning is $^{16}_{8}$O by the reaction:

$$^{12}_{6}\mathrm{C} + {}^{4}_{2}\mathrm{He} \Rightarrow {}^{16}_{8}\mathrm{O} \quad (12.19)$$

At this point in a star's evolution, the $^{1}_{1}$H has been converted to $^{4}_{2}$He, and the $^{4}_{2}$He into $^{12}_{6}$C and $^{16}_{8}$O with the accumulation of some $^{14}_{7}$N. Other isotopes that can be produced by helium burning include $^{18}_{8}$O, $^{22}_{10}$Ne, and $^{25}_{12}$Mg. Helium burning is the key to the synthesis of all elements beyond helium, and probably is responsible for much of the cosmic abundance of $^{12}_{6}$C, although in more massive stars the later burning stages consume some of this $^{12}_{6}$C.

In contrast to massive stars that became supernovae in a few millions of years, stars with mass less than ~8 M_0 take hundreds of millions to billions of years to burn the H and He in their interior to C and O. When available helium is exhausted, the evolution of low-mass stars, such as the Sun, ends after the red giant phase because the gravitational force is not sufficient to overcome Coulomb repulsion of electrons. Nuclear reactions cease, the star simply contracts and its exterior heats up. The star becomes extremely hot, a *white dwarf* (commonly composed of C and O). In the absence of further fusion reactions, a white dwarf eventually cools off to become a *black dwarf* (a burned out chunk of carbon!). White dwarfs comprise approximately 6% of all known stars in the solar neighborhood. It is believed that over 97% of all stars in our galaxy would eventually turn into white dwarfs. This is the likely fate of our Sun in about 5 Gyr.

Carbon burning. In stars with an initial mass of at least 8 solar masses, gravitational contraction of the star's core can generate temperatures in excess of 5×10^{8} K. At such high temperatures it is possible to overcome the Coulomb repulsion barrier between two $^{12}_{6}$C nuclei and fuse them to form $^{24}_{12}$Mg* (an excited nucleus of $^{24}_{12}$Mg, which has higher energy compared to its energy in the ground state, the state of minimum energy):

$$^{12}_{6}\mathrm{C} + {}^{12}_{6}\mathrm{C} \Rightarrow {}^{24}_{12}\mathrm{Mg}^{*} \quad (12.20)$$

This represents the carbon burning stage in the evolution of a star. $^{24}_{12}$Mg* decays mostly to $^{20}_{10}$Ne (Meyer and Zinner, 2006, p. 73):

$$^{24}_{12}\text{Mg}^* \Rightarrow {}^{20}_{10}\text{Ne} + {}^{4}_{2}\text{He} \tag{12.21}$$

Thus, carbon burning is the major producer of $^{20}_{10}$Ne in the universe. A number of other less abundant nuclei (including those of Na, Al, P, S, and K) are also synthesized at this stage, and in the subsequent process.

Neon burning. Neon burning, which follows carbon burning and typically occurs at temperatures near 1.5×10^9 K, lasts for a very short duration. It involves disintegration of $^{20}_{10}$Ne ($^{20}_{10}\text{Ne} + \gamma \Rightarrow {}^{16}_{8}\text{O} + {}^{4}_{2}\text{He}$) and recapture of the a particle so liberated to produce $^{24}_{12}$Mg ($^{20}_{10}\text{Ne} + 24\text{He} \Rightarrow {}^{24}_{12}\text{Mg} + \gamma$). Thus, the net reaction in neon burning is

$$^{20}_{10}\text{Ne} + {}^{20}_{10}\text{Ne} \Rightarrow {}^{16}_{8}\text{O} + {}^{24}_{12}\text{Mg} \tag{12.22}$$

Oxygen burning. The neon burning stage is followed by oxygen burning at temperatures in excess of about 10^8 K. The main products of oxygen burning are $^{28}_{14}$Si, $^{31}_{15}$P, and $^{32}_{16}$S via $^{32}_{16}$S* (an excited nucleus of $^{32}_{16}$S) as an intermediate product:

$$^{16}_{8}\text{O} + {}^{16}_{8}\text{O} \Rightarrow {}^{32}_{16}\text{S}^* \tag{12.23}$$

$$^{32}_{16}\text{S}^* \Rightarrow {}^{28}_{14}\text{Si} + {}^{4}_{2}\text{He} \Rightarrow {}^{31}_{15}\text{Si} + {}^{1}_{1}\text{H} \Rightarrow {}^{32}_{16}\text{S} + \gamma \tag{12.24}$$

Nuclei of masses up to $A = 40$ may be produced by oxygen fusion through the capture of proton, neutron, and α particles, but at the end of the oxygen burning, the matter in the stellar core is dominated by $^{28}_{14}$Si and $^{32}_{16}$S.

Silicon burning. Silicon burning commences when the temperatures and densities inside the star exceed about 3×10^9 K and 10^7 g cm^{-3}, respectively. It lasts for a week or less, depending on the mass of the star. The mechanism for silicon burning is more complicated than that for the previous stages because the high charges of the Si and S isotopes prevent them from interacting directly. Photodisintegration of $^{28}_{14}$Si nuclei and other intermediate-mass nuclei around $A = 28$ produces an abundant supply of protons, neutrons, and α particles, which are captured by the nuclei left from previous burning stages to produce new nuclei up to $A = 56$ (i.e., $^{56}_{28}$Ni). However, $^{56}_{28}$Ni is unstable and it decays quickly to $^{56}_{27}$Co (half-life of $^{56}_{28}$Ni = 6.075 days), and then to stable $^{56}_{26}$Fe (half-life of $^{56}_{27}$Co = 77.27 days), which has the highest binding energy per nucleon. This is the reason for the relatively high solar abundances of the iron group elements (see Fig. 12.4). The relevant reactions are (Meyer and Zinner, 2006):

$$^{28}_{14}\text{Si} + {}^{28}_{14}\text{Si} \Rightarrow {}^{54}_{26}\text{Fe} + 2{}^{1}_{1}\text{H} \tag{12.25}$$

$$^{28}_{14}\text{Si} + {}^{28}_{14}\text{Si} \Rightarrow {}^{56}_{28}\text{Ni} \tag{12.26}$$

$$^{56}_{28}\text{Ni} \Rightarrow {}^{56}_{27}\text{Co} + e^+ + \nu \tag{12.27}$$

$$^{56}_{27}\text{Co} \Rightarrow {}^{56}_{26}\text{Fe} + e^+ + \nu \tag{12.28}$$

Nuclear statistical equilibrium. Iron ($^{56}_{26}$Fe) is something of a dead end of stellar fusion in the sense that fusion reactions that build elements up to iron release energy, whereas fusion reactions for the formation of elements with atomic numbers higher than that of iron actually consume energy. Thus, whereas small amounts of elements heavier than iron (e.g., gold, silver, uranium, etc.) are formed in stars, their abundances in the Solar System are very low. When increasing temperature at the core of a star brings the chain of nuclear fusion reactions to this dead end, disintegrative as well as constructive nuclear reactions begin to occur among the iron group nuclei ($^{51}_{23}$V, $^{52}_{24}$Cr, $^{55}_{25}$Mn, $^{56}_{26}$Fe, $^{59}_{27}$Co, $^{59}_{28}$Ni), leading to a *nuclear statistical equilibrium;* the relative abundances of iron group elements reflect this steady state.

Heavier elements can be synthesized within stars by a neutron capture process known as the *s process* or in the explosive environments, such as supernovae, by a number of processes. Some of the more important of these include: the *r process*, which involves rapid captures of neutrons; the *rp process*, which involves rapid captures of protons; and the *p process*, which involves photodisintegration of existing nuclei.

s process. Nuclides heavier than the iron group form by the capture of neutrons, the product of earlier helium burning reactions in stellar interiors (the main neutron source reactions being $^{13}_{6}\text{C} + {}^{4}_{2}\text{He} \Rightarrow {}^{16}_{8}\text{O} + n$ and $^{22}_{10}\text{Ne} + {}^{4}_{2}\text{He} \Rightarrow {}^{25}_{12}\text{Mg} + n$) by the iron group seed nuclei ($^{51}_{23}$V, $^{52}_{24}$Cr, $^{55}_{25}$Mn, $^{56}_{26}$Fe, $^{59}_{27}$Co, $^{59}_{28}$Ni). Neutrons being electrically neutral particles are not affected by the Coulomb repulsion that inhibits reactions involving charged particles. The capture of one neutron by a nucleus increases its neutron number by one unit, producing the next heavier isotope of the original element. If the resulting nucleus is unstable, it tends to undergo β^- decay (i.e., it emits an electron, and one neutron is effectively transformed into a proton) to form a more stable nucleus (an isobar). The neutron number stays the same as that of the original element, but the number of protons (i.e., the atomic number, Z), increases by one because of the transformation of the captured neutron into a proton (see Table 10.1). If the resulting nucleus is stable, there will be no immediate β^- decay. However, when successive neutron captures producing successively heavier isotopes of the original element result in too high a neutron: proton ratio in the nucleus, it would undergo β^- decay to form a more stable nucleus (an isobar) as in the previous case. The two dominant tracks of neutron addition are the slow *s* process and the rapid *r* process (Fig. 12.2), which occur during the final stages of the evolution of red giants.

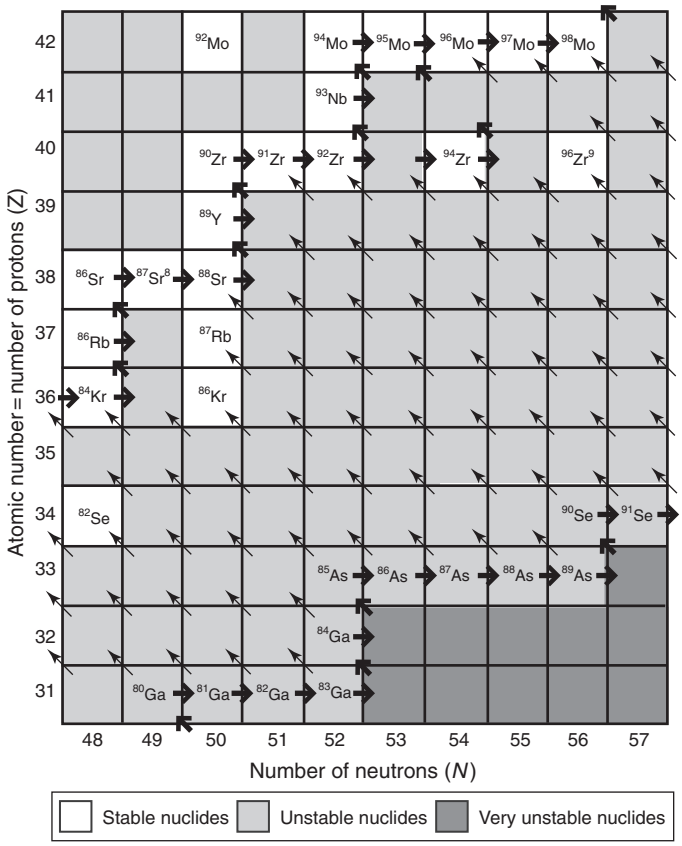

Fig. 12.2 A portion of the nuclide chart illustrating how the *s* process (upper set of arrows) and *r* process (lower set of arrows) form new heavy nuclides by neutron capture and subsequent β decay. In the *s* process, neutron additions (indicated by thick horizontal arrows) move the nucleus rightward on the chart until it is transformed into a neutron-rich unstable nuclide. The unstable nuclide undergoes β decay (indicated by thick diagonal arrows), which shifts it up and to the left, producing an isotope of a different chemical element. The nucleus can then capture additional neutrons until it β decays again, and so forth. In the *r* process, rapid addition of neutrons (rapid compared to the half-lives of nuclides represented by the light gray boxes) creates a chain of neutron-rich unstable nuclides. When neutron addition moves a nucleus into one of the dark gray boxes (very unstable nuclides), it β decays on a time scale even shorter than the duration of a supernova event. When the supernova neutron addition ends, the unstable nuclides left along the *r* process track quickly β decay (thin diagonal arrows) until they become stable nuclides (represented by white boxes). (After J.A. Wood, *The Solar System,* 1st edition, Copyright © 1979, Figure 6-20, p. 152. Used with permission of Pearson Education, Inc., Upper Saddle River, NJ.)

The *s* process occurs at relatively low neutron density and intermediate temperature conditions in stars. It involves slow (relative to the rate of radioactive β^- decay) addition of neutrons until an excess number of neutrons produces an unstable nuclide, which then undergoes β^- decay to form a stable, heavier nuclide. For example, the nucleus of $^{62}_{28}$Ni absorbs a neutron changing it to an excited nucleus of $^{63}_{28}$Ni, which then gets deexcited by emitting a γ-ray, and the radioactive $^{63}_{28}$Ni decays to stable $^{63}_{29}$Ni by emitting a β^- particle (Faure, 1998):

Neutron capture by $^{62}_{28}$Ni: $\quad {}^{62}_{28}\text{Ni} + n \Rightarrow {}^{63}_{28}\text{Ni} + \gamma$

Beta decay of radioactive $^{63}_{28}$Ni:

$$^{63}_{28}\text{Ni} \Rightarrow {}^{63}_{29}\text{Cu} + \beta^- + \bar{\nu} + 0.0659\,\text{MeV} \qquad (12.29)$$

The net result is the production of $^{63}_{29}$Cu from $^{62}_{28}$Ni by neutron capture. $^{63}_{29}$Cu, a stable isotope of copper, can then capture another neutron to form $^{64}_{29}$Cu, and repetition of the process described above would produce other heavy elements. Given enough neutrons, the *s* process can synthesize the majority of the isotopes in the range $23 \le A \le 46$ and a considerable proportion of the isotopes in the range $63 \le A \le 209$ (α decay prevents further nucleosynthesis by neutron capture), and account for abundance peaks at $A = 90$, 138, and 208. Note that a helium burning star producing heavy elements by the *s* process would have to be at least a second generation star with the iron group nuclides inherited from an earlier-generation star.

Explosive nucleosynthesis

A *supernova* (an exploding massive star) begins with the collapse of a stellar core, from a radius of several thousand kolometers to a radius of 100 km or so in a few tenths of a second. When matter in the central region of the core is compressed beyond the density of nuclear matter (3×10^{14}g cm^{-3}), it rebounds, sending a massive shock wave outward. The temperature increase that results from the compression produces a breakdown of existing nuclei by photodisintegration, for example,

$$^{56}_{26}\text{Fe} + \gamma \Rightarrow 13\ {}^{4}_{2}\text{He} + 4n \qquad (12.30)$$

$$^{4}_{2}\text{He} + \gamma \Rightarrow 2\ {}^{1}_{1}\text{H} + 2n \qquad (12.31)$$

The destruction of nuclei that had taken millions of years to build may be viewed as a backward step, but the large number of neutrons and protons produced by photodisintegration leads to three additional processes of nucleosynthesis: the *r* process (rapid process of neutron capture); the *rp* process (rapid capture of free protons); and the so-called *p* process. As the shock wave traverses the outer layers of the star, it compresses and heats them. This initiates explosive helium burning, oxygen burning, and silicon burning in these stellar shells, thereby modifying the composition established in the presupernova burning phase. These processes produce isotopes of S, Cl, Ar, Ca, Ti, and Cr, and some Fe.

The *r* process occurs when a large burst of neutrons, such as that released during the 1 to 100 s of peak temperature during a supernova explosion, allows rapid neutron capture, and immediate transformation of nuclides by β decay. At the end

of the supernova event, nuclides formed by the *r* process transform more slowly by successive β decays to more stable nuclides. An example is the rapid capture of 5 neutrons in succession by $^{65}_{29}$Cu to form $^{70}_{29}$Cu, which then decays by β^- emission to stable $^{70}_{29}$Cu:

Rapid capture of 5 neutrons by $^{65}_{29}$Cu: $^{65}_{29}\text{Cu} + 5n \Rightarrow {}^{70}_{29}\text{Cu} + 5\gamma$

Beta decay of radioactive $^{70}_{29}$Cu: $^{70}_{29}\text{Cu} \Rightarrow {}^{70}_{30}\text{Zn} + \beta^- + \bar{\nu} +$ ~7.2 MeV (12.32)

The *r* process is responsible for the production of a large number of isotopes in the range $70 \leq A \leq 209$, and also for the synthesis of uranium and thorium, as well as of the most neutron-rich isotopes of each heavy element. Many of these isotopes can also be synthesized by the *s* process, but some isotopes, such as ^{86}Kr, ^{87}Rb, and ^{96}Zr, can form only by the *r* process.

A number of proton-rich heavy isotopes (e.g., $^{74}_{32}$Se, $^{195}_{78}$Pt, $^{173}_{70}$Yb) cannot be created by neutron capture on any scale. There are two ways to increase the ratio of protons to neutrons in an atomic nucleus: either add protons or subtract neutrons. The *rp* process consists of consecutive proton addition to seed nuclei, and requires a H-rich environment (i.e., a large proton flux) as well as a very high temperature ($> 10^9$ K) to overcome the large Coulomb barrier. The process is inhibited by α decay, which puts an upper limit of ^{105}Te as the end point.

The *p* process, as it is now understood, is a misnomer because it has nothing to do with proton capture, as the term seems to imply (Meyer and Zinner, 2006, p. 78). Actually, the so-called *p* process operates through the mechanism of photodisintegration, which occurs when γ-rays strip off first neutrons and then protons and α particles from preexisting *r*- and *s*-process isotopes. This is why the *p* process is sometimes referred to as the γ process. Proton capture, which must overcome Coulomb repulsion, is less probable than neutron capture and thus less effective. The *p* process is significant only for those nuclei that cannot be produced by other mechanisms, and the abundances of elements created by the *p* process only (e.g., $^{168}_{70}$Yb, $^{174}_{72}$Hf, $^{180}_{73}$Ta) tend to be low.

Cosmic ray spallation

Stellar and explosive nucleosynthesis do not produce the lighter elements such as Li, Be, and B; these elements are produced continually by cosmic ray spallation. Cosmic ray spallation (CRS) refers to the fragmentation of carbon, oxygen, and nitrogen nuclei in the interstellar medium by *cosmic rays* (fast-moving high energy particles, such as α particles ($^4_2$He) and protons ($^1_1$H), which are abundant in the interstellar gas). These reactions occur at high energies (higher than the Big Bang and stellar interiors), but at low temperatures, and are responsible for all of some of the lightest isotopes (such as $^3_2$He, $^6_3$Li, $^9_4$Be, $^{10}_5$B, $^{11}_5$B, and some of $^7_3$Li, but not $^2_1$H).

12.1.3 The Solar System

The Solar System is part of the Milky Way galaxy, which contains probably more than 10^{11} stars and has a lens-like form with a diameter of about 100,000 light years and a thickness of 1000 light years. The Solar System is comprised of the Sun, which contains > 99.86% of the mass of the system and those celestial objects bound to it by gravity, all of which were formed from the collapse of a much larger molecular cloud approximately 4.6 Ga. The temperature in the Sun ranges from 15.6×10^6 K at the core to 5800 K at the surface, and the pressure at the core is 250 billion atm. It is composed almost entirely of hydrogen (70%) and helium (28%).

The celestial bodies bound to the Sun by gravity include: 8 planets – which, in order of increasing distance from the Sun, are Mercury, Venus, Earth, Mars, Jupiter, Saturn, Uranus, and Neptune (Table 12.2) – and their satellites; at least five dwarf planets; an asteroid belt between Mars and Jupiter; the Kuiper belt containing a large number of small celestial bodies; meteoroids; comets; and interplanetary dust. A fundamental

Table 12.2 Some data about the Sun and the planets in the Solar System.

Planet/ Sun	Planet type	Equatorial diameter (km)	Distance from the Sun (10^6 km)	Relative mass* (kg)	Average density (g cm^{-1})	Composition	Principal atmospheric constituents
Mercury	Terrestrial	4,878	57.9	0.06	5.4	Iron/rocky	No atmosphere
Venus		12,104	108.2	0.82	5.2	Rocky	CO_2, N_2, Ar
Earth		12,756	149.6	1.00	5.5	Rocky	N_2, O_2, Ar
Mars		6,794	227.9	0.11	3.9	Rocky	CO_2, N_2, Ar
Jupiter	Jovian	142,984	778.3	317.87	1.3	Gassy	H, He
Saturn		120,536	1,426.9	95.14	0.7	Gassy	H, He
Uranus		51,118	2,871.0	14.56	1.2	Gassy/icy	H, He, CH_4
Neptune		49,528	4,497.1	17.21	1.7	Gassy/icy	H, He, CH_4
Sun		1.39×10^6		1.99×10^{30}	1.4	H 70% He 28%	No atmosphere

*Normalized to the mass of the Earth = 6.0×10^{24} kg.

difference between the stars, such as the Sun, and planets, such as the Earth, is that stars have a high-temperature core capable of generating their own energy by nuclear reactions, whereas planets have no such self-sustaining energy source. As a result, a star is seen because it generates its own light, but a planet is visible by virtue of the light from a nearby bright star reflected off its surface.

The planets may be divided into two major groups in terms of composition: *terrestrial planets* (Mercury, Venus, Earth, and Mars); and *Jovian planets* (Jupiter, Saturn, Uranus, and Neptune). The terrestrial planets (also classified as inner planets) are characterized by relatively small size (< 13,000 km in equatorial diameter), proximity to the Sun, high-density (3.9–5.5 g cm^{-3}), and earth-like rocky composition (about 90% composed of Fe, Si, Mg, and O). The Jovian planets (also classified as *outer planets* or *gas giants*), in contrast, are large bodies (> 49,000 km in equatorial diameter) of much lower density (0.7–1.7 g cm^{-3}), composed of gases (mostly H and He, like the Sun) and positioned at much greater distances from the Sun. The Earth is unique among the planets in having an oxygen-rich atmosphere, plenty of liquid water, and life. Pluto, previously considered a planet, is now classified as a *dwarf planet* belonging to the Kuiper belt, which is a region of the Solar System beyond the planets, extending from the orbit of Neptune (at 30 AU) to approximately 55 AU from the Sun, and appears to be composed of left-over material from planetary formation. (1 AU (*astronomical unit*) is a unit of length based on the mean distance between the Earth and the Sun = 149.6×10^6 km). A dwarf planet is a celestial body orbiting the Sun and massive enough to acquire a spherical shape by its own gravity, but which has not cleared its neighboring region of planetesimals and is not a satellite. The International Astronomical Union (IAU) currently recognizes only five dwarf planets – Pluto, Eris, Ceres, Haumea, and Makemake – but many more are suspected to exist in the Kuiper belt.

The asteroids comprise a group of relatively small celestial bodies that orbit around the Sun. They range up to about 1000 km in diameter, but most of the 50,000 or so asteroids that have been observed are only about 1 km across, and are fragments of once larger bodies. Asteroids are believed to have accreted shortly after the beginning of the Solar System's history and represent remnants of the proto-planetary disc in the region where perturbations by Jupiter prevented the accretion of planetary materials into planets or a large planet. The Kuiper belt is similar to the asteroid belt, although it is 20 times as wide and 20–200 times as massive and located outboard of the planets. Also, whereas the asteroid belt is composed primarily of rock and metal, the Kuiper belt objects are composed largely of frozen volatiles (usually referred to as "ices") such as methane, ammonia, and water.

Meteoroids are sand- to boulder-sized particles of debris, smaller than asteroids but larger than interplanetary dust. Comets, the most spectacular and unpredictable bodies in the solar system, measuring a few kilometers to tens of kilometers across, are composed of frozen gases (ammonia, methane, carbon dioxide, and carbon monoxide) that hold together pieces of rocky and metallic materials. Comets orbit the Sun and, when close enough to the Sun, exhibit a visible "coma" (or atmosphere) and/or a tail – both primarily from the effects of solar radiation upon the comet's nucleus.

A viable model for the origin of the Solar System must account for its characteristics listed below.

(1) All the planets revolve in the same direction (counterclockwise) around the Sun in elliptical (but near-circular) orbits, and these orbits all lie within a nearly flat disc called the *ecliptic plane*, which is the apparent path that the Sun traces out in the sky. The exception is Mercury, whose orbit is inclined at 7° to the ecliptic plane. The common plane of rotation and the near-circular orbits suggest *in situ* formation of the planets, simultaneously with formation of the Sun, from a disk of material.

(2) All the planets, except Venus and Uranus, rotate on their axis in a counterclockwise direction. Venus rotates slowly to the right and Uranus is tilted on its side with its north pole pointing towards the Sun, possibly due to a catastrophic collision early in the evolution of the Solar System.

(3) More than 99.86% of the mass of the Solar System is concentrated in the Sun at the center of the system, but 98% of its angular momentum resides in the planets at the edges. (Angular momentum is the measure of motion of objects in curved paths, including both rotation and orbital motion.)

(4) There is an orderly change in the composition of the planets with increasing distance from the Sun. The terrestrial planets have high densities (3.9 to 5.5 g cm^{-3}) and no or only a few moons, and are primarily composed of metals and silicate rocks. In contrast, the Jovian planets have lower densities (0.7 to 1.76 g cm^{-3}) and many moons, and are composed of gases – the two largest planets, Jupiter and Saturn, of hydrogen and helium, and the two outermost planets, Uranus and Neptune, largely of ices (such as methane, ammonia, and water vapor). The anomalously high density of Mercury is best explained by the stripping of much of its silicate mantle by collision with a massive planetesimal.

(5) All the components of the Solar System have the same age – about 4.56 Ga based on radiometric measurements on meteorites (Patterson *et al.*, 1956; Allégre *et al.*, 1995).

(6) The planets have a regular spacing – the mean distances of the planets from the Sun are related to a simple mathematical progression of numbers (*Bode's Law*). (This formulation led Bode to predict the existence of another planet between Mars and Jupiter, what we now recognize as the asteroid belt.)

The model that best accounts for these characteristics envisages the creation of the Solar System from a nebula, the Solar Nebula, about 4.56 billion years ago (see section 12.1.6).

12.1.4 Meteorites

A *meteorite* is a rock that was formed elsewhere in the Solar System, was orbiting the Sun or a planet for a long time (a *meteoroid*), was eventually captured by the Earth's gravitational field, and fell to the Earth as a solid object. When a meteoroid passes through the atmosphere, its exterior is heated to incandescence, producing a visible streak of light called a *meteor* or, more commonly a "falling star" or a "shooting star." Most of these objects are very small and burn up in the atmosphere; parts of a few larger ones survive the journey and land on the Earth as meteorites. It is estimated that about 10^6 to 10^7 kg of meteorites, predominantly smaller than 1 mm in size, rain down on the Earth each year; occasionally they have been large enough to produce impact craters such as the Meteor Crater in Arizona. Our database on meteorites is built on the recovered ones, which represent only a small fraction of the population actually received by the Earth.

Most meteorites (~99.8%) are from the asteroids. The catalogued meteorites also include a few martian meteorites (the SNC group, so named for its principal meteorites Shergotty, Nakhla, and Chassigny) and a few lunar meteorites ("lunaites"), which are interpreted to have been ejected from the surface of Mars and the Moon, respectively. Martian meteorites represent the only known samples of another planet available for research. Lunar meteorites are of major scientific importance because most of them probably originated from areas on the far side of the Moon that were not sampled by the Apollo or Luna missions.

The most primitive meteorite specimens are believed to be samples of the most primitive (pre-planetary) material in the Solar Nebula. Some meteorites are so primitive that they contain traces of interstellar dust, which survived thermal processing in the Solar Nebula. Thus, meteorites provide information about the chemical and physical properties at different locations within the Solar Nebular disk, as well as constraints about time scales and physical processes involved in the formation and evolution of objects in the Solar System.

Meteorites show a range of compositions and textures because their parent bodies came into existence in different regions of the Solar Nebula. The most commonly used parameters for classification of meteorites are petrology (texture, mineralogy, and mineral compositions), whole-rock chemical composition, and O-isotopic composition. The abridged classification presented in Table 12.3 is based on petrology. More detailed treatments can be found, for example, in Wasson (1974) and Weisberg *et al*. (2006), and on the Worldwide Web (http://www.meteorite.fr/en/classification).

Of particular interest in the present context are chondrites, which are considered to be samples of pre-planetary material from the Solar Nebula, the volatile-rich carbonaceous chondrites being the most primitive of all meteorites. The parent bodies of chondrites are small to medium sized asteroids that were never part of any celestial body large enough to undergo melting and planetary differentiation. Many of them, however, reached high enough temperatures for thermal metamorphism in their interiors. These metamorphosed chondrites are represented by the so-called *equilibrated chondrites*. The source of the heat most likely was the decay of short-lived radioisotopes, especially ^{26}Al and ^{60}Fe, although some contribution may have come from the heat released during impacts onto the asteroids. The iron meteorites, in contrast, represent the cores of differentiated asteroids, the melting and metal–sulfide–silicate fractionation occurring effectively at the beginning of geologic time (T_0) (Taylor, 1992).

Conspicuous among the constituents present in almost all chondrites are *chondrules*. Carbonaceous chondrites commonly contain ~50% chondrules by volume, whereas ordinary and enstatite chondrites contain up to 80%. Chondrules are spherical bodies ranging in size from ~0.01 to 10 mm across and composed of quenched crystals of ferromagnesian olivine and pyroxene, Fe–Ni metal, troilite (FeS), and glassy or microcrystalline mesostasis (the last-formed interstitial material between the larger mineral grains). The vast majority of chondrules represent molten droplets formed by flash heating of "cool" (< 650 K) nebular dust at peak temperatures of 1770–2120 K (McSween *et al*., 2006) followed by very rapid recondensation, possibly over the span of a few minutes (Hewins, 1997), in the Solar Nebula. Evidence for this conclusion includes relict grains that apparently survived the melting, and the porphyritic texture of most chondrules, which require the presence of residual solid nuclei to facilitate the formation of large crystals. Many chondrules appear to have experienced multiple heating episodes, but most were not completely melted. The coexistence of metallic Fe–Ni with generally Mg-rich olivine and pyroxene in many chondrules reflects a reducing environment during chondrule formation. If the chondrules had been melted in an oxidizing environment, their metallic iron would have been oxidized to FeO, which would have been incorporated by the olivine and pyroxene that crystallized upon cooling. The transient heating episodes were localized because there is no evidence for silicate melting on a nebular scale. However, none of the mechanisms proposed to account for the localized heating – collisional impact, lightning, heating by the Sun, and passage of shock waves – is entirely satisfactory, but thermal processing of particles in nebular shock waves appears to meet most constraints imposed by chondrule properties (Ciesla and Hood, 2002).

Calcium–aluminum-rich inclusions (CAIs) constitute another important, but minor, component of carbonaceous chondrites. These irregularly shaped or round inclusions range in size from microscopic to 5–10 cm. They are enriched, commonly by a factor of 20 or so, in refractory elements such as Ca, Al, Ti, Re, and the noble metals (Ru, Rh, Pd, Ag, Os, Ir, Pt, and Au), and depleted in Fe, Mg, and Si relative to bulk chondrites. The main minerals of CAIs are corundum (Al_2O_3), hibonite ($CaAl_{12}O_{19}$), grossite ($CaAl_4O_7$), perovskite ($CaTiO_3$), spinel ($MgAl_2O_4$), anorthite ($Ca_2Al_2Si_2O_8$), melilite (solid solution of $Ca_2MgSi_2O_7$ and $Ca_2Al_2SiO_7$), and Al–Ti-pyroxene. The origin of CAIs is controversial. Earlier they were thought to be high-temperature equilibrium condensates of the Solar Nebula gas, commonly

Table 12.3 Simplified classification of meteorites (with percentage that falls to the Earth).

Classification	Characteristics
Iron meteorites (5.7%) (Fig. 12.3a, b)	Consist essentially (average 98%) of a Ni–Fe alloy (Ni usually between 4 and 20%, rarely greater), most with a characteristic structure known as Widmanstätten pattern, which consists of lamellae of kamacite (a Ni–Fe alloy containing about 6% Ni) bordered by taenite (another Ni–Fe alloy containing about 30% Ni); this pattern is typical of exsolution from a high-temperature alloy by very slow cooling. Accessory minerals include troilite (FeS), schreibersite $(Fe,Ni,Co)_3P$, graphite (C), daubreelite ($FeCr_2S_4$), cohenite (Fe_3C), and lawrencite ($FeCl_2$).
Stony–iron meteorites (1.5%)	Composed of Ni-Fe alloys and silicate minerals in approximately equal amounts.
Pallasites (Fig. 12.3c)	Consists of abundant olivine crystals (often of gem quality) in a continuous base of Ni–Fe alloy, rendering the meteorite a distinctive texture. Regarded as samples of core–mantle boundary material from differentiated asteroids.
Mesodiorites	The base of Ni–Fe alloy is discontinuous and olivine, if present, is an accessory phase. The silicate portion is heavily brecciated and consists mostly of pyroxene and plagioclase. Have a complex formation history.
Stony meteorites	Composed predominantly of silicate minerals (olivine and pyroxene). Other constituents include variable amounts of refractory inclusions, particles rich in Fe–Ni and sulfides, and interstellar dust.
Chondrites (85.7%)	Stony meteorites that have not been modified due to melting or differentiation of the parent body. Some were thermally metamorphosed (recrystalized without melting) in the Solar Nebula; these are referred to as equilibrated chondrites. Most chondrites contain chondrules. Other constituents of chondrites are Fe–Ni metal and sulfide grains, ameboid olivine aggregates (AOAs), isolated grains of silicate minerals, and very fine-grained dust with embedded presolar grains that originated elsewhere in the galaxy. The various classes of chondrites differ in their proportions of chondrules, calcium–aluminum inclusions (CAIs), and metal.
Carbonaceous chondrite (Fig. 12.3d)	Consists largely of hydrated ferromagnesian silicates (serpentine or chlorite); up to 10% of complex organic compounds, which are not of biologic origin but may represent precursors of biologic organisms; and CAIs, which are among he first solids condensed from the cooling protoplanetary disk. Some contain veins of carbonates and sulfates. The most volatile rich among meteorites. Chemistry matches that of the Sun more closely than any other class of chondrites. Parent bodies represent some of the most primitive matter that formed in oxygen-rich regions of early Solar System.
Ordinary chondrites (Fig. 12.3e)	Most common class of stony meteorites. Composed mostly of olivine and pyroxene. Contain both volatile and oxidized elements, and are believed to have formed in the inner asteroid belt.
Other chondrites	Less common chondrites of variable petrology and chemical composition. At one end of the spectrum are the highly reduced enstatite or E chondrites, containing enstatite ($MgSiO_3$) and almost all of their iron in the metallic form; these must have formed in the inner solar system. At the other end are the highly oxidized rumurutiite or R chondrites, containing large amounts of Fe-rich olivine and oxidized iron, suggesting formation farther from the Sun
Achondrites (7.1%) (Fig. 12.3f)	Do not contain chondrules, have lower abundances of volatile and moderately volatile (e.g., the alkalis) elements, and are usually much more coarsely crystalline than chondrites. Many resemble terrestrial basaltic rocks in composition and texture. They crystallized from silicate melts or are residues of partial melting, and represent pieces of differentiated asteroids that have fragmented due to collision.
	Subclasses include: primitive achondrites (residues from partial melting that took place on small parent bodies having chondritic bulk compositions); meteorites from the asteroid Vesta (HED Group); other evolved achondrites; lunar meteorites (LUN Group); and martian meteorites (SNC Group).

modified by melting, recrystallization, and alteration; they are now generally interpreted to be mixtures of condensate materials and refractory residues of materials vaporized by transitory and local heating events, although some CAIs are probably condensates.

The U–Pb absolute age of CAIs in the Allende chondrite has been determined to be 4.566 ± 0.002 Ga (Allègre *et al.*, 1995), almost identical to the age, 4.5672 ± 0.0006 Ga, obtained for CAIs in the Efremovka chondrite (Amelin *et al.*, 2002), which make them the oldest material in the Solar System sampled and dated so far. Using ^{26}Al–^{26}Mg isotope systematics, it has been shown that many chondrules formed within 1 to 2 Myr of CAIs, and that high-temperature nebular processes, such as CAI and chondrule formation, lasted for about 3–5 Myr (Russell *et al.*, 2006). The Earth and the Moon formed about 50 to 100 Myr later. Carbonaceous chondrites are also notable for their "primitive" chemical composition, "primitive" in the sense that abundances of most chemical elements do not differ by more than a factor of two from those in the Sun's *photosphere* (the region of a star's surface, composed largely of neutral gas

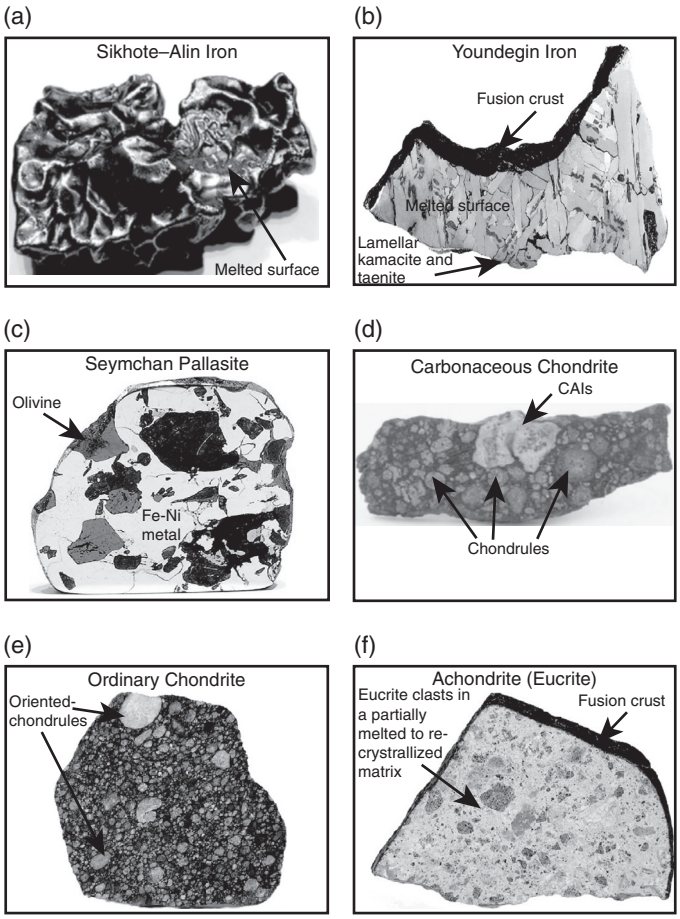

Fig. 12.3 Fragments of selected meteorites (Meteorites Australia Collection). (a) Iron meteorite (Sikhote-Alin; 83 g) with a melted surface. (b) Iron meteorite (Youndegin; 76.1 g complete slice) composed almost entirely of lamellar Fe–Ni alloys kamacite and taenite. (c) Stony iron meteorite (Seymchan pallasite; 15.5 g complete slice) showing olivine crystals in a Fe–Ni metal matrix. (d) Carbonaceous chondrite (NWA 2140; 1.31 g slice) with irregular shaped, light colored Ca–Al-rich inclusions (CAIs) and well preserved chondrules. (e) Ordinary chondrite (NWA 5507; 5.99 g complete slice) containing an abundance of chondrules, some of which show a preferred orientation. (f) Achondrite (NWA 1836 /Eucrite; 7.1 g crusted slice), a melted cumulate rock. (Source: http://www.meteorites.com.au/collection) (Copyright © 2002–2011, Meteorites Australia. Reproduced with permission of Jeff Kuyken, Meteorites Australia.)

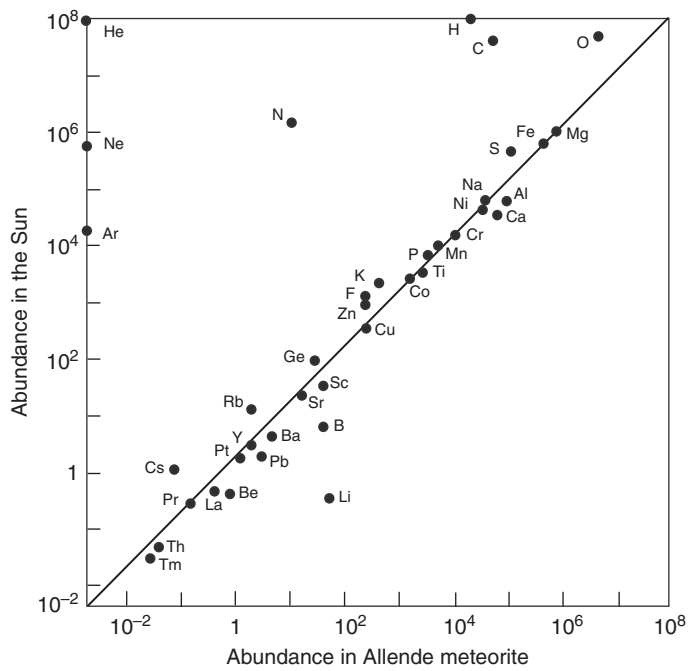

Fig. 12.4 Comparison of element abundances in the Allende meteorite, a carbonaceous chondrite, with those in the solar photosphere. Both axes are normalized to 10^6 silicon atoms. The diagonal line represents perfect correspondence. The scale is logarithmic, but the abundances are within a factor of two of each other, except for the highly volatile elements (H, C, N, O, and inert gases). (From *Geochemistry: Pathways and Processes* by H.Y. McSween, S.M. Richardson, and M.E. Uhle, Figure 15.5, p. 320; Copyright © 2003; Columbia University Press, New York. Used with permission of the publisher.)

atoms at a temperature of ~5700 K, from which radiation escapes), which in turn is believed to define the composition of our Solar System. This is the reason why chondrite compositions are often used as a standard for assessing the degree of chemical fractionation experienced by materials formed throughout the Solar System, including terrestrial rocks (see section 12.2.5). A comparison of the element abundances (normalized to 10^6 Si atoms) in the extensively studied Allende meteorite, a relatively primitive carbonaceous chondrite, with those in the Sun's photosphere (derived from spectral lines of the light emitted from the photosphere) illustrates the close match between them (Fig. 12.4), except for depletion of extremely volatile elements (H, He, C, N, O, and noble gases) and enrichment of a few very light elements (Li, Be, and B). It is assumed that the element abundances in the Sun's photosphere are representative of the Solar Nebula. This is a reasonable assumption because nuclear synthesis during the Sun's evolution should have affected only the composition of the deep interior (with the exception of Li, Be, and B, which are destroyed during hydrogen burning and so have been depleted near the Sun's surface).

12.1.5 Solar System abundances of the elements

The Solar System abundances of the elements, as compiled by Anders and Grevesse (1989), are listed in Appendix 9 and graphically represented in Fig. 12.5. The abundances are based mainly on the analyses of CI chondrites (a group of carbonaceous chondrites that lack chondrules and CAIs, but represent samples of the most undifferentiated Solar System matter available to us), except for the incompletely condensed elements (H, C, N, and O) and noble gases, for which solar photosphere and other astronomical data were used. The values are in terms of

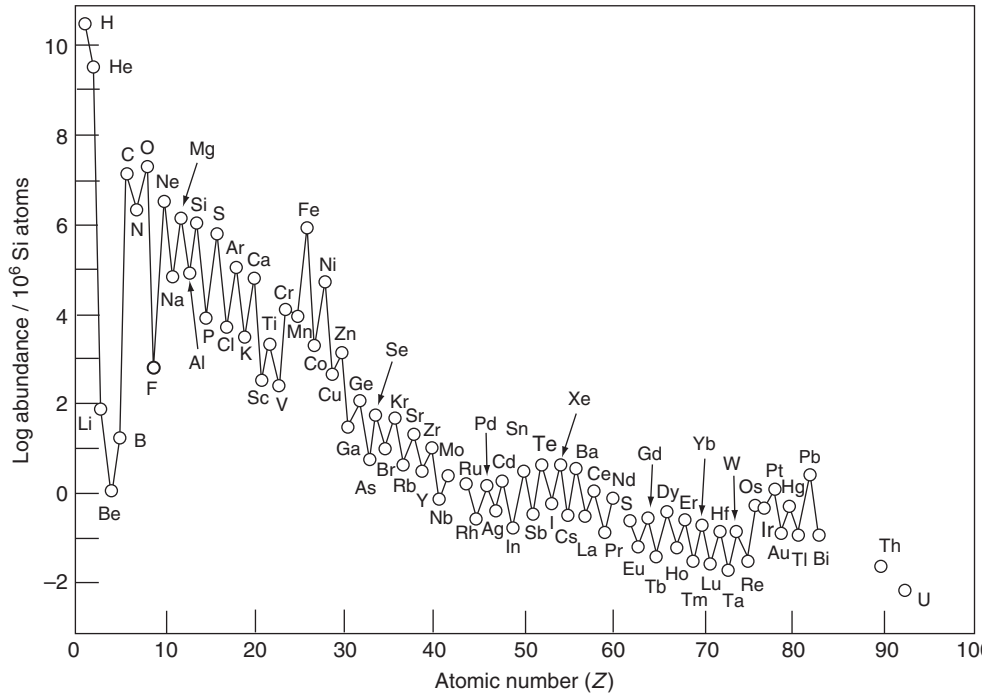

Fig. 12.5 Solar System abundances of the elements normalized to 10^6 silicon atoms. (Source of data: Anders and Grevesse (1989).)

number of atoms, normalized to 10^6 silicon atoms to keep these numbers from being very large. This abundance pattern is often referred to as the *cosmic abundance* of the elements, although it does not necessarily represent the composition of the universe because of variations in the compositions of the stars.

Noteworthy features of the abundance pattern revealed in Fig. 12.5 are as follows.

(1) Hydrogen and helium are, by far, the most abundant elements in the Solar System because these were the primary constituents of the primitive universe; the atomic H : He ratio is about 10.25: 1.
(2) The overall pattern is one of rapidly decreasing abundance with increasing atomic number (although the trend flattens for elements with $Z > 50$), reflecting decreasing nucleosynthesis in the more advanced burning cycles.
(3) Exceptions to the above trend are the abnormally low abundances of Li, Be, and B, which are depleted due to subsequent nuclear burning, and the higher abundance of the iron group relative to its neighbors (for reasons mentioned earlier). The high abundance of Fe makes it an inescapable candidate for being a major constituent of planetary cores.
(4) Elements having even atomic numbers (such as $^{12}_{6}$C) carbon are more abundant than their immediate neighbors having odd atomic numbers (such as $^{14}_{7}$C), which is known as the *Oddo–Harkins* rule. This is because elements with odd atomic numbers have one unpaired proton and are more likely to capture another, thus increasing their atomic number. In elements with even atomic numbers, protons are paired, with each member of the pair offsetting the spin of the other, thus enhancing the stability of the atom. A notable exception to this postulate is $^{1}_{1}$H, the most abundant element in the universe.

12.1.6 *Origin of the Solar System: the planetesimal model*

The most widely accepted model for the origin of the Solar System is that it started about 5 Ga with the formation of a nebula (an interstellar, rotating molecular cloud) from a larger molecular gas cloud some 30 to 40 light years across and 2 to 10 times the mass of the present Solar System. About 10,000 years after the Big Bang, the temperature had fallen to such an extent that the energy density of the universe began to be dominated by massive particles, rather than the light and other radiation that had predominated earlier. Thus, besides the hydrogen and helium gas and plasma generated during the Big Bang, the Solar Nebula consisted of microscopic dust (solid particles) and the ejected matter of long-dead stars. The occurrence of excess amounts of the isotope $^{24}_{12}$Mg in CAIs of chondrites, attributed to the radioactive decay of the short-lived, now-extinct radionuclide $^{26}_{13}$Al (half-life = 0.73×10^6 yr), suggests that the Solar Nebula formed very soon after nucleosynthesis. The neutron-rich, short-lived isotope $^{60}_{26}$Fe (which decays to $^{60}_{28}$Ni with a half-life of 1.5×10^6 yr only) is not formed in abundance by spallation reactions, but is formed in core collapse supernovae. The confirmation of live $^{60}_{26}$Fe isotopes

in the early Solar System is compelling evidence that the Solar System formed near a massive star that eventually went supernova, injecting elements already synthesized within the massive star into the Solar Nebula (Hester and Desch, 2005).

The Solar Nebula, estimated to have been composed essentially of H_2 and He (99.98%) with a $H_2O:H_2$ ratio of 5.4×10^{-4} (Lodders, 2003), collapsed under gravitational attraction, probably triggered by shock waves from the nearby supernova explosion. The collapsed material began a counterclockwise rotation, much of it gravitating to the center of rotation, and conservation of angular momentum caused the nebula to spin faster and faster. The balance between gravity and rotation led to a flattened disk (often referred to as the *proto-planetary disk*) with about 90% of the material concentrated in the central region, forming the proto-Sun that eventually developed into the present Sun. The planets formed as a byproduct of the evolution of the Solar Nebula, constrained by conservation of angular momentum contained in the system. That is why the planets revolve and rotate in counterclockwise direction, and their solar orbits lie nearly on the ecliptic plane. According to the law of conservation of angular momentum, the Sun should be rotating faster than it actually does (25 days per a 360° rotation); the relatively slow rotation is attributed to magnetic flow lines of the Sun interacting with ionized gases in the Solar Nebula.

The formation of the planets involved two important processes: *condensation* of the hot nebular gases into solid grains (dust); and *accretion* of the dust grains into progressively larger solid bodies, which acquired most of their materials locally. The temperature of the proto-planetary disk varied from ~2000 K at the center to ~40 K at approximately 50 AU ($=7.5 \times 10^9$ km) from the proto-Sun. The pressure ranged from less than 0.1 atm at the center to about 10^{-7} atm near the edge of the disk (Cameron and Pine, 1973). According to most astrophysical models, the bulk of the pre-solar solid matter in the interior of the disk vaporized and then condensed as the nebula cooled after the formation of the proto-Sun. The condensation sequence was controlled by *P–T* conditions in various parts of the disk (see, e.g., Grossman and Larimer, 1974). No liquids were produced during condensation because the pressure in the Solar Nebula was too low. Refractory constituents of low volatility such as compounds of magnesium, calcium, iron, and silicon, and Fe–Ni metal, were largely left in planetary masses close to the Sun, where the terrestrial planets formed subsequently by accretion. Not much gas could accumulate in the inner Solar System because of the high temperature. Violent solar flares and solar wind, known as T-Tauri wind, carried hydrogen, helium, the noble gases, and many of the volatile elements outward, beyond 4 to 5 AU, where they accreted to the giant gassy planets, but with rocky, metallic cores. The predominantly gaseous composition of the outer planets is because of the much greater abundance of gases (mainly hydrogen and helium) in the original interstellar material. Water was able to condense as ice in the nebula at a temperature of ~160 K at 4–5 AU and be retained in the distant planets and the satellites of the giant planets. This scenario explains the depletion of the terrestrial planets and meteorites in inert gases and volatile elements (such as K, Pb, and Rb). Cameron (1995) provides a detailed discussion of the nebula stage of the Solar System, which lasted about 1 Myr or less.

In the accretional stage of the planets, solid particles in the rotating proto-planetary disk began to coalesce together, possibly in regions of localized higher gravity such as the mid-plane of the accretion disk, to form a hierarchy of solid bodies of progressively larger sizes, starting with small grains and reaching dimensions of the order of 1 km. The kilometer-sized solid bodies are called *planetesimals*. Experiments have shown that irregular dust grains can stick together if they collide at speeds up to a few tens of meters per second. It is estimated by computer simulation that planetesimals with diameters of 5 km are achievable after a few thousand years. Once accretion produced kilometer-sized bodies, they were no longer controlled by nebular gas drag, and the planetesimals grew rapidly into *planetary embryos* of the order of 1000 km in diameter in roughly 10^5–10^6 yr by swallowing smaller objects available in their respective "feeding zone" (a roughly annular region of the order of 0.01 AU in width), a process referred to as "runaway growth" (Chambers, 2004). The ultimate size of a planet depended upon the amount of material available in its feeding zone.

The final stage of planetary accretion occurred over a timeframe of 10^7 years, and involved the collision of a few dozen planetary embryos comparable in size to the Moon or Mars (0.01–0.1 Earth masses). Numerical simulations suggest that the accretion of the Earth may have occurred in as little as ~5 Myr in the presence of a significant amount of nebular gas or in as long as ~100 Myr without the gas, although most of the planetary mass would probably be accreted within the first 10 Myr (Wetherill, 1986). It is not clear how much nebular gas was present during these early growth stages, but the near-circular orbits of the planets can be explained by the dampening of eccentricities due to the presence of even a small amount of nebular gas (Halliday, 2006). A small amount of dust and gases that never accreted into larger bodies still remain in interplanetary space. Smaller bodies not accreted into planets, except those retained in the asteroid belt, were lost from the Solar System.

The final planets were a mixture of material from a broad region of the inner Solar System, but most of it for any planet came from its own locale, the variations in the composition of the planets arising from the difference in the suites of planetesimals they acquired. The formation of the planets, including the Earth, was complete by 4.56 Ga, which is considered the beginning of geologic time (T_0).

12.2 Evolution of the Earth

12.2.1 The internal structure of the Earth

The present-day internal structure of the Earth is a composite of its original accretionary growth and subsequent modifications by physical and chemical processes such as heating,

convective circulation, geochemical differentiation, etc. In essence, the Earth's interior consists of three concentric shells of markedly different composition and density (Fig. 12.6a): the *core*, the *mantle*, and the *crust*. This interpretation is based on multiple lines of evidence (Fig. 12.6b): (i) sharp breaks in density, which generally increases with depth; (ii) sharp breaks in the velocities of P and S seismic waves, which depend on the density and elastic constants of the medium; (iii) differentiation of the parent bodies of meteorites, as reflected in the spectrum of meteorite compositions; and (iv) mineralogy and estimated *P–T* conditions of equilibration of rock samples from the Earth's interior brought up through magmatism.

The crust

The volumetrically insignificant crust (only 0.7% of the Earth's mass) is composed almost entirely of silicate minerals, only eight elements – O, Si, Al, Fe, Ca, Mg, Na, K – making up about 99% of the total. The crust is of two distinct types: *oceanic crust* and *continental crust*. The low-lying oceanic crust, which covers approximately 70% of the Earth's surface area, is relatively thin (from ~4 km at some mid-ocean ridges to more than 10 km in some oceanic volcanic plateaus produced from profuse outpourings of basaltic lava; average thickness ~7 km), young (≤ 200 Ma), fairly homogeneous on a large scale, and composed of relatively dense rock types such as basalt (enriched in Ca, Mg, and Fe; Table 12.4). The continental crust, on the other hand, is topographically higher, thicker (from 20 to 80 km, average thickness ~40 km), much older (> 3.8 Ga at places), and composed of diverse lithologies that yield an average intermediate igneous rock or "andesitic" bulk composition (enriched in Si, Na, K, volatiles, and radioactive elements). The continental crust is significantly enriched incompatible elements (with about 1% of the mass of the primitive mantle, it contains up to 50% of the primitive mantle's budget for these elements); it has a high La/Nb ratio, a low Ce/Pb ratio, and a subchondritic Nb/Ta ratio (Rudnick and Gao, 2004). The presence of a chemically evolved continental crust is one of the Earth's unique features compared to other rocky planets in our Solar System.

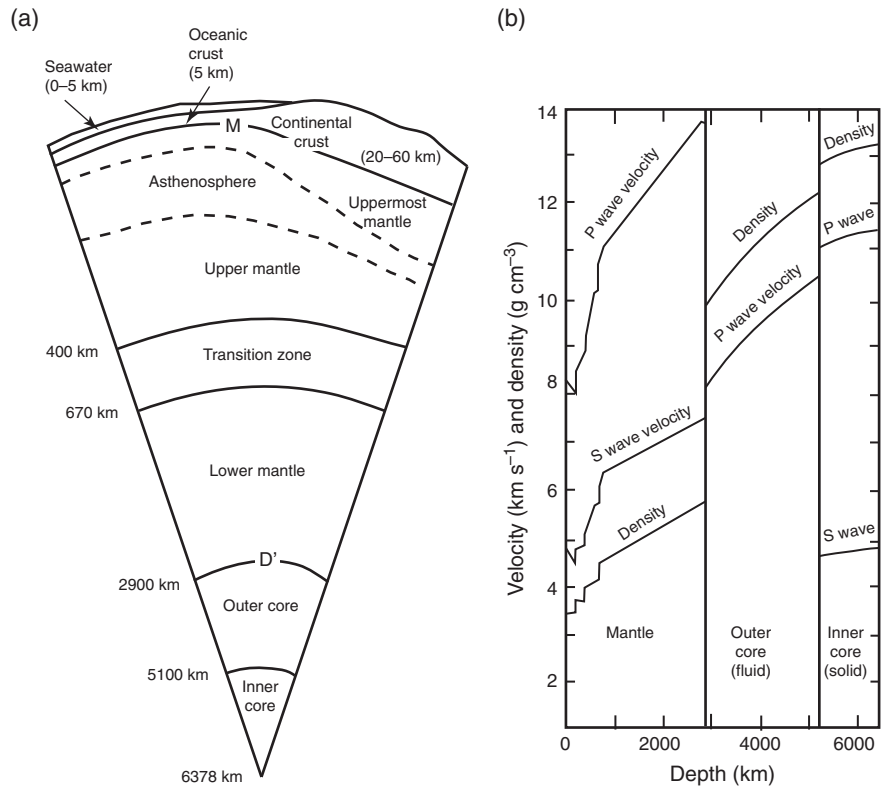

Fig. 12.6 (a) Schematic section of the Earth. Details of the crust and mantle are not to scale. M = Mohorovicic Discontinuity (commonly referred to as "Moho"); D" = the core–mantle boundary (CMB) (Wiechert–Gutenberg discontinuity?). The average densities of the various units are as follows: continental crust – 2.7 to 3.0; oceanic crust – 3.0 to 3.3; mantle – 3.3 to 5.7; outer core (liquid) – 9.9 to 12.2; inner core (solid) – 12.6 to 13.0. (b) Variation of density and velocities of seismic body waves (P- and S-waves) as a function of depth. Note that S-waves do not pass through the liquid outer core. (Sources of data: Wilson (1989); Ernst (2000).)

The mantle

Compared to the crust, the mantle, which represents about 83% of the volume and 68.3% of the mass of the Earth, is enriched in Mg, contains less Fe and much less Si, and is depleted in volatile and radioactive elements. The mantle is divided into three regions on the basis of major discontinuities in seismic velocities (Fig. 12.6a). The *upper mantle* extends from the *Mohorovicic Discontinuity* (or *Moho*), which marks a jump in compressional seismic wave (P-wave) velocity from ~7 km s^{-1} to ~8 km s^{-1} and is interpreted to mark the crust–mantle boundary, to a major seismic discontinuity occurring near a depth of 400 km. In some regions the Moho is transitional rather than a sharp discontinuity, and the exact location of the crust–mantle boundary is debatable. The upper mantle includes the lower part of the *lithosphere*, the strong outer layer of the Earth, including the crust, which reacts to stresses as a brittle solid, and the underlying weaker *asthenosphere* that readily deforms by creep. The asthenosphere is a low-velocity zone in which seismic waves are attenuated strongly, indicating the possible presence of a partial melt phase. This is also the zone in the upper mantle in which convective motions are most likely to occur.

A second major seismic discontinuity occurs near a depth of 650–670 km, and the region between the two seismic discontinuities is referred to as the *transition zone*. The *lower mantle* comprises the large region between the "650 km discontinuity" and the core, the outer limit of which is encountered at a depth of 2900 km. Constrained by the observed P-wave velocities, the compositions of ophiolite complexes and xenoliths recovered from alkali basalts and kimberlites, and the requirement that the mantle material must be capable of producing the large volumes of terrestrial basaltic magmas by partial melting, the upper mantle is inferred to be composed of ultramafic rocks such as peridotite (olivine + pyroxene) and eclogite (garnet + pyroxene). The composition of the upper mantle under oceanic crust is thought to be somewhat different from that under the continental crust. In both cases, however, the peridotite immediately below the Moho has been depleted in incompatible elements because of the extraction of copious volumes of basaltic magmas throughout geologic time, and the depleted peridotite is underlain by primitive, undepleted peridotite (Fig. 12.7). Clark and Ringwood (1964) proposed that the overall composition of this primitive source rock, which is capable of yielding basaltic magma on partial melting, corresponds to a hypothetical mixture of one part basalt to three parts dunite, and called it "pyrolite" (pyroxene–olivine rock) (Table 12.4). The depleted peridotite under the continental crust is thought to contain pockets of eclogite segregations; that beneath the oceanic crust is believed to be composed of an upper layer of strongly depleted harzburgite (olivine + orthopyroxene) due to extraction of mid-oceanic ridge basalts, and a lower layer of less depleted lherzolite (olivine + orthopyroxene + clinopyroxene) (Ringwood, 1991).

Most geophysical measurements are at least consistent with the upper and lower mantle, as well as the transition zone, having broadly the same bulk chemical composition. The mineralogy of the mantle, however, varies as a function of depth (Fig. 12.8) because of progressive increase in load pressure. High-

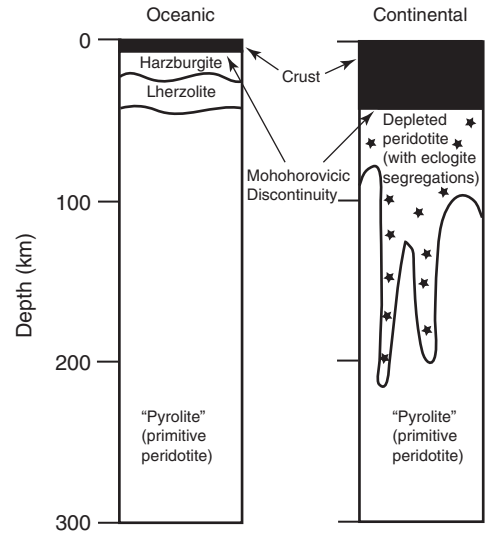

Fig. 12.7 Composition of the upper mantle according to the pyrolite model. (After Ringwood, 1991, Figure 1, p. 2326.)

pressure experimental data indicate that the transition zone is characterized by denser polymorphs of olivine: β-olivine, which has a distorted spinel structure (compared to orthorhombic α-olivine, whose structure consists of independent SiO_4 tetrahedra linked by divalent aoms in sixfold coordination); and, at still higher pressures, γ-olivine, which has a spinel structure. At a depth of about 300 km, the pyroxene components begin to form a solid solution with the garnet, and at about 450 km depth, the Si-rich garnet solid solution [termed *majorite*, empirical formula $Mg_3Fe_{1.2}^{3+}Al_{0.6}Si_{0.2}(SiO_4)_3$] becomes the only stable aluminous phase. The mineral assemblage adopted by pyrolite in the lower mantle is believed to comprise three dense phases – Mg-perovskite ($MgSiO_3$ with perovskite structure), Ca-perovskite ($CaSiO_3$ with perovskite structure), and magnesiowüstite ((Mg, Fe)O).

The core

The Earth's core comprises about 16% of the Earth's volume and 31% of the Earth's mass. The average density of the Earth is 5.515 g cm^{-3}, making it the most dense planet in the Solar System. Since the average density of the crust is only 2.7 to 3.3 g cm^{-3} and that of the mantle is 3.3 to 5.7 g cm^{-3}, the Earth's core must be made of high-density elements, an inference supported by seismic data. If we assume chondritic meteorites to be the building blocks of terrestrial planets, the much less concentrations of siderophile elements in the Earth's upper mantle implies that these elements reside mainly in the core. The Earth's core is believed to be composed of Fe–Ni alloy (primarily Fe, with about 4–5% Ni and 0.2% Co), probably with small amounts of lighter elements such as S, C, O, and Si (Stevenson, 1981; Poirier, 1994; Kargel and Lewis, 1993; Allègre *et al.*, 1995). Model calculations by Kargel and Lewis (1993) yielded

Table 12.4 Estimated model compositions (major elements).

Oxide (wt%)	Primitive mantle† (1)	Primitive mantle (2)	Pyrolite (3)	Continental crust (4)	Oceanic crust (5)	"Normal" MORB (6)
SiO_2	45.0	49.9	45.16	59.7	49.4	50.45
TiO_2	0.20	0.16	0.71	0.68	1.4	1.61
Al_2O_3	4.45	3.65	3.54	15.7	15.4	15.25
Cr_2O_3	0.384	0.44	0.43			
MgO	37.8	35.15	37.47	4.3	7.6	7.58
FeO	8.05*	8.0*	8.04	6.5*	7.6	10.43*
Fe_2O_3			0.46		2.7	
CaO	3.55	2.90	3.08	6.0	12.5	11.30
MnO	0.135	0.13	0.14	0.09	0.3	
NiO	0.25	0.25	0.20			
CoO	0.013		0.01			
Na_2O	0.36	0.34	0.57	3.1	2.6	2.68
K_2O	0.029	0.022	0.13	1.8	0.3	0.09
P_2O_5	0.021	0.06	0.06	0.11	0.2	

(1) McDonough and Sun (1995), based on compositions of peridotite, komatiites, and basalts; (2) Taylor and McLennan (1985), based on CI carbonaceous chondrites; (3) Ringwood (1966); (4) Condie (1997); (5) Ronov and Yaroshevsky (1976); (6) Hofmann (1988).
*Total Fe as FeO.
†Primitive mantle (or bulk silicate Earth) = Earth's mantle immediately after the core formation (i.e., the present mantle plus crust).

the following composition for the core (in wt%): Fe – 85.55, O – 5.18, Ni – 4.88, S – 2.69, Cr – 0.45, Mn – 0.41, P – 0.35, Co – 0.22, Cl – 0.07, and possibly K – 0.02; modeling by Allègre *et al.* (1995) produced similar numbers for O (4 wt%) and S (2.3 wt%), but also 7.3 wt% Si. The outer core is interpreted to be molten (at a temperature of ~5000°C) because of its low viscosity and inability to transmit S-waves, whereas the inner core is solid, with the crystals probably exhibiting a large degree of common orientation. The liquid state of the outer core can be rationalized by the disposition of the melting curve for metallic iron (and minor nickel) relative to the Earth's present geothermal gradient (Fig. 12.9). The Earth's magnetic field owes its origin to fluid flow within the outer core, and the differential motion between the outer liquid, metallic core and the base of the solid, silicate mantle. One effect of this magnetic field is that it deflects the solar wind from the Earth, and therefore prevents certain molecules (e.g., water vapor) in the atmosphere from being swept away into space.

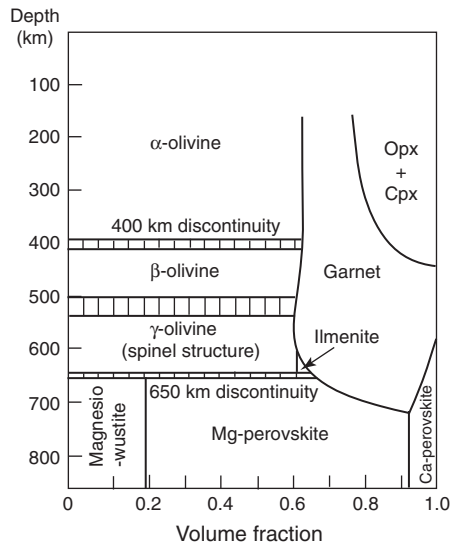

Fig. 12.8 Distribution of mineral assemblages in the upper mantle, assuming a pyrolite compositional model (after Ringwood, 1991). It is assumed that the temperature at 400 km depth is near 1400°C and at 650 km depth is near 1600°C. Opx = orthopyroxene; Cpx = clinopyroxene. (After Ringwood, 1991, Figure 4, p. 2090.)

12.2.2 Bulk Earth composition

The ratios of various elements and isotopes in the Earth roughly match those of undifferentiated chondrites. It appears reasonable, therefore, to infer that the bulk composition of the Earth itself must be close to the average composition of chondritic meteorites, the presumed building blocks of the Earth. The Earth's bulk composition can then be computed by distributing the metal and silicates of meteorites so as to satisfy the requirements of density and elastic properties deduced from the behavior of seismic waves. Mason (1966), for example, calculated the bulk composition of the Earth assuming that (i) the core has the composition of the average for iron–nickel in chondrites, and includes the average amount (5.3%) FeS in these meteorites; and (ii) the composition of the *bulk silicate Earth* (BSE), the residual silicate portion of the Earth after core formation, now represented by modern mantle plus crust, is the same as the silicates (plus small amounts of phosphates and oxides) of the "average" chondrite. The problem is that there is no consensus as to what kind of meteorite should be chosen as

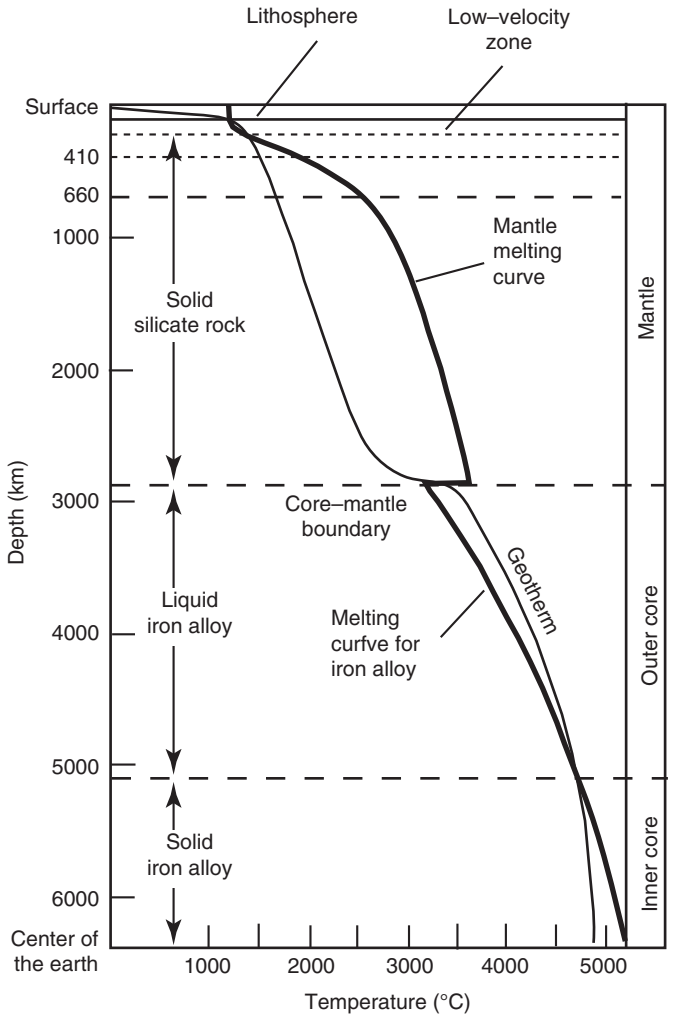

Fig. 12.9 Explanation for the liquid state of the outer core based on the estimated relative positions of the geotherm (which describes the increase in temperature with depth) and the melting curve for iron alloy. The geotherm lies below the mantle melting curve throughout most of the mantle (solid) and below the melting curve for iron alloy in the inner core (solid), but it lies above the iron melting curve in the outer core (liquid). The intersection of the geotherm with the mantle melting curve at the base of the lithosphere is consistent with the partially molten low-velocity zone. (After Grotzinger and Jordan, 2010 , Figure 14.10,p. 379.)

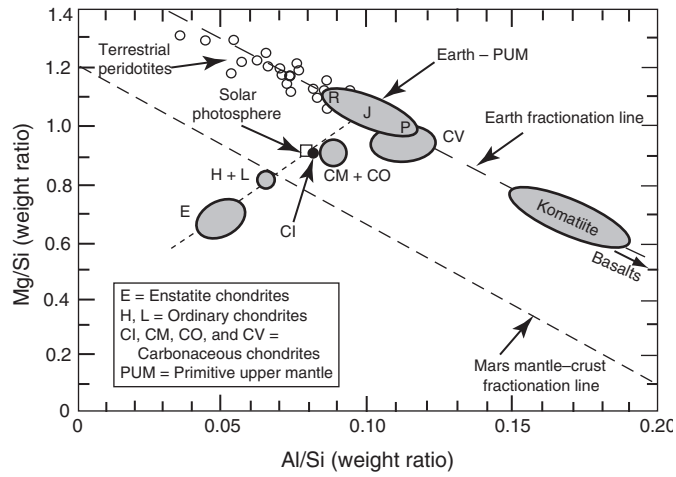

Fig. 12.10 Al/Si versus Mg/Si ratios of primitive material in the inner Solar System define an unexplained trend that is very different from the Earth's fractionation line defined by peridotites, komatiites, and basalts. The intersection of the two trends gives Si/Al ~0.11 and Mg/Si ~1, which are considered as the most plausible values for the bulk silicate Earth (BSE; Drake and Righter, 2002). The letters R, J, and P refer to estimates of the BSE composition by Ringwood (1979), Jagoutz et al.(1979), and Palme and Nickel (1986), respectively. Martian fractionation line is defined by Chassigny, shergottites, and martian soils and rocks from the Viking and Pathfinder mission (Dreibus et al.,1998). (Modified from *Meteorites and the Early Solar System, II,* edited by D. Lauretta, and H.Y. McSween, Jr. © 2006 The Arizona Board of Regents. Reprinted by permission of the University of Arizona Press.)

the best representative of an average composition or how meteorite compositions should be weighted to get an average composition.

There is even a more fundamental argument against the above approach. Drake and Righter (2002) compared Mg/Si and Al/Si ratios (Fig. 12.10), oxygen-isotope ratios, osmium-isotope ratios, and D/H, Ar/H_2O and Kr/Xe ratios of material from the Earth, Mars, comets, and various meteorites, and concluded that no primitive material similar to the Earth's mantle is currently represented in our meteorite collections. It appears that the "building blocks" of the Earth, at least in part, were composed of chondrites or achondrites yet to be sampled. Zolensky *et al.* (2006) have shown that the flux of material to the Earth's surface changes over time such that material accreting to the Earth today may not be entirely representative of that available in the early Solar System. The estimation of the Earth's bulk composition is a difficult task in the absence of known chondrites that could be considered representative of the undifferentiated primitive Earth.

An alternative approach would be to combine the average compositions of the Earth's various units formed by differentiation according to their relative proportions. The problem is that whereas the compositions of the atmosphere, hydrosphere, and crust can be determined by direct measurements, the compositions of the mantle and core are model dependent. There is no way to calculate the core composition directly from seismic data, which merely constrain the density and physical state, and the composition of the mantle is dependent on the model adopted for the composition of the "primitive mantle" (the *bulk silicate Earth*, BSE).

Element abundances for the whole Earth presented in Table 12.5 were estimated by Kargel and Lewis (1993) following a different approach. First, they established a "best" estimate of the BSE. This estimate was based on analyses of oceanic basalts, continental flood basalts, oceanic and continental alkali basalts, ultramafic components of ophiolites, Archean komatiites, and spinel- and

Table 12.5 Estimated bulk Earth element abundances (in ppm).

Z	Element	Abundance	Z	Element	Abundance	Z	Element	Abundance
1	H	36.9?	32	Ge	10.2	63	Eu	0.1035
2	He		33	As	1.73	64	Gd	0.363
3	Li	1.69	34	Se	3.16	65	Tb	0.0671
4	Be	0.052	35	Br	0.13	66	Dy	0.448
5	B	0.292	36	Kr	?	67	Ho	0.1027
6	C	44?	37	Rb	0.76	68	Er	0.294
7	N	0.59	38	Sr	14.4	69	Tm	0.0447
8	O	316700	39	Y	2.88	70	Yb	0.300
9	F	15.8	40	Zr	7.74	71	Lu	0.0449
10	Ne	?	41	Nb	0.517	72	Hf	0.203
11	Na	2450	42	Mo	1.71	73	Ta	0.0281
12	Mg	148600	43	Tc		74	W	0.171
13	Al	14330	44	Ru	1.71	75	Re	0.0674
14	Si	145900	45	Rh	0.227	76	Os	0.898
15	P	1180	46	Pd	0.831	77	Ir	0.889
16	S	8930	47	Ag	0.099	78	Pt	1.77
17	Cl	264	48	Cd	0.068	79	Au	0.157
18	Ar	?	49	In	0.0049	80	Hg	0.0065
19	K	225	50	Sn	0.34	81	Tl	0.0073
20	Ca	16570	51	Sb	0.061	82	Pb#	0.172
21	Sc	11.1	52	Te	0.39	83	Bi	0.0057
22	Ti	797	53	I	0.036	84	Po	
23	V	104	54	Xe	?	85	At	
24	Cr	3423	55	Cs	0.055	86	Rn	
25	Mn	2046	56	Ba	4.33	87	Fr	
26	Fe	320400	57	La	0.434	88	Ra	
27	Co	779	58	Ce	1.114	89	Ac	
28	Ni	17200	59	Pr	0.165	90	Th	0.0543
29	Cu	82.7	60	Nd	0.836	91	Pa	
30	Zn	47.3	61	Pm		92	U	0.0152
31	Ga	4.42	62	Sm	0.272		Sum	100.02

Nonradiogenic Pb only.
Source of data: Kargel and Lewis (1993).

garnet-bearing xenoliths recovered from basalts and kimberlites (see section 12. 3.1). The BSE incorporates the combined effects of core formation and volatility, presumably including condensation and sublimation in the solar nebula and volatile loss during the accretion and early evolution of the Earth. So, next, they established the Earth's *volatility trend*, which was based on a plot of chondrite-normalized abundances of lithophile elements versus calculated nebular condensation temperatures. Element abundances for the core and the bulk Earth were inferred from BSE abundances and the volatility trend.

Examination of Table 12.5 shows that (i) about 90% of the Earth is made up of only four elements: Fe, O, Si, and Mg; (ii) the abundance of only three other elements – Ni, Ca, and Al – exceed 1%; and (iii) ten elements – Na, P, S, Cl, K, Ti, V, Cr, Mn, and Co – occur in amounts ranging from 0.01 to 1%. Thus 17 elements account for about 99.9% of the bulk Earth chemical composition, the rest of the elements comprising 0.1% or less of the bulk.

12.2.3 The primary geochemical differentiation of the proto-Earth: formation of the Earth's core and mantle

Timing of core formation

Short-lived radioactive isotopes, such as ^{26}Al ($^{26}Al \Rightarrow {}^{26}Mg$; $t_{1/2} = 0.73$ Myr), ^{60}Fe ($^{60}Fe \Rightarrow {}^{60}Ni$; $t_{1/2} = 1.5$ Myr), and ^{182}Hf ($^{182}Hf \Rightarrow {}^{182}W$; $t_{1/2} = 8.9$ Myr), can be used to constrain the timimg of differentiation events that occurred within their lifetimes. The decay of the extinct radionuclide ^{182}Hf to ^{182}W is an ideal isotopic system for tracing the rates of accretion and core formation of the Earth and other inner Solar System objects for the following reasons (Halliday and Lee, 1999).

(1) The half-life of ^{182}Hf (8.9×10^6yr) is ideal for evaluating events that occurred up to ~50–60 Myr after the start of the Solar System.

(2) The initial abundance of ^{182}Hf was relatively high (^{182}Hf/^{180}Hf = 10^{-4}), so that the isotopic effects produced are easily resolved.
(3) Both Hf and W are refractory elements, so parent : daughter ratios and W isotope compositions of bulk planets are usually chondritic, and hence well defined.
(4) Both Hf and W are strongly fractionated during core segregation, which is considered to be an early process in planetary evolution. Hf, a strongly lithophile element, is retained in the silicate portion (mantle) of a planet or planetesimal, whereas W, a moderately siderophile element, is largely partitioned into a coexisting metallic phase (core). Consequently, if core formation took place when the Earth still had some ^{182}Hf, the W remaining in the silicate mantle would eventually develop an excess abundance of ^{182}W relative to that of chondrites. Conversely, if core formation was late, after (practically) all ^{182}Hf had decayed, the W isotope composition of the silicate Earth would be identical to that found in chondrites.

The slight excess ^{182}W/^{183}W ratio observed in the bulk silicate Earth compared to chondrite samples (Yin *et al.*, 2002; Kleine *et al.*, 2004) implies that segregation of the Earth's core occurred within a relatively short interval after the formation of the Solar System, during the life-time of ^{182}Hf. Modeling of the W-isotope composition of BSE as a function of time indicates that the bulk of metal–silicate separation (i.e., core–mantle differentiation) in the proto-Earth was essentially completed within < 30 Myr of the Solar System formation (Yin *et al.*, 2002; Kleine *et al.*, 2002, 2004). These results are consistent with other lines of evidence for rapid planetary formation (Lugmair and Shukolyukov, 1998), and are also in agreement with dynamic accretion models that predict a relatively short time (~10 Myr) for the main growth stage of terrestrial planet formation (Wetherill, 1986).

Formation of the Moon: the giant impact hypothesis

The last major growth stage of the Earth's core formation is defined by the age of the Moon. The most widely accepted model for the origin of the Moon at present is based on the so-called *giant impact hypothesis* (Hartman and Davis, 1975) – the off-center impact delivered by a Mars-sized planetary body (sometimes referred to as Theia) of approximately chondritic composition with the Earth, when the Earth had acquired about 90% of its final mass.

^{182}Hf—^{182}W isotope data indicate that the Moon formed 30–50 Myr after the start of the Solar System, the exact age being dependent on the model deployed (Halliday and Kleine, 2006). The most commonly quoted date is 45 ± 5 Ga (Halliday, 2003; Kleine *et al.*, 2004), which is almost the same as the Moon's Rb–Sr age, 4.48 ± 0.02 Ga (Halliday, 2008). The impactor and the Earth are assumed to have already differentiated by that time into a metallic core and a metal-poor silicate mantle. Hydrodynamic simulations of the giant impact require that as much as 70–90% of the material forming the Moon came from the debris disk of vaporized silicate mantle of the impactor (not from the terrestrial mantle), and the metallic core of the impactor accreted to the Earth contributing the final ~10% of the Earth's mass (Canup and Asphaug, 2001; Canup, 2004; Pahlevan and Stevenson, 2007). Calculations indicate that the Moon could have formed from the impact debris in 10 yr or less, certainly in no more than 100 yr. The impact model explains the angular momentum of the Earth–Moon system (the spin of each, plus the orbital motion of the Moon around the Earth), the volatile-poor and refractory-rich composition of the Moon, and its iron-depleted bulk composition. The Moon has only a tiny metallic core, and estimates of its iron abundance vary between 8 and 12% compared to about 31% for the Earth (McSween and Huss, 2010).

Wiechert *et al.* (2001) showed that oxygen isotope compositions of lunar samples from Apollo missions define, within analytical uncertainties ($2\sigma = \pm 0.016$), a single mass-dependent fractionation line in a plot of δ^{18}O versus δ^{17}O, and it is identical to the terrestrial fractionation line within uncertainties. They attributed this congruence to isotopic similarity between the Moon-forming impactor and the proto-Earth. The problem is that most of the Moon material came from the impactor. For the impactor to have the same mix of primordial material as the Earth, we have to invoke the unlikely scenario of the two bodies growing at exactly the same distance from the Sun, being fed from the same part of the Solar Nebula, and having similar histories of core–mantle separation. Perhaps, as argued by Pahlevan and Stevenson (2007), the oxygen isotope composition was homogenized as a result of vigorous mixing between the Earth and the proto-lunar disk in the aftermath of the giant impact.

Calculations indicate that the energy released in such an impact would be enough to melt much of the impact debris, implying that the Moon would have formed very hot, possibly entirely molten (Canup, 2004; Pahlevan and Stevenson, 2007). This hot initial state is consistent with the decades-old idea that the Moon was surrounded by a "magma ocean" when it formed. The highly anorthositic composition of the lunar crust, as well as the existence of KREEP-rich lunar rocks (i.e., rich in K, REE, and P) are consistent with the idea that a large portion of the Moon was once molten, and a giant impact scenario could easily have supplied the energy needed to form such a "magma ocean." It is also likely that the Moon-forming impact, the last time that the Earth was hit by another planet-size body, led to the loss of the Earth's existing atmosphere, large-scale melting and vaporization of some of the Earth's mantle, and the formation of a terrestrial "magma ocean" engulfed in a rock-vapor atmosphere (Koeberl, 2006; Zahnle, 2006; Pahlevan and Stevenson, 2007; Wilson, 2008).

Homogeneous versus heterogeneous accretion models

Over the years, much of the debate about the mechanism of the Earth's accretion and its differentiation into a primitive mantle and core has focused on two end-member models (Fig. 12.11): (i) *homogeneous accretion* and (ii) *heterogeneous accretion*.

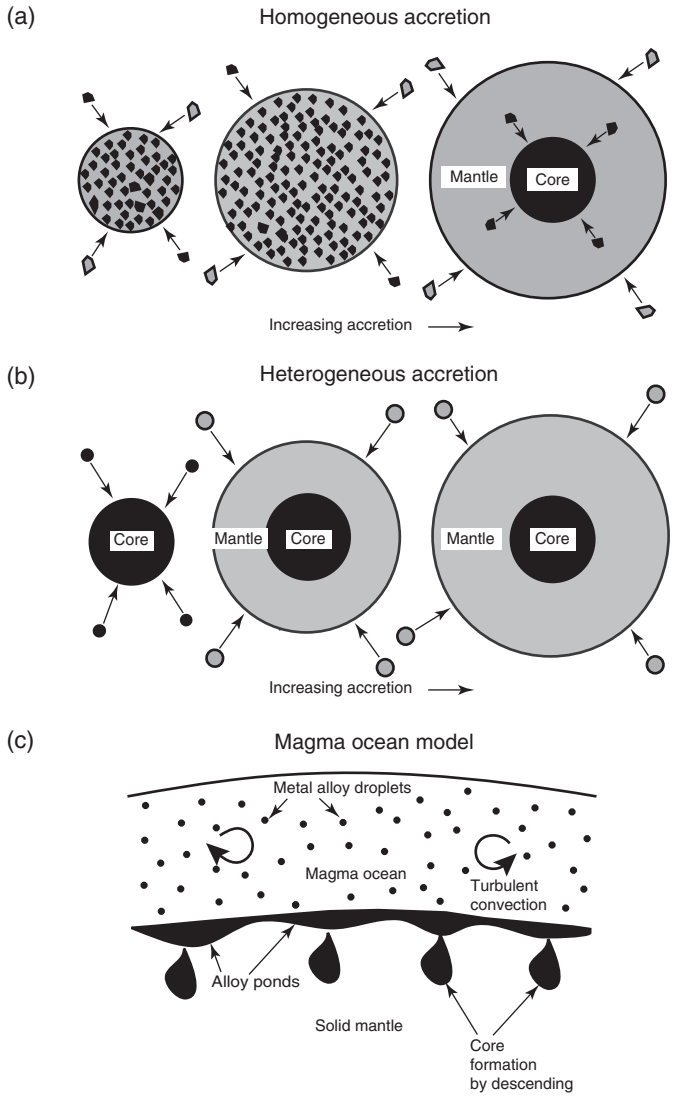

Fig. 12.11 Schematic illustration of models proposed for the formation of the Earth's metallic core and silicate mantle (BSE). (a) Homogeneous accretion, a two-stage process consisting of the accretion of a homogeneous (undifferentiated) proto–Earth and its subsequent differentiation into metallic core and silicate mantle. (b) Heterogeneous accretion, which envisions contemporaneous accretion and differentiation of material that changed from reducing to oxidized with time (followed by the addition of a "late veneer" after the core formation). (c) "Deep magma ocean" model of core formation. Small metal alloy droplets settle rapidly through the strongly convecting silicate liquid, accumulate as ponds of molten alloy at the bottom of the magma ocean, and equilibrate with the surrounding silicate material before descending as diapirs into the growing core.

Both models, neither of them totally satisfactory, assume that the Earth is made of extant meteoritic material that originated in the asteroid belt; the main difference between them lies in the timing and mechanism of metal–silicate separation.

According to the homogeneous accretion model (Ringwood, 1979), condensation of the Earth material from the solar nebula gas was essentially complete before accretion began. The temperature of the nebula is assumed to decrease outward from the Sun, and the composition of the condensate was a function of the distance from the Sun. The solids so formed accreted to form various planets without getting involved further in reactions with the gas; any uncondensed materials were somehow flushed from the system. The Earth accreted as a cool, homogeneous and undifferentiated mixture of silicates and metals, but became molten soon after accretion due to meteorite bombardment, gravitational compression, and radioactive decay of mainly short-lived radionuclides such as ^{26}Al, ^{182}W and ^{142}Nd (especially ^{26}Al), and differentiated internally into the core–mantle structure. The heavier metals (predominantly Fe and Ni) percolated downwards, eventually forming large dense accumulations that sank rapidly towards the center to form the core (Elsasser, 1963; Walter and Tronnes, 2004). Problems with this model, which satisfactorily accounts for planetary mean densities, are as follows (McSween *et al.*, 2003): (i) it is unrealistic to assume that a large planet would accrete only condensates formed at single temperature; and (ii) the planets Venus, Earth, and Mars should have no atmosphere because no condensed volatiles are possible at the condensation temperatures for these planets.

The heterogeneous accretion model, originally proposed by Turekian and Clark (1969), envisages planetary growth by simultaneous condensation and accretion of various compounds as the temperature fell inside an originally hot Solar Nebula. The model is based on the premise that all solids were vaporized in a hot Solar Nebula prior to condensation, and each new condensate was accreted as soon as it formed, preventing its subsequent reaction with the vapor. The planet grew by accretion of chondritic material that became more oxidizing with time. The result was a layered planet – the most refractory material (e.g., Fe + Ni), which would condense first out of a hot nebular gas, accreted forming a single metallic core. This was followed by condensation of less refractory silicates at lower temperatures and addition of this material, in layers, to generate an iron-rich core overlain by the primitive mantle composed of silicates, and finally an atmosphere composed of volatile phases. The heterogeneous accretion hypothesis has been widely accepted, but advances in our understanding of the accretion process have made this hypothesis less viable (Righter, 2003).

Let us examine how the heterogeneous accretion model fits the available geochemical data. It is reasonable to expect that refractory elements were accreted to all planets in cosmic or average solar system abundances (corrected for volatility as described by Newsom and Sims, 1991). The differentiation of a planet into mantle and core would partition trace elements according to the their distribution coefficients under planetary conditions of temperature, pressure, oxidation state, and compositions of the core and mantle, the distribution coefficient of an element i between molten alloy (core) and silicate (mantle) being defined as (see Box 5.6)

$$D_i^{\text{alloy–silicate}} = C_i^{\text{alloy}}/C_i^{\text{silicate}} \qquad (12.33)$$

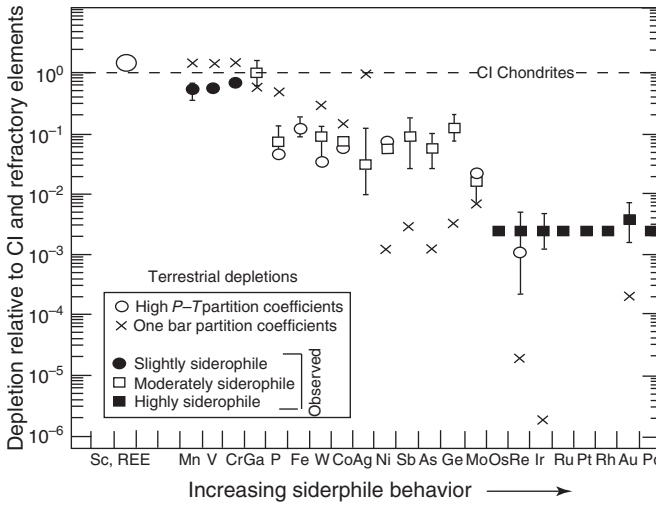

Fig. 12.12 "Stair-step" pattern observed for the depletion of siderophile elements (normalized to CI carbonaceous chondrites and refractory elements) in the Earth's primitive upper mantle. For highly and moderately siderophile elements, the abundances are greater than those calculated using partition coefficients between a peridotite magma and metallic liquid measured at 1 bar pressure and 1200°C–1600°C. This discrepancy is commonly referred to as the "excess siderophile element problem." Calculations using high *P–T* (270 ± 60 kbar; 2250 ± 300 K) partition coefficients overlap the observed depletions for moderately siderophile elements and Re, consistent with metal–silicate equilibrium and homogeneous accretion. The depletions of Ga, Sn, and Cu are due entirely to volatility rather than core formation (After Drake and Righter, 1997, Figure 1, p. 542.)

where C_i^{alloy} and C_i^{silicate} are the concentrations of i in weight per cent (or ppm) in the metal alloy liquid and silicate liquid, respectively. However, as shown in Fig. 12.12, the abundances of moderately siderophile (P through Ge) and highly siderophile (Os through Pd) elements in the BSE are too high to be consistent with metal (core)–silicate (BSE) equilibrium based on distribution coefficients measured at low pressure (1 bar) and moderate temperature (1200°C–1600°C). This observation has come to be known as the "excess siderophile element problem" (Ringwood, 1966). Actually, the term is somewhat misleading because some of the moderately and slightly siderophile elements are actually less abundant than predicted by their partition coefficients (Fig. 12.12).

Wänke (1981), a proponent of the heterogeneous accretion model, addressed the stair-step pattern of siderophile elements by suggesting that the material accreting to the Earth changed in composition and oxidation state in time (Fig. 12.11b). The first 80% to 90% of the material was very reducing, so that all elements included in Fig.12.12, except the refractory lithophile elements such as Sc and REE, were quantitatively extracted into the core, and the mantle became almost devoid of Fe^{2+}. The next 20% to 10% or so of the accreting material was more oxidized (such as Fe, Co, Ni, Ga, W, Zn, Ge as oxides) and contained elements of moderately volatile character (such as Na, K, Rb, F) in chondritic abundances. The admixture of a small amount (< 1%) of metallic iron and segregation of this metal was responsible for the extraction of highly siderophile elements (Ir, Os, Au, etc.), and possibly also S and chalcophile elements, present in this material to the core, leaving other elements stranded in the mantle. Icy planetesimals (richer in volatiles such as H_2O, halogens, and CO_2), added the last 1% or so of the accreting material, the so-called "late veneer," after core formation had ceased. This material was too oxidizing to coexist in equilibrium with metallic iron, and all the siderophile elements delivered by the "late veneer" were forced to stay in the mantle, where they were thoroughly homogenized. The term "late veneer," although entrenched in the literature, is misleading, as the last dregs of material accreted to the Earth are well mixed into at least the upper mantle and perhaps the entire mantle, rather than veneering the surface (Drake and Righter, 2002).

The heterogeneous accretion hypothesis makes dynamical sense in that the "feeding zone" of the Earth's accretion must have extended further out from the Sun with the growth of the planet, but the zonal structure of the Earth could not have been predicted from condensation temperatures of earth materials because of the large degree of overlap. Also, according to this model, there should be much more sulfur in the Earth's mantle and Ga (which should have behaved like Ni) in the core than estimated (Drake, 2000).

Magma ocean hypothesis

There is general agreement that the Earth experienced large-scale melting and developed, probably multiple times, one or more magma oceans late in its accretion. The melting was an inevitable consequence of the heating due to collisions among the accreting planetesimals, radioactive decay of short-lived nuclides within the first few million years of Solar System history, and the greenhouse effect of the evolving atmosphere (see section 13.3.3). The last global-scale terrestrial magma ocean probably resulted from the Moon-forming giant impact. The oxygen isotope homogeneity observed in meteorites (angrites, eucrites, and lunar and Martian meteorites) and terrestrial samples is consistent with the involvement of magma oceans in the Earth's evolution (Greenwood *et al.*, 2005). The Earth most likely accreted heterogeneously, with material composition changing with time, but we have not found any evidence for it. It appears that the magma ocean(s) homogenized the pre-existing material, thus obliterating any record of heterogeneous accretion, with the possible exception of the "late veneer" of highly siderophile elements that was added later than core formation (Drake and Righter, 2002).

Accretion followed by magmatic processes in a deep, high *P–T* magma ocean environment offers a reasonable explanation for the Earth's bulk geochemical properties. The essence of the "deep magma ocean" hypothesis (Murthy, 1991; Li and Agee, 1996; Righter and Drake, 1997, 1999; Drake, 2000; Rubie *et al.*, 2003; Wade and Wood, 2005; Righter, 2007) is that droplets (of diameter of about 1 cm and a settling velocity of about 0.5 m s^{-1}, according to Rubie *et al.*, 2003) of metallic liquid descended

through a deep magma ocean, equilibrating with the silicate at high temperatures and pressures as they fell. Experimental studies have shown that metal–silicate partition coefficients of siderophile elements, such as Ni and Co, are significantly reduced at elevated temperatures and pressures (Li and Agee, 2003). The liquid metal ponded in pockets at the base of the magma ocean, which extended approximately to the base of the current upper mantle, and subsequently descended rapidly as large diapers to the growing core without further equilibration with the surrounding silicate material (Fig. 12.11c). Modeling suggests a short duration, in the order of 1000 yr, for metal–silicate equilibration and magma ocean crystallization (Rubie *et al.*, 2003), and the short timeframe is consistent with W–Hf dates for Moon formation around 4540 Ma. The principal objection to this model is the improbability that one set of P–T conditions can satisfy the mantle abundances of all elements.

As summarized in Righter (2003), estimates of the temperature and pressure at the base of the magma ocean, based on experimental determination of partition coefficients of many of the excess siderophile elements (Mn, V, Cr, P, Fe, W, Co, Ni, Mo, Re) between metal alloy liquid and a hydrous peridotite magma, range from 2000 K to 4000 K and 25 GPa to 60 GPa, at an oxygen fugacity about 2 log units below that of the iron–wüstite buffer (Li and Agee, 1996; Chabot and Agee, 2003; Righter, 2003; Chabot *et al.*, 2005). Assuming that the core formed by a single-stage process, Wade and Wood (2005) determined that the mantle concentrations of the refractory elements could be matched at a temperature of 3750 K and a pressure of 40 GPa. At 40 GPa, however, the calculated equilibrium temperature turned out to be about 1000 K above the peridotite *liquidus* (the boundary curve on a phase diagram, representing the onset of crystallization of a liquid with lowering temperature). This is an implausible scenario because the base of the magma ocean, where the metal would pond during accretion, must be saturated in crystals and should, therefore, lie at or below the peridotite liquidus. Forcing the temperature to lie on the peridotite liquidus as the Earth grew, Wade and Wood (2005) could match the mantle concentrations of refractory elements provided oxygen fugacity increased during accretion. They proposed that as the Earth continued to grow by accretion, Mg-perovskite (which is stable below 660 km in the present-day Earth and is the principal phase in the lower mantle) started to crystallize at the base of the magma ocean, and the mantle became increasingly more self-oxidizing through cycles of dissolution and reprecipitation of Mg-perovskite as described below.

In peridotite compositions, Mg-perovskite accommodates about 5% Al_2O_3, the charge balance being maintained by the coupled substitution

$$Mg^{2+}\,Si^{4} \Leftrightarrow Fe^{3+}\,Al^{3+} \qquad (12.34)$$

This substitution mechanism is so stable that it forces ferrous iron (Fe^{2+}) to disproportionate to ferric iron (Fe^{3+}) and iron metal (Fe^{0}):

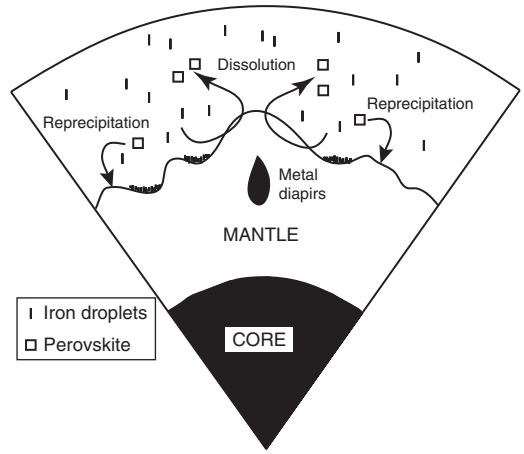

Fig. 12.13 Formation of the Earth's core accompanied by mantle "self-oxidation" as a result of perovskite precipitation at the base of the terrestrial magma ocean. The repeated crystallization and dissolution of Fe^{3+}-containing perovskite (due to fluctuating depth of the magma ocean) acted as a Fe^{3+} "pump," raising progressively the oxygen fugacity of the magma ocean from which the mantle grew by crystallization. (After Wade and Wood, 2005, Figure 10, p. 92.)

$$3Fe^{2+}\ (\text{in silicate}) \Leftrightarrow 2Fe^{3+}\ (\text{in perovskite}) + Fe^{0} \qquad (12.35)$$

Stated in terms of oxide components of the lower mantle, perovskite that crystallized from the magma ocean (silicate melt) dissolved Fe^{3+} as the $Fe^{3+}\,AlO_3$ component and released Fe^{0} in the process:

$$3Fe^{2+}O + Al_2O_3 \Leftrightarrow \underset{\text{perovskite}}{2Fe^{3+}\,AlO_3} + \underset{\text{metal}}{Fe^{0}} \qquad (12.36)$$

The depth of the magma ocean fluctuated continuously, generating fronts of dissolution and precipitation of perovskite (which is stable above 23 GPa) at its lower boundary (Fig. 12.13). The repeated dissolution, which released Fe^{3+} to the magma ocean, and precipitation, which produced more Fe^{3+} (reaction 12.36), resulted in a progressive oxidation of the magma ocean. Later droplets of metal falling through the magma ocean reacted with Fe^{3+}, driving reaction 12.36 to the left and producing more Fe^{2+} that dissolved in the magma ocean and was available for disproportionation to Fe^{3+} and Fe^{0}. Thus, oxidized iron (Fe^{3+}) content in the magma ocean (mantle) increased as a consequence of perovskite crystallization, raising the oxygen fugacity of core metal–silicate equilibration. In the very final stages of the Earth's accretion, this mechanism may have caused sufficient oxidation to halt metal segregation to the core, thus setting the stage for the "late veneer" to establish the mantle contents of highly siderophile elements.

The deep magma ocean hypothesis is also compatible with partitioning of light elements such as silicon into the metallic core. Gessman *et al.* (2001) and Malavergne *et al.* (2004) have shown that silicon solubility in iron–alloy melt is enhanced at high pressures.

12.2.4 Formation and growth of the Earth's crust

Many questions regarding the formation and evolution of the Earth's crust have not been resolved. When did the first crust form? Was the earliest crust ultramafic, mafic, or felsic? How were continental and oceanic crusts extracted from the mantle? Did the crusts grow continuously or episodically? Here is a brief summary of what we know about answers to these questions.

The earliest crust

We really do not know the nature of the earliest crust, but comparison with other planets suggests that the Earth's first or primary crust was basaltic in composition like modern oceanic crust. At present, new oceanic crust is created predominantly at spreading ridge axes, from basaltic melts generated directly from the upper mantle by partial melting, and recycled into the mantle by subduction at continental margins. The earliest oceanic crust probably formed and was recycled the same way. However, as the Earth's oldest oceanic crust is only about 200 Ma old, and no remnants of Hadean or Archean oceanic crust (e.g., in the form of ophiolites, which are interpreted as obducted oceanic crust) have yet been identified, we have no direct evidence regarding the nature of oceanic crust in the early Earth. It is reasonable to speculate that early oceanic crust probably crystallized from a magma ocean soon after planetary accretion and, like modern oceanic crust, it probably was widely distributed on the Earth's surface. Because of the greater amount of heat in the Archean upper mantle, oceanic crust may have been produced at a considerably faster rate than at present, and thus probably was much thicker than the modern oceanic crust (Condie, 1997). Russell and Arndt (2005) suggested that a high degree of partial melting of hot, dry Hadean (> 3.8 Ga) mantle at ocean ridges and in plumes resulted in an oceanic-type crust about 30 km thick, overlain at places by extensive and thick mafic volcanic plateaus.

The continental crust, because of its diversity, is a much more complex system compared to the oceanic crust, but preserved remnants of continental crust (granitic) are much older. The earliest continental crust must have formed by partial melting of the primitive mantle, with incompatible elements (such as Cs, Rb, K, U, Th, and La) mostly segregated into the partial melts. Much of the key evidence regarding the earliest continental crust has been lost owing to repeated erosion, metamorphism, tectonism, and remelting. It has been possible, however, to reconstruct the age of the earliest mantle–crust differentiation by isotopic studies, all of which point to a very early formation of the first crustal rock. The Earth's oldest known *in situ* crustal units, which comprise less than 10% of preserved Archean crust, are mainly of tonalitic gneisses containing fragments of komatiite (high-Mg basalt) and amphibolite (metamorphosed basalt), some of which may be remnants of early oceanic crust. These units have been dated to 3.8–4.0 Ga (e.g., Baadsgaard *et al.*, 1984; Bowring and Williams, 1999), leaving a gap of more than 500 Myr in the crustal record, considering that the surfaces of the Moon, Mars, and Mercury reveal crater-saturated regions of ~4.5 Ga "primordial" crust.

Evidence of crust older than 4.0 Ga – actually as old as ~4.4 Ga – is provided by U–Pb ages of the cores of some isolated, detrital zircon crystals from ~3.0-Ga-old metasedimentary rocks of the Yilgarn Craton, Western Australia (Froude *et al.*, 1983; Compston and Pidgeon, 1986; Wilde *et al.*, 2001; Mojzsis *et al.*, 2001; Valley *et al.*, 2002; Cavosie *et al.*, 2005; Nemchin *et al.*, 2006). The zircon crystals are interpreted to have been derived from granitic terranes, suggesting that at least small amounts of proto-continental crust existed by ~4.4 Ga (only about 200 Myr later than the end of Earth's accretion). Without such buoyant crust, the zircon-bearing sediments would have sunk into the mantle and assimilated. Grieve *et al.* (2006) calculated that pockets of felsic crust could have been produced by differentiation of melts generated by early large-scale impacting of the basaltic crust. Analysis of Lu–Hf isotopes support the view that continental crust had formed by 4.4 to 4.5 Ga and was rapidly recycled into the mantle (Harrison *et al.*, 2005). Oxygen isotope ratios of > 4.0-Ga zircon crystals from Jack Hills in the Yilgarn Craton have been interpreted to represent the earliest evidence for oceans on the Earth (Peck *et al.*, 2001) (see section 13.5.1). According to this interpretation, the Earth during the Hadean eon (4.6–3.8 Ga) was most probably characterized by a thick basaltic crust covered by an ocean, with very little dry land (composed mostly of granitic rocks) under an atmosphere probably dominated by CO_2 and/or CH_4.

How did the earliest crust form? Again, we do not know with any certainty, partly because we do not know the nature of the primitive crust. Perhaps, the Earth's earliest crust formed the same way as that of the Moon, by crystallization differentiation and solidification of the deep magma ocean that once covered the entire surface. In lunar magma ocean, the crystallizing plagioclase separated by floating to the top, and is now represented by anorthositic lunar highlands; later, remelting of the olivine- and pyroxene-rich cumulates under reducing conditions produced the mare basalts. The most compelling evidence for this interpretation is provided by the strong europium depletion in mare basalts because of removal of Eu^{2+} (octahedral coordination ionic radius = 1.25 Å) from the magma ocean by easy substitution for Ca^{2+} (octahedral coordination ionic radius = 1.08 Å) in plagioclase. Thus, the negative Eu anomaly indicates that the source of mare lavas was melted under reducing conditions and had experienced plagioclase crystallization (Grove and Krawczynski, 2009).

A problem with invoking an analogous mechanism for the formation of the Earth's cust from a terrestrial magma ocean is the lack of evidence of a terrestrial anorthositic primitive crust. Even without a magma ocean, extensive melting of the upper mantle should have produced large pockets of peridotitic magma and patches of anorthositic crust by crystallization of such magma. Perhaps no anorthositic crust formed on the Earth because the Ca and Al contents of the terrestrial magma(s) were not high enough for plagioclase to be an early crystallization phase, or plagioclase that formed could not float to the

top of the hydrous terrestrial magma. If an anorthositic crust did form, then it has been completely destroyed by chemical weathering, leaving no remnants (Warren, 1989). Also, the terrestrial basaltic rocks do not show a Eu anomaly, perhaps because the terrestrial magma ocean was not reducing.

Preserved stratigraphic records in continental terranes as old as 900 Ma provide evidence that the currently operative plate tectonic paradigm has governed the evolution of the lithosphere at least since the late Precambrian (Kröner, 1977). Extending plate tectonics (see section 12.3) to the interpretation of older crustal history is highly controversial because many of the hallmarks of plate tectonics – obducted oceanic crust in the form of ophiolites, tectonic mélanges, high-level thrust belts, accretionary wedges, foreland basins, and low-temperature/high-pressure paired metamorphic belts – are absent in the Archean rock record. Hamilton (2003), for example, has argued that plate tectonics began only at about 2.0 Ga "when continents could stand above oceans and oceanic lithosphere could cool to subduction-enabling density and thickness." On the other hand, many authors (e.g. Moorbath, 1978; Sleep and Windley, 1982; Condie, 1997) contend that some mechanism of plate creation and recycling must have been operative to accommodate the large amounts of heat loss and vigorous convection in the early mantle. Thus, accretion of felsic crust on a limited scale could have occurred shortly after the solidification of the magma ocean. Many kimberlites contain eclogite xenoliths, which are interpreted by some authors to represent metamorphic products of subducted oceanic crust on the basis of their elemental and isotopic compositions (e.g., Helmstaedt and Doig, 1975; Jacob, 2004; Riches *et al.*, 2010). If this interpretation is correct, then the Archean age of some of these xenoliths makes a very powerful case for some form of plate tectonics operating in the late Archean Earth. As Cawood *et al.* (2006) have pointed out, there is mounting evidence in favor of the operation of modern-style subduction processes possibly as far back as the Hadean eon. The evidence includes: the discovery of Archean eclogites in the eastern Baltic Shield; the presence of late Archean subduction-related ("Kuroko-type") volcanogenic massive Cu–Zn–Pb sulfide deposits; the discovery of mid-Archean island arc volcanics; and the discovery of detrital zircon crystals attesting to the existence of at least some amount of proto-continental crust by 4.4 Ga. Some authors (e.g., Watson and Harrison, 2005; Cawood *et al.*, 2006) have suggested that the pattern of modern-style crust production, crust destruction, and sedimentary recycling, similar to the essential processes of plate tectonics, was probably operative as far back as the Hadean eon.

Composition of the continental crust

Matching of seismic wave velocities to lithology supports a threefold subdivision of the continental crust that gets more mafic with depth (Christensen and Mooney, 1995; Rudnick and Gao, 2004): an upper crust (~10 km thick) of granitic composition; a middle crust (~20 km thick) composed of a basalt (amphibolite)–granite mixture; and a lower crust (~10 km thick) of basaltic composition (mafic granulite). All segments of the continental crust are enriched in incompatible elements relative to the primitive mantle, and the upper crust is particularly enriched in LREE (Fig. 12.14). In addition, the upper crust has large negative europium and strontium anomalies that are largely complemented by the positive europium and strontium anomalies of the lower crust; the middle crust has essentially no europium anomaly. These features suggest that the upper granitic crust differentiated from the lower crust through partial melting, crystal fractionation (involving plagioclase in which Eu^{2+} and Sr^{2+} substitute easily for Ca^{2+}), and mixing processes (see section 12. 3). The middle crust has an overall trace-element pattern that is very similar to that of the upper crust, indicating that it too is dominated by the products of intracrustal differentiation (Rudnick and Gao, 2004). Based on observations of the rock types present in the upper continental crust and models of lower-crust composition, the average bulk composition of the continental crust is estimated to be andesitic, with SiO_2 = 57–64% and Mg# (defined as 100 × molar Mg/(Mg + ∑Fe)) between 50 and 56 (Rudnick, 1995).

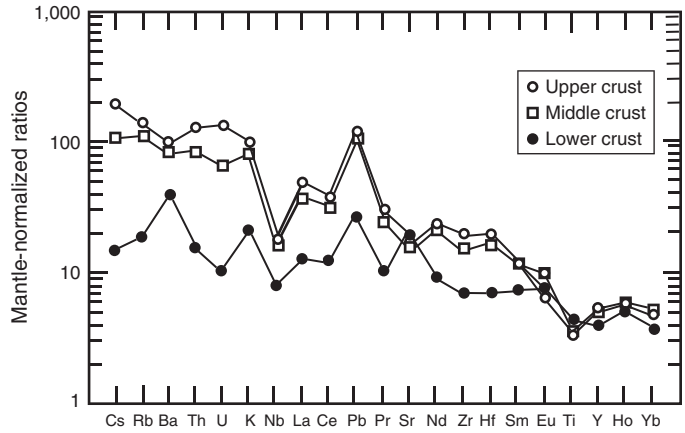

Fig. 12.14 Trace element (including REE) composition of the upper, middle, and lower continental crusts from Rudnick and Gao (2004), normalized to primitive mantle values from McDonough and Sun (1995). (After Rudnick and Gao, 2004, Figure 17b, p. 51.)

Average compositions of the continental and oceanic crusts relative to the primitive mantle composition form surprisingly complementary patterns (Fig. 12.15). In continental crust, concentrations of the most incompatible elements Rb, Ba, Th, and K reach 50 to 100 times the primitive mantle values but < 3 times primitive mantle values in the oceanic crust. In average oceanic crust (represented by "normal" MORB), the maximum concentrations are only about 10 times the primitive mantle values, and they are attained by the moderately incompatible elements Hf, Zr, Ti, Yb, Y, and the intermediate to heavy REE. The patterns cross at element P, and the least incompatible elements Ti, Yb, and Y are more enriched in oceanic crust than in continental crust. Relative depletions in Nb (resulting in characteristic low Nb/La and Nb/Ta ratios),

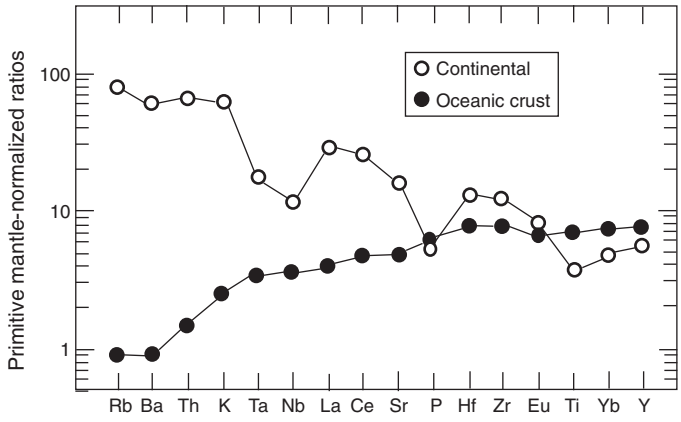

Fig. 12.15 Complementary patterns exhibited by concentrations of elements in the bulk continental crust (Condie, 1997) and "normal-type" mid-ocean ridge basalts (N-MORB) (Hofmann, 1988), both normalized to the estimated values for the primitive mantle (Sun and McDonough, 1989. The continental rust is enriched in incompatible elements and has a high La/Nb ratio, which are characteristic features of convergent margin magmas and rarely observed in intraplate magmas.

P, and Ti, and a strong relative enrichment in Pb are important features of continental crust. This lack of complementary relation between the continental crust and depleted mantle can be balanced by a refractory eclogite reservoir deep in the mantle, which formed by metamorphism of sinking slabs of oceanic crust in subduction zones and is enriched in Nb, Ta, and Ti (Rudnick *et al.*, 2000).

Growth of the continental crust

Hoffman (1988) argued that the compositional relationship between continental crust and oceanic crust could be explained by a simple (employing equilibrium partial melting), two-stage model of first extracting continental crust from the primitive mantle, and then extracting oceanic crust by remelting of the residual (depleted) mantle. Yet most high-pressure single-stage melting experiments conducted on mantle peridotite compositions have yielded magmas that are considerably less evolved (e.g., basalts and picrites) than the bulk continental crust (andesitic). Several models of crustal growth have been proposed to explain this paradox (see reviews in Rudnick, 1995; Kelemen, 1995; Rudnick and Gao, 2004), all of which require the return of mafic-to-ultramafic lithologies to the convecting mantle, and thus assume crustal recycling to have been operative throughout the Earth's history.

The similarity between the composition of high-Mg# andesite (HMA) lavas (e.g., negative Nb–Ta anomalies) found in many contemporary magmatic arcs and the continental crust average, coupled with the occurrence of prolific andesite magmatism at continental convergent margin settings (such as the Andes and the Cascades), prompted Taylor (1967) to propose the "andesite model" of continental growth – that continental crust formed as a result of andesitic arc magmatism and was accreted to a preexisting crustal mass. The andesite model, however, cannot explain the higher Cr and Ni contents or Th/U ratio of the continental crust compared to HMA. Moreover, andesite magmatism is uncommon in volcanic sequences emplaced during the Archean when a substantial part of the present crustal mass is inferred to have formed. This led Taylor and McLennan (1985) to suggest that only post-Archean crustal growth was accomplished by island arc accretion, and growth of continental crust during the Archean probably occurred in intraplate settings in response to plume-related and continental rift magmatism. The recent discovery of andesites with negative Nb and Ta anomalies on the Pacific–Antarctic Rise implies that such magmas are not restricted to subduction zones but can form also at plume-influenced mid-oceanic ridge (Haase *et al.*, 2005). However, post-Archean crust of andesitic composition could not have been formed by accretion of intra-oceanic island arcs because they are estimated to have basaltic rather than andesitic bulk compositions. Magmas in continental arc settings, such as the Andes and the Cascades, are andesitic, presumably due to contamination from preexisting continental crust, but the primary magmas are estimated to have been basaltic, similar to those in intraoceanic settings.

A variation of the andesite model envisages the formation of HMA in the mantle beneath arcs through interaction between rising basaltic melts from mantle peridotite and silicic melts derived from subducted oceanic crust, and the direct addition of the HMA to continental crust. This process is likely to have been more prevalent in a hotter, Archean Earth and involve extensive silicic-melt–peridotite reaction as the slab melts traversed the mantle wedge (Kelemen, 1995). The model, however, suffers from the same shortcomings as the original andesite model – that intra-oceanic island arcs appear to have basaltic bulk compositions, and andesites are uncommon constituents of Archean-aged crust.

An alternative model (Arndt and Goldstein, 1989) proposes "delamination" of the lower continental crust to account for the andesitic composition of the continental crust. High-Mg# andesite may have formed by crustal differentiation of mantle-derived basaltic magmas, and the mafic/ultramafic residue of differentiation forming the lower crust transformed into eclogite during subduction of continental crust as a result of arc–continent collision. Being denser than upper mantle peridotite, the eclogite might have then sunk into the mantle ("delaminated"), leaving only andesitic differentiates in the crust (Kelemen, 1995).

Crustal growth rate

There are two diametrically opposing hypotheses to account for the growth of continental crust to its present dimensions. The first may be called a steady-state hypothesis, which proposes that the present mass of the crust formed almost immediately after the Earth's formation, after which the system reached a steady state of negligible crustal growth through a

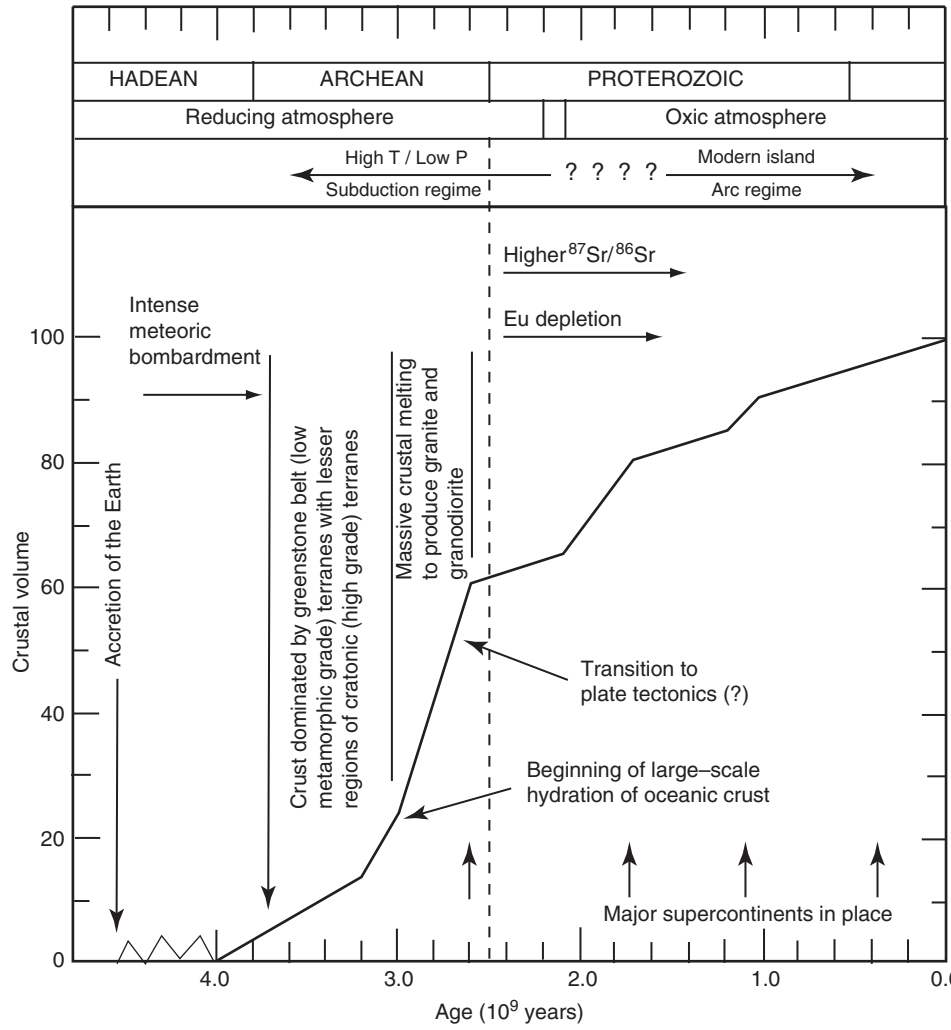

Fig. 12.16 Schematic model for the growth and evolution of the continental crust on a global scale as proposed by Taylor and McLennan (1995). The actual value of crust present at any given time is not well constrained, but a value of 50% crust by about 2.5 Ga is a likely minimum value. Although major global episodes of crustal growth and differentiation are well documented during the late Archean and at about 2.1–1.7 Ga, it is less clear if crustal growth is episodic on a global scale during younger times. In general, there appears to be a relationship between crustal growth episodes and assembly phases of supercontinents. (After Taylor and McLennan, The geochemical evolution of the continental crust, Rev. Geophysics and Space Physics, v. 33, p. 241-265, 1995. Copyright 1995 American Geophysical Union. Used by permission of American Geophysical Union.)

balance between new additions from the mantle and losses by erosion and by recycling via subduction (Armstrong, 1991; Bowring and Housh, 1995). The opposing hypothesis, which is more popular and more consistent with geochemical evidence, argues for episodic growth of continental crust over geologic time (Taylor and McLennan, 1981, 1995; Deming, 2002).

The episodic growth model of Taylor and McLennan (1995) presented in Fig. 12.16 shows that major pulses of continental growth occurred at about 3.8–3.5, 2.9–2.7, 2.0–1.7, 1.3–1.1, and 0.5–0.3 Ga, which appear to correlate reasonably well with phases of supercontinental assembly. During supercontinental assembly, subduction of old oceanic crust would be at a maximum, leading to an increase in arc volcanism. In addition, the continental collisions that terminated the assembly phases would promote crustal thickening, intracrustal melting and differentiation, granulite facies metamorphism, continental underplating, and, accordingly, preservation of such unsubductible crust in the geologic record.

Two striking features of the episodic growth model are particularly well constrained: the absence of significant amounts of continental crust prior to 3.0 Ga; and the most rapid growth of continental crust in the late Archean (2.9–2.7 Ga). At least 60% of the crust was emplaced by 2.7 Ga. There are at least three independent lines of geochemical evidence for this conclusion (Deming, 2002): (i) an abrupt increase in the $^{87}Sr/^{86}Sr$ ratio of ocean water at ~2.5 Ga, which is interpreted to represent the emergence of large continental land masses; (ii) the scarcity of zircons older than 3.0 Ga, and the abundance of 2.5 to 3.0 Ga zircons; and (iii) the absence of europium depletion in rocks older than 2.5 Ga.

The late Archean pulse corresponds to the Archean–Proterozoic transition. This transition was marked by widespread "cratonization" of the crust that involved massive intracrustal melting, resulting in the emplacement of large amounts of K-rich granitic rocks in the upper crust, transfer of heat-producing radioactive elements (K, U, and Th) to the upper crust, and stabilization of the crust. The Archean–Proterozoic boundary can also be correlated with many other geologic events. As summarized by Taylor and McLennan (1995), these include: the widespread occurrence of uranium

deposits in basal Proterozoic sediments because of enrichment of the upper crust in incompatible elements due to intracrustal melting; the dramatic increase in ^{87}Sr in the K-rich granites emplaced in the upper crust; and the proliferation of stromatolites and banded iron formations in the Proterozoic, attesting to the development of stable continental shelves.

12.3 Generation and crystallization of magmas

On the basis of tectonic setting, we can define four distinct plate-tectonic environments in which magmas may be generated (Fig. 12.17; Table 12.5): (i) constructive plate margins (spreading centers); (ii) destructive plate margins (subduction zones); (iii) oceanic intraplate settings; and (iv) continental intraplate settings.

The Earth's mantle is composed essentially of solid rocks, except perhaps a very small amount (< 1 wt%) of a melt phase in the asthenosphere. Partial melting resulting from heating of surrounding cold rocks by basaltic underplating may generate magmas locally in the continental crust and lithosphere, but *decompression melting* (pressure-release melting) and lowering of the *solidus* temperature (i. e., the temperature at which it will start to melt) by volatiles appear to be the major mechanisms of partial melting in the mantle. Partial melting beneath mid-oceanic ridges occurs in response to adiabatic decompression of ascending mantle peridotite in the zone of upwelling. The decompression-melting model is also applicable to mantle plumes that are believed to be responsible for intraplate magmatism. In subduction zones (located at convergent plate margins) magmas are generated by partial melting of the upper portion of the subducting oceanic crust and the overlying mantle wedge. As the slab of cold oceanic crust descends into the mantle by subduction, it is progressively heated by conduction of heat from the surrounding mantle and also possibly by frictional heating at the surface of the slab. The increasing temperature and pressure results in dehydrating an originally hydrous mineral assemblage in the slab and releasing aqueous fluids, which depress the melting points of silicate minerals and induce partial melting of the overlying mantle wedge (Fig. 12.18).

12.3.1 Geochemical characteristics of primary magmas

It is generally accepted that partial melting of upper mantle material produces magmas dominantly of mafic (basaltic) and ultramafic (picritic and komatiitic) compositions in most tectonic settings. Such magmas are called *primary magmas*, in contrast to *evolved* (or *derivative*) *magmas* generated through differentiation or mixing of primary magmas. Primary magmas appear to be generated within a very restricted depth range, within the upper 100–200 km of the mantle. Diamond-bearing kimberlites probably represent the deepest terrestrial magmas, originating from depths greater than 200–250 km. The geochemical characteristics of primary magmas depend upon parameters such as the source composition and mineralogy, and the depth, degree, and mechanism of partial melting – factors that vary from one tectonic setting to another. The wide spectrum of terrestrial igneous rocks is due partly to the varying composition of the primary magmas and partly to subsequent differentiation and assimilation processes. These

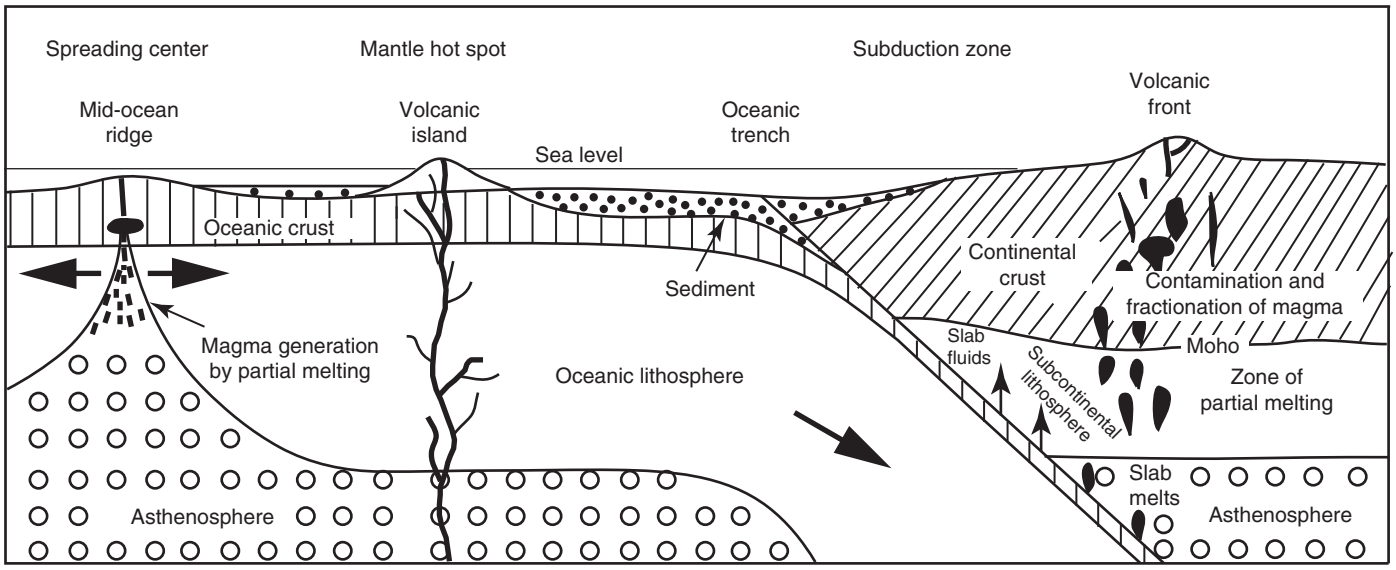

Fig. 12.17 Schematic composite diagram showing the different plate-tectonic environments of magma generation: (a) divergent plate margin (spreading center); (b) oceanic-plate–continental-plate convergent margin (subduction zone); and (c) oceanic intraplate setting (oceanic islands).

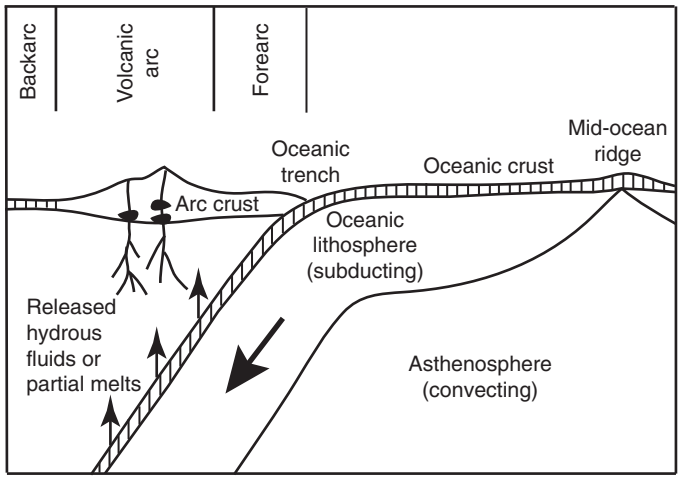

Fig. 12.18 Model of magma generation in a subduction zone marked by the convergence of two oceanic plates. The aqueous fluids released from the subducting oceanic crust due to metamorphic dehydration reactions enable partial melting of the overlying mantle wedge.

include fractional crystallization, magma mixing, and crustal contamination, either during the ascent of the magmas to higher levels or concurrently with crystallization (the so-called assimilation and fractional crystallization (AFC) process; DePaolo, 1981).

Basaltic rocks (SiO_2 = 44 – 53.5 wt%) are the most abundant type of volcanic rocks found within the accessible continental crust and are the overwhelmingly dominant volcanic rocks in the oceanic domain. On the basis of major element chemistry, primary basaltic magmas (and the resulting rocks) are divisible into three major *magma series* (e.g., Middlemost, 1975) – *tholeiitic*, *calc-alkaline*, and *alkalic* – each magma series comprising a genetically related spectrum of mafic to felsic rocks, as evidenced by the trends in their chemistry and mineralogy. Volcanic rocks of the alkalic group are silica-undersaturated, and can be distinguished from subalkalic rocks (which include tholeiitic and calc-alkaline magma series) by their higher alkali (Na_2O and K_2O) contents (Fig. 12.19a and b). The very low-K_2O, subalkalic basalts (Fig. 12.19b) are also depleted in other *large ion lithophile* (LIL) elements (such as Rb, Ba, U, Th, Pb, and LREEs). Some basalts plot within the alkalic field on the SiO_2–Na_2O diagram but within the subalkalic field on the SiO_2–K_2O diagram; such basalts are termed *transitional*. Komatiitic basalts (SiO_2 < 44 wt %) are low-K subalkalic basalts characterized by low Al_2O_3 and high MgO contents. Komatiitic basalts, however, can be readily separated from the low-K basalts of the present ocean floor, as komatiitic basalts normally contain more MgO than Al_2O_3, whereas the "ocean-floor basalts" normally contain more Al_2O_3 than MgO.

The subalkalic basaltic rocks, the most dominant type of volcanic rocks found in both the continental and oceanic domains, can be subdivided into a *tholeiitic series* and a *calc-alkaline* or high-alumina series (Fig. 12.19c). These two series can also be distinguished in terms of their differentiation trends on an AFM diagram (Fig. 12.20) – tholeiitic suites show a strong trend of iron enrichment because of crystallization of Fe–Ti oxides in the early stages of differentiation, which is followed by alkali enrichment. Calc-alkaline suites also show an alkali enrichment trend but no iron enrichment trend. Calc-alkaline basalts may be further subdivided into high-K, medium-K, and low-K types on a plot of SiO_2 versus K_2O (Fig. 12.19d).

At the present time, the calc-alkaline series is restricted to subduction-related tectonic settings, whereas alkalic basalts and their differentiates are commonly found in intraplate tectonic settings such as oceanic islands and continental rifts. The characteristic magma series associated with each of the tectonic settings in which primary magmas are generated are summarized in Table 12.6. Note that the distinction between tholeiitic and alkalic basalts, although important petrologically, does not appear to be correlated with tectonic setting.

12.3.2 *Behavior of trace elements during partial melting of source rocks*

Since the same kind of volcanic rocks occur in more than one tectonic setting (Table 12.6), the tectonic settings of primary basaltic magmas cannot be discriminated on the basis of major elements. We have to, therefore, depend on distributions of trace elements (including REEs) and Sr–Nd–Pb isotopic signatures for such discrimination.

Compatible and incompatible elements

The partitioning of a trace element *i* between a mineral and a melt at equilibrium is described by the *Nernst distribution coefficient* (see Box 5.6):

$$K_{D(i)}^{\text{mineral–melt}} = \frac{C_i^{\text{mineral}}}{C_i^{\text{melt}}} \tag{12.37}$$

where C_i^{mineral} and C_i^{melt} represent concentrations (e.g., in wt% or ppm) of *i* in the two phases.

Mineral–melt distribution coefficients are determined commonly from the analysis of minerals and their glassy matrix in rapidly cooled volcanic rocks, or from experiments at specified conditions in which synthetic or natural starting materials are doped with the trace element of interest. Values of distribution coefficients depend on a number of variables: composition of the melt, temperature, pressure, oxygen fugacity (especially for Eu), and crystal chemistry of the minerals. Published data on mineral–melt distribution coefficients are rather limited, and often we have to use approximate values for modeling calculations. Useful compilations of mineral–melt distribution coefficients can be found, for example, in Rollinson (1993), Lodders and Fegley (1998), and Salters and Stracke (2004). A compilation of

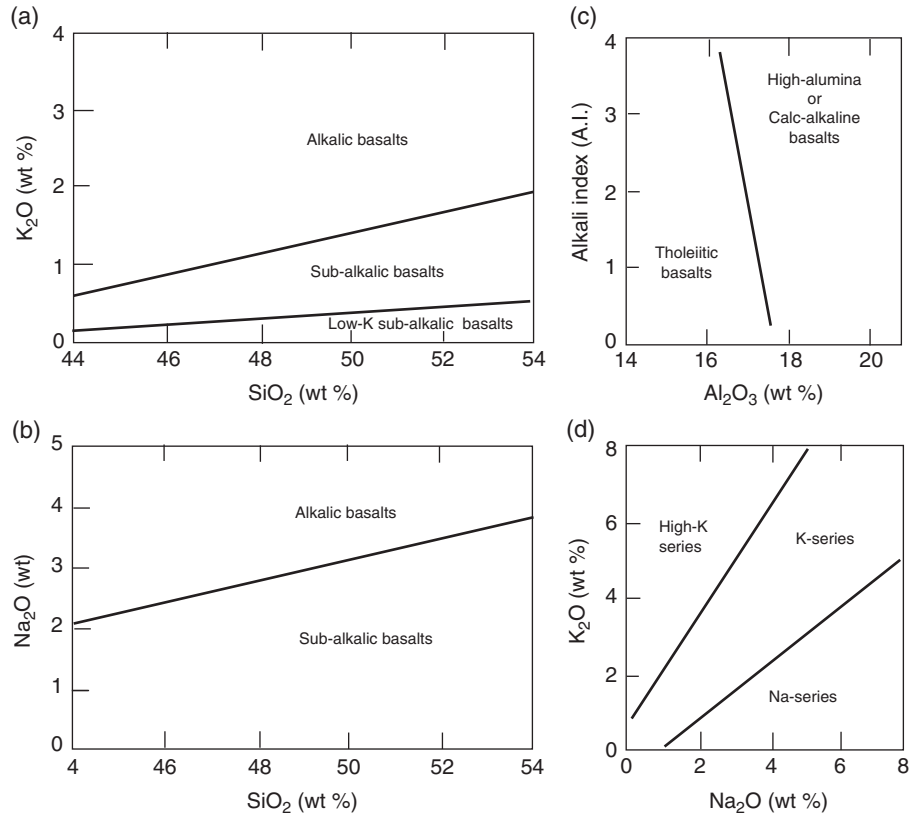

Fig. 12.19 Classification of primary basaltic magmas (after Middlemost, 1975; Wilson, 1989): (a) SiO_2 (wt%) versus K_2O (wt%); (b) SiO_2 (wt%) versus Na_2O (wt%); (c) alkali index (AI) versus Al_2O_3 (wt%); (d) SiO_2(wt%) versus K_2O (wt%). Alkali Index = $(Na_2O + K_2O) / [(SiO_2 - 43) \times 0.17]$.

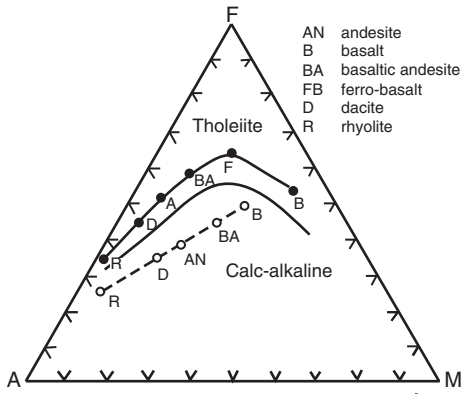

Fig. 12.20 AFM diagram showing typical tholeiitic and calc-alkaline trends of differentiation. A = $Na_2O + K_2O$; F = $FeO + Fe_2O_3$; M = MgO.

mineral–melt distribution coefficients appropriate for very Mg-rich (komatiitic) melts and useful for modeling the evolution of the lunar magma ocean and crust is given in Snyder *et al.* (1992). For the purpose of illustration, a few mineral–mafic melt distribution coefficients for REEs at specific temperature, pressure and oxygen fugacity conditions are listed in Table 12.7.

During partial melting and crystallization, trace elements with $K_{D\,(i)}^{\text{mineral–melt}} > 1$ are preferentially concentrated in the solid phases (minerals) and are called *compatible elements*, whereas trace elements with $K_{D\,(i)}^{\text{mineral–melt}} < 1$ are preferentially concentrated in the melt phase and are called *incompatible elements*. Some trace elements, however, exhibit variable behavior. For example, phosphorus behaves as an incompatible element during partial melting of mantle rocks and prefers the melt phase, but behaves as a compatible element during crystallization of granitic melts and is accommodated in the structure of the minor phase apatite.

Depending on the *field strength* (or *ionic potential*), which is defined as the charge : ionic radius ratio of an ion, incompatible elements may be divided further into two groups: *high field strength* (HFS) elements (such as lanthanides, Sc, Y, Th, U, Pb, Zr, Hf, Ti, P, Nb, and Ta) with ionic potential >2; and *low field strength* (LFS) elements (such as Cs, Rb, K, Ba, Sr, Pb, Eu^{2+}) with ionic potential <2. The LFS elements, along with the light rare earth elements La and Ce, are also referred to as LIL elements. The LIL elements are particularly concentrated in late-stage products of magmatic crystallization. Elements having small ionic radius and a relatively low charge (such as Ni, Cr, Cu, W, Ru, Rh, Pd, Os, Ir, Pt, and Au) tend to be

Table 12.6 Characteristic magma series associated with specific tectonic settings.

	Plate margin		Within-plate	
Tectonic setting	**Divergent (constructive)**	**Convergent (destructive)**	**Intra-oceanic**	**Intracontinental**
Volcanic feature	Mid-oceanic ridges; backarc spreading centers	Island arcs; active continental margins	Oceanic islands	Continental rift zones; continental flood-basalt provinces
	(Ocean-floor basalts)	(Volcanic-arc basalts)	(Ocean-island basalts)	(Continental basalts)
Characteristic magma series	Tholeiitic	Tholeiitic (low K_2O)	Tholeiitic	Tholeiitic
	–	Calc-alkaline (high Al_2O_3)	–	–
	–	Alkalic	Alkalic	Alkalic
Rock type	Basalts	Basalts and differentiates	Basalts and differentiates	Basalts and differentiates

Sources of data: Pearce and Cann (1973) and Wilson (1989).
Definitions of the three magma series included in this table are illustrated in Fig. 12.17.

Table 12.7 Nernst distribution coefficients, $K_{D\,(i)}$, for rare earth elements between some minerals and mafic silicate melt.

	Mineral									
Melt	**La**	**Ce**	**Nd**	**Sm**	**Eu**	**Gd**	**Dy**	**Er**	**Yb**	**Lu**
Diopside [T = 1265°C, P = 1 bar; –log f_{O_2} = 0.679 (for Eu, –log f_{O_2} = 10–16) (Grutzeck *et al*., 1974)]										
	0.69	0.098	0.21	0.26	0.31	0.30	0.33	0.30		0.28
Olivine [T = 1200°C, P = 1 bar; –log f_{O_2} = 12.4 (Kennedy *et al*., 1993)]										
	0.000028	0.000038	0.00020	0.00062	0.00015	0.00099	0.0039	0.0087	0.017	0.020
Plagioclase [T = 1150–1400°C, P = 1 bar; –log f_{O_2} = 0.679 (for Eu, –log f_{O_2} = 12.5 (Drake and Weil, 1975)]										
	(1)	(2)	(3)	(4)	(5)	(6)	(7)	(8)	0.035	(9)
Perovskite [T = 1150–1400°C, P = 1 bar; –log f_{O_2} = 0.679 (for Eu, –log f_{O_2} = 12.5 (Nagasawa *et al*., 1980)]										
	2.62			2.70	2.34	2.56			0.488	0.411

(1) ln $K_{D\,(La)} = -6.40 + 7000/T$; (2) ln $K_{D\,(Ce)} = -5.21 + 4600/T$; (3) ln $K_{D\,(Nd)} = -4.22 + 2920/T$; (4) ln $K_{D\,(Sm)} = -4.13 + 2340/T$; (5) ln $K_{D\,(Eu)} = -3.65 + 1560/T$; (6) ln $K_{D\,(Gd)} = -3.09 + 240/T$; (7) ln $K_{D\,(Dy)} = -1.54 - 2360/T$; (8) ln $K_{D\,(Er)} = -0.12 - 4620/T$; (9) ln $K_{D\,(Lu)} = -5.40 - 3200/T$.
T in Kelvin

compatible with minerals formed early in the crystallization process. Fig. 12.21 illustrates the distribution trends of a few trace elements in an island-arc tholeiite suite of volcanic igneous rocks formed by magmatic differentiation. The concentrations of compatible elements (e.g., Sr, Cr, Ni) generally decrease, whereas the concentrations of incompatible elements (e.g., Rb, Ba, Zr, Y) generally increase, with increased differentiation as indexed by increasing whole-rock SiO_2 content. Cr^{3+} (ionic radius 0.615 Å) and Ni^{2+} (0.69 Å) substitute easily for Mg^{2+} (0.72 Å) in early formed Mg-minerals (olivines and pyroxenes), and Sr^{2+} (1.18 Å) substitutes for Ca^{2+} (1.0 Å) in plagioclase. Rb^{+} (1.52 Å) and Ba^{2+} (1.35 Å) substitute for K^{+} (1.38 Å) in K-feldspars and, therefore, tend to be concentrated, along with K, in late differentiates. Zr^{4+} (0.72 Å) and Y^{3+} (0.70 Å) are concentrated at the felsic end of a differentiated series because their ionic size and charge make their substitutution for any major cations in common silicate minerals rather difficult. These elements are segregated into the late residual solutions, and if present in appreciable amounts they may form minerals of their own (e.g., zircon, $ZrSiO_4$).

Partial melting models

Depending on mineral–melt distribution coefficients, concentrations of trace elements in a mantle-derived partial melt, unlike those of the major elements, may be quite sensitive to the type of melting process and the degree of partial melting of the mantle source. There are two ideal or end-member models for the partial melting process.

(1) *Equilibrium partial melting* (or *batch melting*), in which the partial melt forms continually and equilibrates thermodynamically with the solid residue at the site of melting until mechanical conditions allow the melt to be removed as a single "batch." Up to this time the bulk composition of the source-rock–melt system remains the

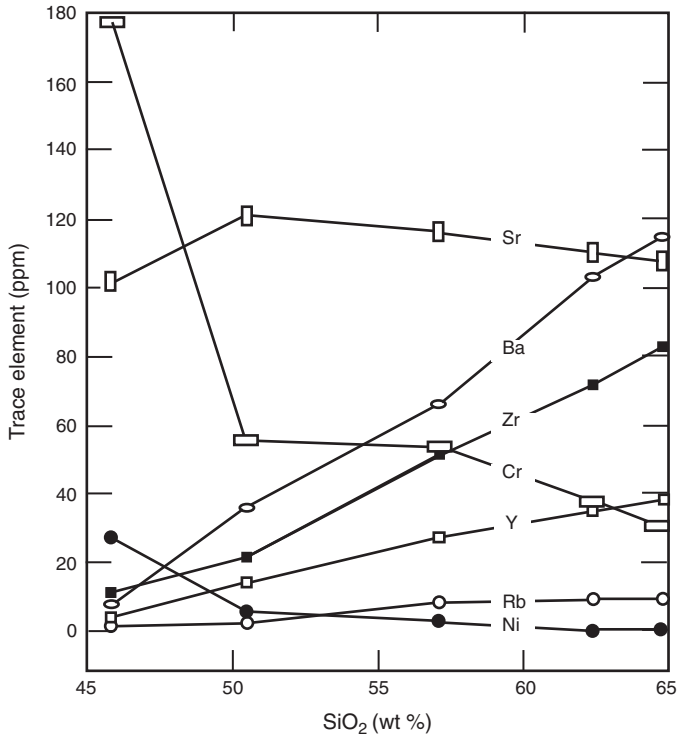

Fig. 12.21 Distribution trends of selected trace elements in a mafic-to-felsic differentiated suite of volcanic igneous rocks from South Sandwich island arc. The rock types of the suite are: basalt 1 (SiO_2 = 45.8%); basalt 2 (SiO_2 = 50.49%); basaltic andesite (SiO_2 = 57.1%); andesite (SiO_2 = 62.39%); and dacite (SiO_2 = 64.81%). In this system, Cr, Ni, and Sr are compatible elements, whereas Ba, Rb, Zr, and Y are incompatible elements. (Source of data: Luff, 1982.)

same as at the start, although the compositions of the partial melt and the solid residue change progressively with partial melting.

(2) *Fractional partial melting* (or *Rayleigh melting*), in which the small amount of partial melt formed at any instant may be in equilibrium with the solid residue, but is immediately and continuously removed from the source-rock–melt system, thereby preventing further interaction with the solid residue. For this process the bulk composition of the system changes continuously along with the compositions of the partial melt and the solid residue.

Which partial melting process is appropriate in a particular situation depends on the permeability threshold of the source? Which determines the ability of a partial melt to segregate from its source region? Because of the requirement of immediate melt removal, fractional melting can occur only if the mantle becomes permeable at very low degrees of partial melting (generally in the order of 1% or less, but may be up to about 2–3%). Thus, fractional melting may be an appropriate model for generation of some mafic melts, whereas batch melting may be the appropriate process for generating felsic melts, which are more viscous and, therefore, have a higher permeability threshold. Also, considering that the removal of infinitesimal amounts of melt is physically unlikely, batch melting may be the more geologically realistic model for the formation of large bodies of magma of uniform composition. An alternative model would be to allow thorough mixing of melt increments collected in a common reservoir, in which case the results for fractional melting would be indistinguishable from batch melting for highly incompatible trace elements.

For both melting processes, the concentration of a trace element *i* in the partial melt depends on whether the melting is *modal* or *nonmodal*, the degree of partial melting, and the appropriate *bulk distribution coefficient* of the residual solid at the moment when melt is removed from the system. The underlying assumption in all geologically relevant melting models is that the distribution coefficients remain constant throughout each melting event irrespective of changing melt composition and temperature.

Modal and nonmodal melting

In modal melting, the minerals melt according to their modal proportions in the source assemblage so that their weight fractions, and therefore the bulk distribution coefficient, ($D^{\text{rock}}_{0(i)}$), remain the same as for the source rock at the onset of melting, until one of the minerals is completely consumed as melting progresses. For example, in the partial melting of mantle rocks, minor phases such as garnet, amphibole, biotite, and clinopyroxene would, in general, be consumed much earlier than olivine and orthopyroxene. $D^{\text{rock}}_{0(i)}$ is the weighted mean of the individual mineral distribution coefficients for the element *i*, and is calculated as

$$D^{\text{rock}}_{0\,(i)} = W^{\alpha}_{0}\ K^{\alpha\text{–melt}}_{\text{D}\,(i)} + W^{\beta}_{0}\ K^{\beta\text{–melt}}_{\text{D}\,(i)} + W^{\gamma}_{0}\ K^{\gamma\text{–melt}}_{\text{D}\,(i)} + \ldots = \sum_{\alpha} W^{\alpha}_{0}\ K^{\alpha\text{s–melt}}_{\text{D}\,(i)} \qquad (12.38)$$

where W^{α}_{0} is the weight fraction of the mineral α in the source rock, and $K^{\alpha\text{-melt}}_{D(i)}$ is the α-melt distribution coefficient for the element *i*, and so on for the other phases in the source rock undergoing partial melting. For example, the bulk distribution coefficient of Ni in a hypothetical source rock containing 30 wt% olivine, 20 wt% orthopyroxene, and 50 wt% clinopyroxene, would be

$$D^{\text{rock}}_{0(\text{Ni})} = 0.3\,K^{\text{ol-melt}}_{D(i)} + 0.2K^{\text{opx-melt}}_{D(\text{Ni})} + 0.5K^{\text{epx-melt}}_{D(\text{Ni})}$$

Evidently, $D^{\text{rock}}_{0(i)}$ must be recalculated every time one or more of the minerals in the initial assemblage gets consumed completely by melting.

In the more realistic case of nonmodal melting (which is also more difficult to quantify), the proportions of the minerals entering the melt change continuously in the course of partial melting. For a particular value of F, the weight fraction

of melt formed (equivalent to the degree of partial melting), the bulk distribution coefficient, D_i^{bulk}, is (Wilson, 1989)

$$D_i^{\text{bulk}} = \frac{D_{0\,(i)}^{\text{rock}} - FP}{1 - F} \tag{12.39}$$

If $p^\alpha, p^\beta, p^\gamma, \ldots$ represent the weight fractions of phases entering the melt, then

$$\begin{aligned} P &= p^\alpha\ K_{\text{D}\,(i)}^{\alpha-\text{melt}} + p^\beta\ K_{\text{D}\,(i)}^{\beta-\text{melt}} + p^\gamma\ K_{\text{D}\,(i)}^{\gamma-\text{melt}} + \ldots \\ &= \sum_\alpha p^\alpha\ K_{\text{D}\,(i)}^{\alpha-\text{melt}} \end{aligned} \tag{12.40}$$

Note that the value of P, and therefore the concentration of i in the melt, is unaffected by any change in the mineralogy of the source rock that may have occurred prior to the instant under consideration.

Equations for batch and fractional melting

Equations for calculating the concentration of a trace element i in the partial melt, C_i^{melt}, relative to that in the original source rock, $C_{0(i)}^{\text{rock}}$, are as follows (Wood and Fraser, 1976; Allègre and Minster, 1978):

Batch melting (Fig. 12.22)

Modal
$$\boxed{\frac{C_i^{\text{melt}}}{C_{0\,(i)}^{\text{rock}}} = \frac{1}{D_{0\,(i)}^{\text{rock}} + F(1 - D_{0\,(i)}^{\text{rock}})}} \tag{12.41}$$

Nomodal
$$\boxed{\frac{C_i^{\text{melt}}}{C_{0\,(i)}^{\text{rock}}} = \frac{1}{D_{0\,(i)}^{\text{rock}} + F(1 - P)}} \tag{12.42}$$

Fractional melting

Modal
$$\boxed{\frac{C_i^{\text{melt}}}{C_{0\,(i)}^{\text{rock}}} = \frac{1}{D_{0\,(i)}^{\text{rock}}}\ (1 - F)^{\left(\frac{1}{D_{0\,(i)}^{\text{rock}}} - 1\right)}} \tag{12.43}$$

Nomodal
$$\boxed{\frac{C_i^{\text{melt}}}{C_{0\,(i)}^{\text{rock}}} = \frac{1}{D_{0\,(i)}^{\text{rock}}}\ \left(1 - \frac{PF}{D_{0\,(i)}^{\text{rock}}}\right)^{\left(\frac{1}{P} - 1\right)}} \tag{12.44}$$

F is the weight fraction of melt produced in the case of batch melting, and the weight fraction of the melt produced and already removed from the source in the case of fractional melting.

In each of the above cases, the concentration of i in the residual solid can be obtained by solving an appropriate mass balance equation (Allègre and Minister, 1978). Equations for more complex scenarios of partial melting have been discussed, for example, by Hertogen and Gijbels (1976) and Allègre and Minster (1978).

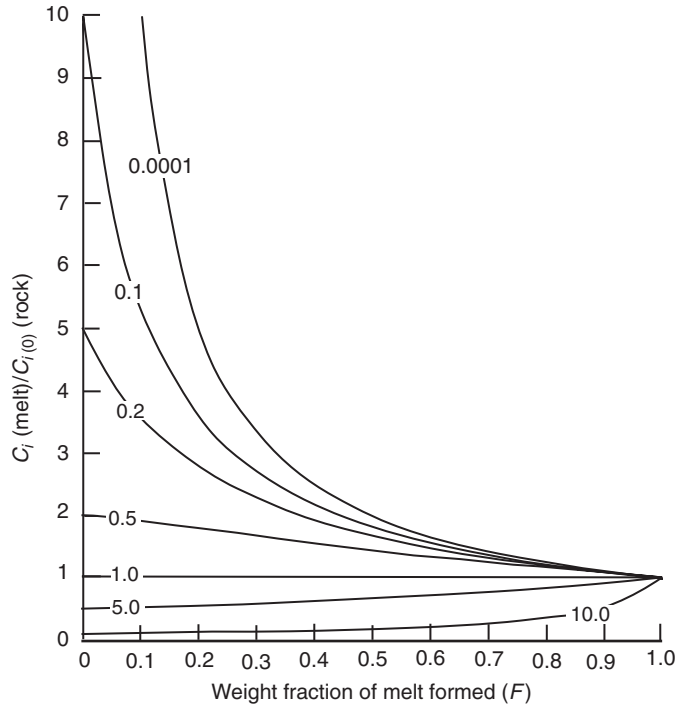

Fig. 12.22 Change in the concentration of an incompatible element, relative to its initial concentration in the source rock, as a function of the weight fraction of melt formed (F) during modal equilibrium (batch) partial melting. The curves are for arbitrarily assumed values (0.0001, 0.2, 0.5, 1.0, 5.0, 10.0) of the bulk distribution coefficient.

In all the four cases stated above, the concentration of a given trace element in the melt relative to the source increases with decreasing value of bulk distribution coefficient for a given degree of partial melting and decreases with increasing degree of partial melting for a given value of the bulk distribution coefficient. In the case of modal batch melting, the simplest case, for very small values of $D_{0(i)}^{\text{rock}}$, equation (12.41) reduces to $C_i^{\text{melt}}/C_{0(i)}^{\text{rock}} = 1/F$, which marks the limit of enrichment of i in the melt for any given degree of batch melting. For very small values of F, equation (12.41) reduces to $C_i^{\text{melt}}/C_{0(i)}^{\text{rock}} = 1/D_{0(i)}^{\text{rock}}$, which represents the maximum possible enrichment of an incompatible element in the melt (or maximum possible depletion of a compatible element in the melt). The concentrations of incompatible elements in the partial melt approach those of the source rock with increasing degree of partial melting and should be the same as in the source rock for 100% melting. The results for modal fractional melting are very similar to that of modal batch melting. A noticeable difference is that, in the range 0–10% partial melting, the changes in element concentrations relative to the original source are more extreme in fractional melting compared to batch melting, although the limiting value of $1/D_{0(i)}^{\text{rock}}$ is the same.

Example 12–1: Calculation of trace element concentrations in a partial melt generated by modal and nonmodal batch and fractional melting

Suppose we are interested in the concentration of the rare earth element Ce, a highly incompatible trace element, in the partial melt formed from an ultramafic mantle source rock composed of three minerals in the following proportion (by weight) – diopside (di) : enstatite (en) : forsterite (fo) = 0.4:0.2:0.4. Phase equilibria in the system di–en–fo indicate that the phases would melt in the proportion 0.7 (di) : 0.2 (en): 0.1 (fo) in the case of nonmodal melting. Our task is to calculate the value of $C_{Ce}^{melt}/C_{0(Ce)}^{rock}$ for modal and nonmodal equilibrium and fractional partial melting for $F = 0.3$, given that the distribution coefficients for Ce for the minerals are: di – 0.10; en – 0.003; and fo – 0.001 (Wilson, 1989, p. 65).

$$D_{0(i)}^{rock} = W_0^{di} K_{D(Ce)}^{di\text{-}melt} + W_0^{en} K_{D(Ce)}^{en\text{-}melt} + W_0^{fo} K_{D(Ce)}^{fo\text{-}melt}$$

$$= (0.4)\,(0.10) + (0.2)\,(0.003) + (0.4)\,(0.001)$$

$$= 0.04 + 0.0006 + 0.0004 = 0.041$$

$$P = p^{di} K_{D(Ce)}^{di\text{-}melt} + p^{en} K_{D(Ce)}^{en\text{-}melt} + p^{fo} K_{D(Ce)}^{fo\text{-}melt}$$

$$= (0.7)\,(0.10) + (0.2)\,(0.003) + (0.1)\,(0.001)$$

$$= 0.07 + 0.0006 + 0.0001 = 0.0707$$

Now let us calculate the $C_{Ce}^{melt}/C_{0(Ce)}^{rock}$ values for $F = 0.3$.
Batch melting:

$$\text{Modal} \quad \frac{C_{Ce}^{melt}}{C_{0\,(Ce)}^{rock}} = \frac{1}{D_{0\,(Ce)}^{rock} + F(1 - D_{0\,(Ce)}^{rock})} = \frac{1}{0.041 + (0.3)\,(1 - 0.041)} = 3.04$$

$$\text{Nomodal} \quad \frac{C_{Ce}^{melt}}{C_{0\,(Ce)}^{rock}} = \frac{1}{D_{0\,(Ce)}^{rock} + F(1 - P)} = \frac{1}{0.041 + (0.3)\,(1 - 0.0707)} = 3.13$$

Fractional melting:

$$\text{Modal} \quad \frac{C_{Ce}^{melt}}{C_{0\,(Ce)}^{rock}} = \frac{1}{D_{0\,(Ce)}^{rock}}\,(1 - F)^{\left(\frac{1}{D_{0\,(Ce)}^{rock}} - 1\right)} = \frac{1}{0.041}(1 - 0.3)^{\left(\frac{1}{0.041} - 1\right)} = 0.0058$$

$$\text{Nomodal} \quad \frac{C_{Ce}^{melt}}{C_{0\,(Ce)}^{rock}} = \frac{1}{D_{0\,(Ce)}^{rock}}\,\left(1 - \frac{PF}{D_{0\,(Ce)}^{rock}}\right)^{\left(\frac{1}{P} - 1\right)} = \frac{1}{0.041}\,\left(1 - \frac{(0.0707)\,(0.3)}{0.041}\right)^{\left(\frac{1}{0.0707} - 1\right)} = 0.0017$$

To predict the change in the melt composition with continued partial melting, we would have to consider the stabiliy relations among the three phases as depicted in an appropriate phase diagram for the di–en–fo system.

12.3.3 Behavior of trace elements during magmatic crystallization

Differentiation of primary magmas on cooling occurs mainly by two processes: (i) liquid immiscibility and (ii) crystallization. *Liquid immiscibility* is the phenomenon of separation of a cooling magma into two or more liquid phases of different composition in equilibrium with each other. Separation of a sulfide liquid in a mafic or ultramafic magma, for example, is believed to be the dominant mechanism in the formation of magmatic nickel–copper sulfide deposits hosted by ultramafic–mafic complexes. Model equations for calculating the concentration of a trace element in the immiscible sulfide liquid have been discussed by Campbell and Naldrett (1979) and Naldrett *et al*. (1984), and summarized in Misra (2000).

Analogous to partial melting, crystallization of magma may be viewed in terms of two end-member models.

(1) *Equilibrium crystallization*, which assumes continuous thermodynamic reequilibration of the crystallized product with the residual (depleted) magma producing crystals without zoning. It is assumed that the cooling is sufficiently slow and the diffusion sufficiently rapid so that the interior of crystals maintain equilibrium with the melt during crystallization.
(2) *Fractional crystallization* (or *Rayleigh fractionation*), which precludes equilibration between the products of crystallization and magma, either because of continuous removal of the products from magma as soon as they are formed or because diffusion in crystals is much slower than in magma. This process is best described by the Rayleigh distillation equation.

Consider the crystallization of a mineral assemblage containing a trace element i from a finite magma reservoir. Assuming that the mineral–magma distribution coefficients remain constant during the crystallization process, equations that may be used to calculate the changing concentration of i in the residual magma relative to the original magma are as follows (Wood and Fraser, 1976; Allègre and Minster, 1978):

Equilibrium crystallization

$$\boxed{\frac{C_i^{res\ magma}}{C_{0\,(i)}^{magma}} = \frac{1}{D_i^{cryst} + F * (1 - D_i^{cryst})}} \qquad (12.45)$$

Fractional crystallization

$$\boxed{\frac{C_i^{res\ magma}}{C_{0\,(i)}^{magma}} = F^{*(D_i^{cryst} - 1)}} \qquad (12.46)$$

where $C_{0(i)}^{\text{magma}}$ is the initial concentration of i in the magma, $C_i^{\text{res magma}}$ is its concentration in the residual magma, F^* is the weight fraction of the original magma remaining (a measure of the degree of crystallization), and D_i^{cryst} is the bulk distribution coefficient of i for the crystallizing mineral assemblage. The calculation of the bulk distribution coefiicient, D_i^{cryst}, is analogous to that of $D_{0(i)}^{\text{rock}}$ (equation 12.30):

$$D_i^{\text{cryst}} = \sum_{\alpha} W_0^{\alpha} \; K_{\text{D}\,(i)}^{\alpha\text{—magma}} \tag{12.47}$$

where W_0^{α} is the weight fraction of crystallizing mineral α and $K_{D(i)}^{\alpha\text{-magma}}$ its crystal–magma distribution coefficient for the element i. For either crystallization model, the smaller the value of the bulk distribution coefficient of a trace element, the greater will be its enrichment in the melt for a given degree of crystallization (Fig. 12.23). A comparison of equilibrium and fractional crystallization for the same element would show that the enrichment of the residual magma in incompatible trace elements is very similar in the two cases up to about $F = 0.25$, but at $F > 0.25$ for incompatible elements and for highly compatible elements the two models differ significantly. In a differentiated suite of igneous rocks, the late differentiates are commonly considerably enriched in highly incompatible elements (such as Li, Ba, Rb, and Pb) and depleted in markedly compatible elements (such as Cr and Ni).

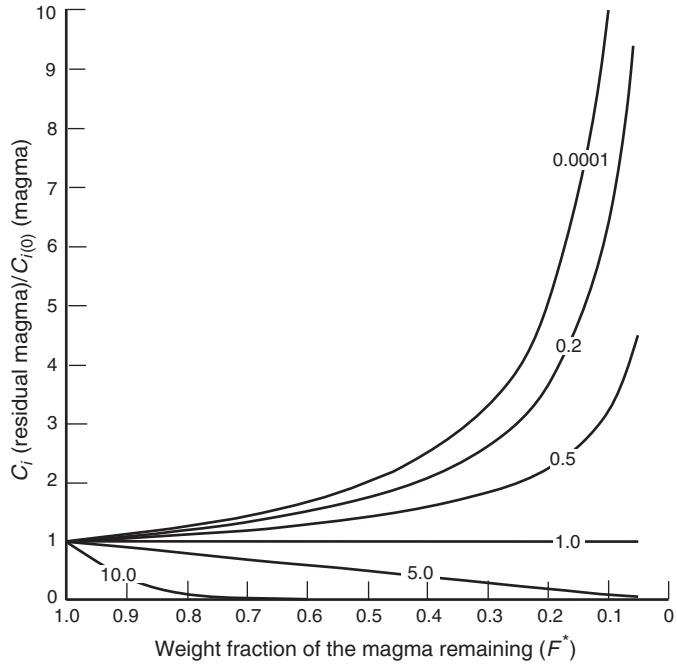

Fig. 12.23 Change in the concentration of an incompatible element, relative to its initial concentration in the source rock, as a function of the weight fraction of melt remaining (F^*) during fractional crystallization. The curves are for arbitrarily assumed values (0.0001, 0.2, 0.5, 1.0, 5.0, 10.0) of the bulk distribution coefficient.

Gravitative settling of crystals to the base of the magma chamber (or flotation to the top, depending on the density of crystals relative to the magma) is no longer considered the dominant mechanism of crystal separation, except perhaps in the case of ultramafic magmas. The evidence now appears to favor *in situ* growth of crystals on the floor and walls of the magma chamber and, to facilitate further crystallization, removal of the depleted magma from contact with the growing crystals by a combination of diffusive and convective processes (Sparks *et al.*, 1984). Equations that describe trace element distributions during *in situ* crystallization have been discussed by Langmuir (1989).

In principle, it should be possible to invert the above equations to calculate the weight proportion of phases crystallizing from a melt for a given degree of fractional crystallization (Allègre and Minister, 1978). At present such calculations are limited because of the lack of high-quality mineral-melt partition coefficient data for many of the elements of interest. In addition, trace element modeling of natural systems is constrained by the problems inherent in the analysis of very small concentrations and the dependence of K_{D} values on the compositions of the phases involved in the crystallization process.

Example 12–2. Crystallization differentiation of oceanic tholeiitic basalts

The average Rb contents of oceanic tholeiitic basalts and oceanic alkalic basalts are 1 and 18 ppm, respectively. The bulk distribution coefficient for Rb in tholeiitic basalt is 0.02, and it is assumed to be constant throughout the crystallization process. Based on the distribution of Rb, could alkalic basalts be a fractional crystallization product of tholeiitic magmas (after Wood and Fraser, 1976)?

The enrichment factor for Rb in alkali basalts (residual magma) relative to tholeiites (original magma) = 18.0 ppm/1 ppm = 18. Let us calculate the degree of crystallization necessary to produce such a residual magma.

Applying the Rayleigh crystallization model, the most favorable condition for enrichment of incompatible elements in the residual magma, the extent of fractional crystallization necessary in this case can be calculated as follows:

$$\frac{C_{\text{Rb}}^{\text{alk basalt magma}}}{C_{\text{Rb}}^{\text{tholeiite magma}}} = F^{*(D_i^{\text{cryst}}-1)} = F^{*(0.02-1)} = F^{*(-\,0.98)} = 18$$

$$F^* = 0.0524$$

$$\text{Equivalent percent crystallization} = (1 - 0.0524) \times 100 = 94.76$$

Applicaton of the equilibrium crystallization yields a similar result:

$$\frac{C_{\text{Rb}}^{\text{alk basalt magma}}}{C_{\text{Rb}}^{\text{tholeiite magma}}} = F^{*(D_i^{\text{cryst}}-1)} = F^{*(0.02-1)} = F^{*(-\,0.98)} = 18$$

$$\frac{C_i^{\text{alk basalt magma}}}{C_{0\,(i)}^{\text{tholeiite magma}}} = \frac{1}{0.02+F^*(1-0.02)} = 18$$

$F^* = 0.037$

Equivalent percent crystallization = $(1 - 0.037) \times 100 = 96.3$

It is difficult to imagine any combination of phases that could be removed from a tholeiitic melt so as to achieve 95–96% crystallization without substantially altering the major element chemistry of the residual liquid. It is, therefore, unlikely that alkali basalts are equilibrium or fractional crystallization products of tholeiitic magmas.

12.3.4 Chemical variation diagrams

A *chemical variation diagram* is a graphical display of compositional variation in a presumably genetically related suite of rocks. Variation diagrams are plotted in terms of abundances or ratios of major or trace elements (or a combination of both) that are relevant to the rocks being investigated. Trends in such diagrams are particularly useful for the interpretation of crystal–liquid fractionation processes, by either partial melting or fractional crystallization, in a cogenetic suite of volcanic igneous rocks. One of the commonly used types in igneous petrology is the *Harker diagram*, in which constituent oxides (in wt%) are plotted against SiO_2 (in wt%), the latter chosen as a measure of the degree of magmatic differentiation. Because SiO_2 tends to be mobile even in weakly altered rocks, other less mobile constituents, such as MgO or Zr, are often preferred as the differentiation index. For a cogenetic differentiated series of rocks, Harker-type variation diagrams may display continuous linear trends or coherent segmented trends marking the so-called *liquid line of descent*, which represents the changing magma composition with fractional crystallization. In general, the inflection point between two adjacent segmented trends marks the onset of crystallization of a new mineral or a group of new minerals. This principle is illustrated in Fig. 12.24 with a hypothetical example. Basaltic magmas, in which the number of crystallizing phases is normally small, frequently display strong inflected trends; intermediate volcanic suites, on the other hand, typically display inflection-free trends in major element variation diagrams, despite wide variation in the crystallizing assemblage (Wilson, 1989).

Variation diagrams with trace elements as variables may also provide useful information about fractional crystallization. For example, trends of decreasing Ni, Cr, and Ti with differentiation through a rock series indicate fractionation of olivine, clinopyroxene, and Fe–Ti oxides, respectively. In such diagrams Zr is often used as a differentiation index.

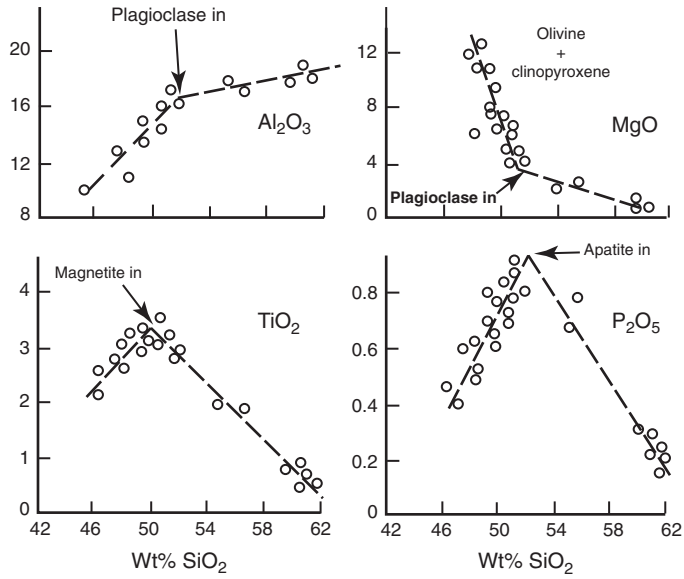

Fig. 12.24 Harker variation diagrams for a suite of cogenetic volcanic rocks related by fractional crystallization of olivine, clinopyroxene, plagioclase, magnetite, and apatite. (From *Igneous Petrogenesis* by Marjorie Wilson, 1989, Fig. 4.7, p. 85, Springer, The Netherlands. Originally published by Chapman and Hall. Reproduced with kind permission from Science+Business Media B.V.)

12.3.5 Rare earth elements

The REEs comprise a coherent group of 15 elements – La (Z = 57), Ce, Pr, Nd, Pm, Sm, Eu, Gd, Tb, Dy, Ho, Er, Tm, Yb, and Lu (Z = 71) – characterized by very similar physical and chemical properties. They all form 3+ cations. Eu also exists as Eu^{2+} in igneous systems, substituting mainly for Ca^{2+} in plagioclase, the Eu^{3+}:Eu^{2+} ratio becoming higher with increasing oxidizing condition, and Ce may be tetravalent under oxidizing conditions.

The REEs in both chondrites and basalts exhibit a sawtooth pattern because of the *Oddo–Harkins effect* (elements with even–odd atomic numbers having higher concentrations than their immediate neighbors with odd atomic number). Normalization of the REE abundances for basalts relative to the abundances in CI chondrite meteorites, believed to be the Earth's parental material, gives smoothed REE patterns that can be compared directly to primordial Earth. The normalization is done by dividing the concentration of each REE by the concentration of the same REE in the chondrite standard. A few examples of chondrite-normalized REE patterns are shown in Fig. 12.25.

Magmas formed by partial melting of upper mantle rocks incorporate REEs depending on their abundances in the source rock and the $D^{\text{mineral–magma}}$ values for the various minerals in the source rock (see section 12.3.2). Therefore, the overall shape of the REE patterns and anomalies associated with individual elements are useful for constraining the source of magma or the participation of specific minerals in

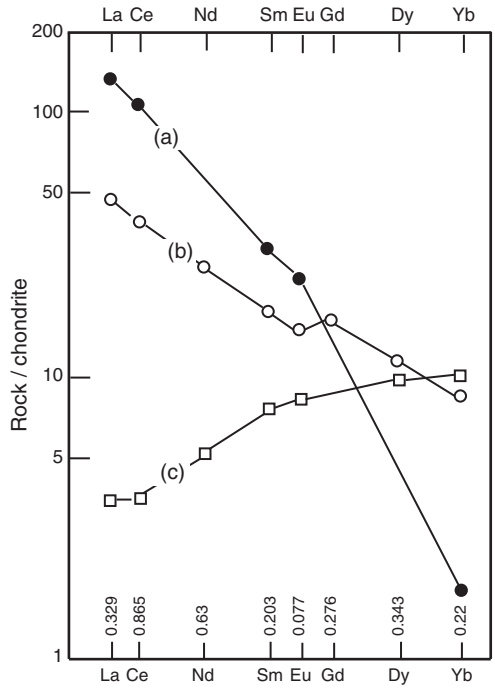

Fig. 12.25 Schematic chondrite-normalized REE patterns for basaltic igneous rocks formed by partial melting of upper mantle rocks. (a) Basalt strongly enriched in light REE, suggesting very small degrees of partial melting or a light-REE enriched source, and very low concentrations of heavy REE, suggesting the presence of residual garnet in the source. (b) Basalt with high concentrations of heavy-REE, suggesting the absence of garnet in the source rock, and a slight negative Eu anomaly indicative of plagioclase crystallization or equilibrium of the partial melt with a plagioclase-bearing mantle source. (c) Basalt showing strong light-REE depletion, suggesting derivation from a light-REE depleted garnet-free source. Chondrite values for normalization, as indicated on the diagram, are from Nakamura (1974). (From *Igneous Petrogenesis* by Marjorie Wilson, 1989, Fig. 2.3, p. 18, Springer, The Netherlands. Originally published by Chapman and Hall. Reproduced with kind permission from Science+Business Media B.V.)

its evolution. For example, garnet has very low $D^{\text{mineral–magma}}$ values for the light REEs and increasingly larger values for heavy REEs (Table 12.7), so that magma generated by partial melting of a garnet-bearing source rock would be depleted in the heavy REEs. On the other hand, $D^{\text{mineral–magma}}$ values for all REEs are less than 0.1 in the case of olivine; thus its presence in the source rock leads to essentially equivalent enrichment of all the REEs. The compatibility of Eu^{2+} with plagioclase, in contrast to low $D^{\text{mineral–magma}}$ values for all other REEs, gives rise to the negative europium anomaly either because Eu^{2+} is retained by plagioclase in the source rock or because of crystallization and removal of plagioclase from the partial melt (Fig. 12.25).

Rare earth elements typically have low solubility in water. So clastic sediments commonly inherit the REE composition of their eroded parents. Consequently, the REE distribution pattern of clastic sediments is a good indication of the composition of the crystalline rock from which the sediments were derived. The interpretation gets complicated if sediments were contributed by more than one parent.

12.4 Geochemical discrimination of paleotectonic settings of mafic volcanic suites

12.4.1 Tectonomagmatic discrimination diagrams

Several studies have shown that modern basaltic rocks erupted in different tectonic settings carry different trace element signatures. For example, island arc basalts are characterized by a selective enrichment in incompatible elements, whereas continental tholeiites contain higher concentrations of K, Rb, Ba, and Th compared to MORB. It is, therefore, reasonable to expect that the tectonic settings of ancient basaltic rocks may be deciphered from their trace element geochemistry, a particularly useful exercise in those cases where the paleotectonic setting is not clear from field relations and petrology. The principle behind all the proposed "*tectonomagmatic discrimination diagrams*" is the comparison of selected trace element concentrations in an ancient basaltic suite with their concentrations in present day analogs from known plate-tectonic settings. Some discrimination diagrams use ratios of incompatible elements for such comparisons in order to overcome the effects of fractionation that occur during partial melting or fractional crystallization. The effectiveness of discrimination diagrams utilizing major elements is limited by the extensive overlap in major element chemistry among MORB, backarc basin tholeiites, and volcanic-arc basalts, and the relative mobility of the major elements during alteration and metamorphism.

Trace elements that can be used for these empirical discrimination diagrams must be relatively immobile during post-crystallization alteration and metamorphism. Elements that commonly best satisfy this requirement are: the REEs (with the possible exception of Ce); HFS elements such as Sc, Y, Zr, Hf, Th, Ti, P, Nb, and Ta; and some other elements such as Cr, Ni, Co, and V. Low field strength elements (Cs, Sr, K, Rb, Ba) are relatively mobile, even during low to moderate temperature alteration by seawater; even HFS elements may be somewhat mobile in fluids at lolw pH and with high F contents (Jiang *et al.*, 2005). In addition, the transition metals Mn, Zn, and Cu tend to be mobile, particularly at high temperatures. Such generalizations are normally valid, but many exceptions have been documented. The samples analyzed must not be much altered, as evidenced by other tests, for example, a high degree of correlation between MgO and Ni as expected in unaltered basaltic rocks. The samples should also be free of phenocrysts and be large enough to overcome the effects of small-scale inhomogeneities.

Since the pioneering work of Pearce and Cann (1973), who proposed a Ti–Zr–Y ternary diagram with distinct

Table 12.8 Tectonomagmatic discrimination diagrams for determining paleotectonic settings of ancient basaltic suites.

Tectonomagmatic discrimination diagram	Tectonic settings to be discriminated	Reference	Comments	
Bivariate	Ti–Zr	OFB–LKT–CAB	Pearce and Cann (1973)	Continental (within-plate) tholeiitic basalts must be screened out before using this diagram for altered volcanics (Floyd and Winchester, 1975)
	Cr–Ti	OFB–LKT	Pearce (1975)	
	(Y/Nb)–TiO_2 (Fig. 12.26d)	Oceanic tholeiites–oceanic alkali basalts–continental tholeiites–continental alkali basalts	Floyd and Winchester (1975)	Useful for discriminating between tholeiitic basalts (Y/Nb > 1; horizontal trend) and alkali basalts (Y/Nb > 1; vertical trend)
	Ni–(Ti/Cr)	OFT–IAT (low-K)	Beccaluva *et al*. (1979)	Only tholeiitic rocks with SiO2 between 40 and 56% were used for this diagram
	Y–Cr (Fig. 12.26b)	MORB–WPB–VAB	Pearce *et al*. (1981)	Effectively discriminates between MORB and VAB
	Zr–Ti (Fig. 12.26a)	MORB–WPB–IAB	Pearce *et al*. (1981)	Considerable overlap among the three fields
	(Nb/Y)–(Ti/Y)	MORB–IAB–WPB	Pearce (1982)	Successfully separates MORB from WPB
	Zr–(Zr/Y) (Fig. 12.26c)	MORB–IAB–WPB	Pearce and Norry (1979)	Effectively discriminates between MORB, IAB, and WPB
Ternary	(Ti/100)–Zr–(Yx3) (Fig. 12.26e)	OFB–LKT–CAB–WPB	Pearce and Cann (1973)	Supposed to be very effective for discriminating WPB, but not according to Holm (1982) The OFB field should also represent all tholeiitic basalts formed in a rifting environment (Floyd and Winchester, 1975)
	(Ti/100)–Zr–(Sr/2)	OFB–LKT–CAB	Pearce and Cann (1973)	Should not be used unless Sr can be shown to be immobile
	(Hf/3)–Th–Ta (Fig. 12.26h)	N-MORB–P-MORB–WPB–DPMB	Wood (1980)	Recognizes different types of MORB, and is supposed to be effective at identifying volcanic-arc basalts. Does not work well according to Thompson *et al*. (1980)
	TiO_2–(MnOx10)–(P_2O_5x10) (Fig. 12.26f)	MORB–IAT–OIT–CAB–OIA	Mullen (1983)	Applicable to basaltic andesites and basalts (45–54% SiO2), and their zeolite to green schist facies metamorphosed products, of oceanic regions. Continental tholeiites overlap portions of all five oceanic fields
	(Nbx2)–(Zr/4)–Y (Fig. 12.26g)	N-MORB–P-MORB WPBA–WPBT–VAB	Meschede (1986)	VAB plot within both WPBT and N-type MORB fields and thus cannot be distinguished from these types. Ancient continental tholeiites which plot in the T–Zr–Y diagram within the MORB/VAB field are clearly distinguished from N-type MORB
Major elements	Statistical analysis of major elements	OFB–LKT–CAB–SHO–WPB	Pearce (1976)	Does not successfully discriminate between ocean-island and continental basalts
	FeO*–MgO–Al_2O_3	Ocean floor and ridge–continental tholeiites–ocean island basalts–orogenic–spreading center islands	Pearce *et al*. (1977)	Based on analysis of subalkaline basaltic–andesitic rocks only (51–56% SiO2), mainly Cenozoic in age. Claims to differentiate between oceanic and continental basalts

CAB = calc-alkaline basalts; CON = continental basalts; DMPB = destructive plate margin basalts; IAB = island-arc basalts; IAT/LKT = island-arc (low-K) tholeiites; MORB = mid-oceanic ridge basalts; N-MORB = "normal" mid-oceanic ridge basalts; P-MORB = plume-type enriched MORB; OFB = ocean-floor basalts; OFT = ocean-floor tholeiites; SHO = shoshonites; OIA = oceanic-island alkalic basalts; OIB = ocean-island basalts; OIT = ocean-island tholeiites; VAB = volcanic-arc basalts; WPB = within-plate basalts (oceanic and continental); WPBA = within-plate basalts alkalic; WPBT = within-plate basalts tholeiitic.
Shoshonite is a volcanic-arc basaltic (trachy-andesitic, alkaline) rock composed of olivine and augite phenocrysts in a groundmass of labradorite with orthoclase rims, olivine, augite, small amount of leucite, and some dark colored glass.

fields for WPB, CAB, IAT, and IAT+MORB, a number of tectonomagmatic discrimination diagrams have been proposed by various authors. A selection of useful discrimination diagrams is summarized in Table 12.8, and some of the more commonly used diagrams are presented in Fig. 12.26. Rollinson (1993) provides a comprehensive discussion of tectonomagmatic discrimination diagrams for basaltic and granitic rocks.

It must, however, be mentioned that this approach by itself is unlikely to provide unequivocal interpretation of the paleotectonic settings, especially for highly altered rocks. The tectonomagmatic discrimination diagrams should be used as a possible clue but not as the conclusive evidence.

12.4.2 *Spider diagrams*

Another method of inferring the tectonic setting of an ancient basaltic suite is to compare its pattern of selected trace element abundances with those of their present-day analogs, both normalized to a common reference material, in known tectonic settings. The elements chosen for generating such patterns, referred to as "*spider diagrams*" (Thompson, 1982), behave incompatibly (i.e., $D_i^{\text{mineral—melt}} < 1$) with respect to a small percentage of melt generated by partial melting. Exceptions to this are Sr, which may be compatible with plagioclase, Y and Yb with garnet, and Ti with magnetite. The order in which the elements are arranged in a spider diagram is somewhat arbitrary, commonly designed to give a smooth pattern for average MORB. Generally, the order is one of decreasing incompatibility from left to right in a four-phase lherzolite (clinopyroxene–orthopyroxene–olivine–garnet) undergoing partial melting.

Normalization concentrations adopted for spider diagrams range from chondritic abundances (e.g., Thompson, 1982; Sun and McDonough, 1989) because of their nearly cosmic composition, to a hypothetical primitive mantle (BSE) composition (e.g., Taylor and McLennan, 1985; Kargel and Lewis, 1993; McDonough and Sun, 1995), to an average MORB composition (Pearce, 1983; Bevins *et al*., 1984). Some of the commonly used normalization values are listed in Table 12.9. Normalization to chondritic values, which have been measured directly, may be preferable to the primordial mantle composition, which is estimated. The normalization values (in ppm) used for Fig. 12.26 are chondritic values from Thompson (1982).

MORB-normalized patterns are particularly useful for comparing the trace element characteristics of different types of basalts. The elements used for MORB-normalized spider diagrams include two groups based on their relative mobility in aqueous fluids: Sr, K, Rb, and Ba are mobile and plot at the left side of the pattern; the remaining elements are immobile. The elements are arranged such that the incompatibility of the mobile and immobile elements increases from the outside to the center of the pattern (Wilson, 1989, p. 21). The shape of these patterns, according

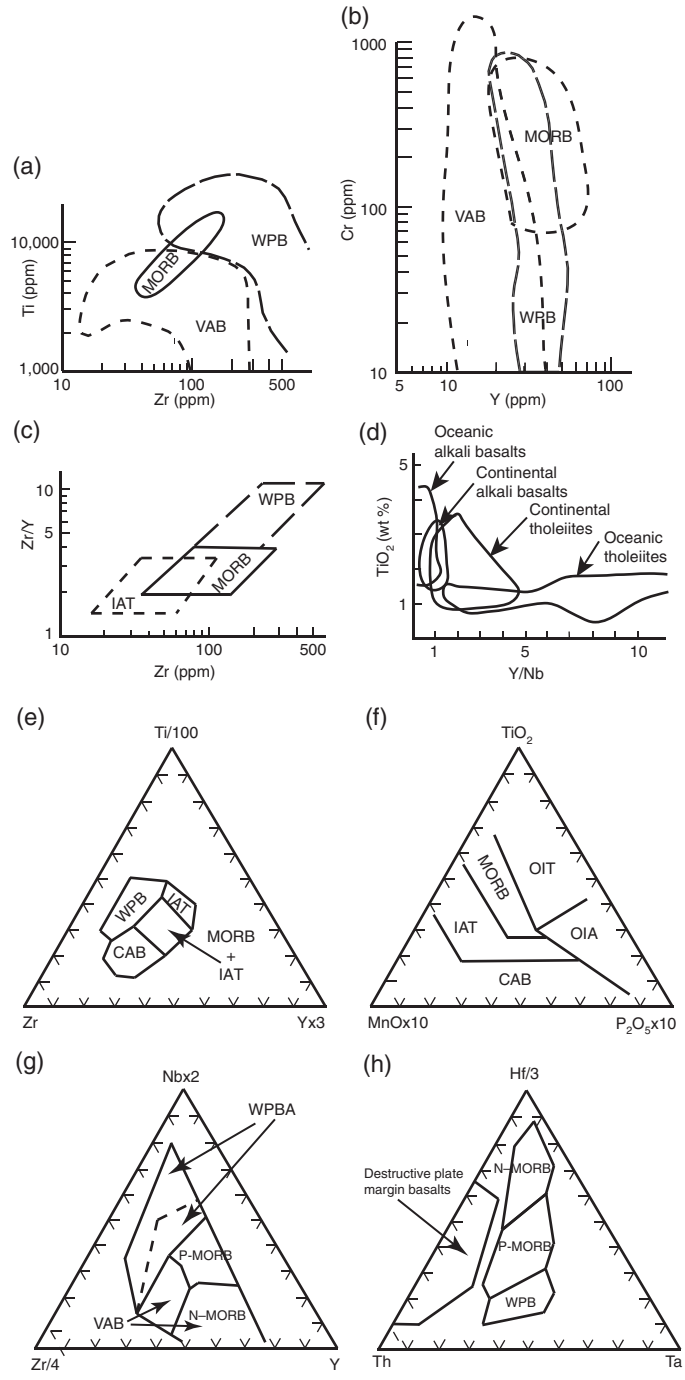

Fig. 12.26 Some commonly used tectonic discrimination diagrams for mafic volcanic rocks: (a) Ti/100–Zr–Yx3 (Pearce and Cann, 1973); (b) TiO_2–MnOx10–P_2O_5x10 (Mullen, 1983); (c) Nbx2–Zr/4–Y (Meschede, 1986); (d) Hf/3–Th–Ta (Wood *et al*., 1979); (e) Zr–Ti (Pearce *et al*., 1981); (f) Y–Cr (Pearce *et al*., 1981); (g) Zr–Zr/Y (Pearce and Norry, 1979); (h) Y/Nb–TiO_2 (Floyd and Winchester, 1975). OFB = ocean-floor basalts; OFT = ocean-floor tholeiites; N-MORB = "normal" mid-oceanic ridge basalts; P-MORB = plume-type enriched MORB; VAB = volcanic arc basalts; IAT/LKT = island arc (low-K) tholeiites; CAB = calc-alkaline basalts; IAB = island arc basalts; SHO = shoshonites. WPB = within-plate basalts (oceanic and continental); CON = continental basalts; WPBA = within-plate basalts alkalic; WPBT = within-plate basalts tholeiitic; OIB = ocean-island basalts; OIT = ocean island tholeiites; OIA = oceanic island alkalic basalts.

Table 12.9 Normalizing values (in ppm) commonly used in the calculation of "spider diagrams."

	Primitive mantle						MORB	
Trace element	**(1)**	**(2)**	**(3)**	**Trace element**	**Chondrite (4)**	**Trace element**	**(5)**	**(6)**
Cs	0.018	0.0131	0.021	Ba	6.90	Sr	120	136
Rb	0.550	0.598	0.600	Rb	0.350	K2O(%)	0.15	0.15.
Ba	5.1	6.41	6.6	Th	0.042	Rb	2	1
Th	0.064	0.0782	0.0795	K	120	Ba	20	12
U	0.018	0.022	0.023	Nb	0.350	Th	0.20	0.20
K	180	232.4	240	Ta	0.020	Ta	0.18	0.17
Ta	0.040	0.0412	0.037	La	0.329	Nb	3.50	2.50
Nb	0.560	0.765	0.658	Ce	0.865	Ce	10	10
La	0.551	0.622	0.648	Sr	11.800	P2O5(%)	0.12	0.12
Ce	1.436	1.592	1.675	Nd	0.630	Zr	90	88
Sr	17.8	20.7	19.9	P	46	Hf	2.40	2.50
Nd	1.067	1.175	1.250	Sm	0.203	Sm	3.50	
P	n.d.	79.4	90	Zr	6.840	TiO2(%)	1.50	1.50
Hf	0.270	0.300	0.283	Hf	0.200	Y	30	35
Zr	8.3	11.47	10.5	Ti	620	Yb	3.40	3.50
Sm	0.347	0.360	0.406	Tb	0.052	Sc	40	
Ti	960	1180	1205	Y	2	Cr	250	290
Tb	0.087	0.0955	0.099	Tm	0.034			
Y	3.4	3.91	4.30	Yb	0.220			
Pb	0.120	0.149	0.150					

Sources of data: (1) Taylor and McLennan (1985); (2) Kargel and Lewis (1993); (3) McDonough and Sun (1995); (4) Thompson (1982); (5) Pearce (1983); (6) Bevins *et al*. (1984).

to Pearce (1983), is not likely to be modified much by variable degrees of partial melting or fractional crystallization, and the patterns may provide constraints on source characteristics.

As an example, spider diagrams for some typical present-day basaltic rocks from known tectonic settings are presented in Fig. 12.27. Note that the patterns are quite distinct. The oceanic basalts (both tholeiitic and alkalic) are characterized by the relatively smooth, convex upward patterns and high degrees of incompatible element enrichment, especially in Nb–Ta, suggesting that the source may be enriched in incompatible elements. The island arc calc-alkaline basalt, on the other hand, is strongly spiked, with a pronounced Nb–Ta trough and a lesser dip for the relatively less incompatible elements. The positive spikes are mostly a consequence of materials added to the mantle source of the basalts by subduction-zone fluids. In contrast, the MORB has a relatively smooth pattern, with the less incompatible elements (such as Zr, Hf, Ti, and Y) more enriched than the more incompatible elements (such as Ba, Rb, Th, and K). There is no known mechanism for producing such a pattern in the large volumes of partial melt generated at mid-oceanic ridges (Nory and Fitton, 1983). The most logical explanation for the MORB pattern is a large degree of partial melting of a source depleted in the more incompatible elements such as K and Rb and, to a lesser extent, Nb and La. The depletion is probably complementary to the formation of continental crust throughout geologic time.

The major limitation of the reliance on spider diagrams to interpret paleotectonic settings is the sensitivity of the patterns to compositional variability within any magma series due to variations in the partial melting process as well as due to external factors such as magma mixing, crustal contamination, and alteration. For instance, the distinctive Nb–Ta trough for calc-alkaline basalt (Fig. 12.27) is also a typical feature of other types of basalts that have experienced crustal contamination.

Spider diagrams, which may be viewed as an extension of REE diagrams (Fig. 12.25), also provide valuable petrogenetic information concerning crystal–magma equilibria. Consider, for example, the pattern for MORB in Fig. 12.27. The enrichment in less incompatible elements such as Zr, Ti, and Y in the magma indicates high degrees of partial melting of the upper mantle source, which can be reconciled with the much lesser enrichment in the highly incompatible elements such as Ba, Rb, and K only if the source of MORB is depleted in these elements. The complementary trace element patterns of the oceanic crust and continental crust (Fig. 12.15) are consistent with the argument that this depletion of the source has resulted from the formation of the continental crust throughout geological time.

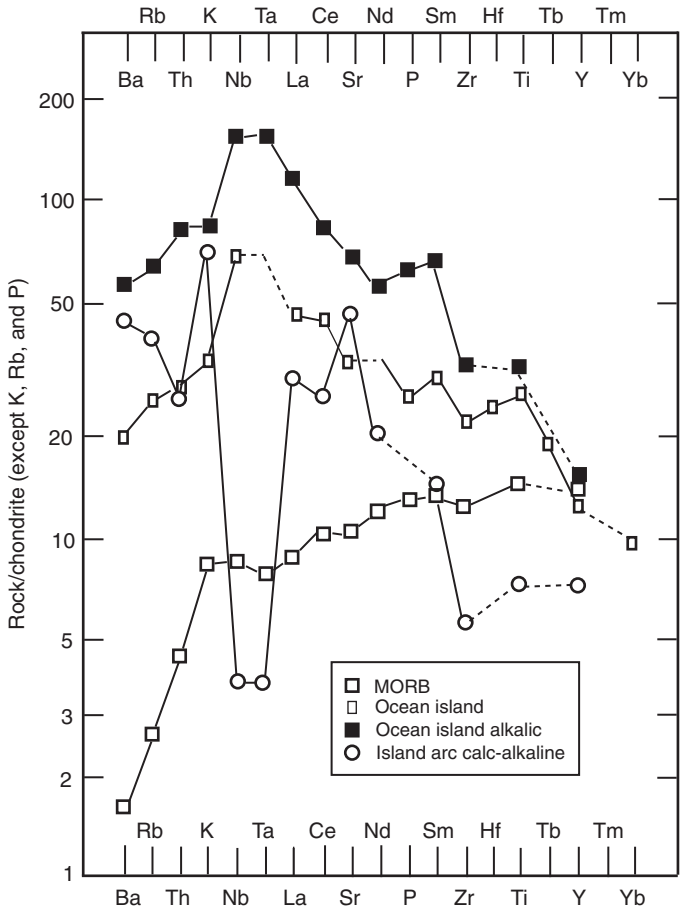

Fig. 12.27 Spider diagrams for typical mid-ocean ridge basalt (MORB), ocean island alkalic basalt, ocean island tholeiite, and island arc calc-alkaline basalt (Basaltic Volcanism Study Project, 1981). The trace elements are arranged in order of decreasing incompatibility. The chondrite normalization factors are from Thompson *et al.* (1984).

12.5 Summary

1. The most popular model for the origin of the universe is the Big Bang theory, which attributes the creation of the universe about 15 Ga to very rapid, exponential expansion of infinitely small, very hot, and infinitely dense matter.
2. The Big Bang created only two elements, hydrogen and helium, in any abundance, and trace amounts of three very light elements – lithium, beryllium, and boron.
3. Elements up to $A = 56$ were formed mostly inside stars by a succession of nuclear fusion processes referred to as hydrogen burning, helium burning, carbon burning, neon burning, oxygen burning, and silicon burning. Heavier elements could be synthesized within stars by a slow neutron capture process known as the *s* process or in the explosive environments, such as supernovae, by a number of processes. Some of the more important of these include: the *r* process, which involves rapid neutron captures; the *rp* process, which involves rapid proton captures; and the *p* process, which involves photodisintegration of existing nuclei.
4. The Solar System formed from a nebula. The formation of the planets within he Solar Nebula involved two important processes: condensation of the nebular gases into solid grains (dust); and accretion of the dust grains into progressively larger solid bodies, reaching dimensions of the order of 1 km (planetesimals). The largest of the planetesimals grew rapidly into planetary embryos of the order of 1000 km in diameter in 0.1–1 million years, and collision of a few dozen of the embryos formed the planets.
5. Age-dating of meteorites indicates that the formation of the planets, including the Earth, occurred at about 4.56 Ga, which is considered the beginning of geologic time.
6. The Earth's interior consists of a series of concentric shells of differing composition and density: the core (outer liquid core and solid inner core), the mantle, and the crust (continental and oceanic).
7. The Earth's differentiation into primitive mantle (bulk silicate Earth, BSE) and metallic core is best explained by magmatic processes operating in a deep high *P*–*T* magma ocean environment.
8. The oldest oceanic crust is only about 200 Ma old. The earliest crust probably was basaltic in composition (with significant amounts of komatiite?) formed by magmatic processes and was recycled the same way as the modern oceanic crust, but there are no remnants of the earliest oceanic crust. The oldest continental crust material identified so far is in the form of ~4.4-Ga-old detrital zircon crystals in metamorphosed sediments. The earliest continental crust must have formed by partial melting of the primitive mantle, with incompatible elements (such as Cs, Rb, K, U, Th, and La) segregated into the crust-forming partial melts. The continental crust appears to have grown episodically, with at least 60% of the crust emplaced by 2.7 Ga.
9. Primary magmas generated by partial melting of upper mantle rocks, dominantly resulting from decompression, comprise three major magma series – tholeiitic, calc-alkaline, and alkalic – each of which spans a genetically related spectrum of mafic to felsic rocks.
10. Trace element characteristics of primary magmas are governed by the composition of the parent material, degree of partial melting, mineral–melt bulk distribution coefficients of the elements, and whether the melting was an equilibrium or fractional (Rayleigh) process. The concentration of a given trace element in the melt relative to the source increases with decreasing value of bulk distribution coefficient for a given degree of partial melting and decreases with increasing degree of partial melting for a given value of the bulk distribution

coefficient. Behavior of trace elements during crystallization can also be modeled as an equilibrium or fractional process.

11. Crystal–liquid fractionation proceses, by either partial melting or crystallization, in a cogenetic volcanic suite can be interpreted from trends in chemical variation diagrams.
12. Incompatible and immobile trace elements, including REEs, in unaltered (or only slightly altered) and genetically related basaltic suites are useful for recognition of their paleotectonic settings. Tools commonly used for this purpose include empirical tectonomagmatic discrimination diagrams and "spider diagrams."

12.6 Recapitulation

Terms and concepts

Asthenosphere
Big Bang theory
Bulk distribution coefficient
Bulk silicate Earth (BSE)
Chemical variation diagram
Compatible elements
Continental crust
Core
Doppler effect
Enrichment factor
Equilibrium crystallization
Equilibrium (batch) partial melting
Fractional crystallization
Fractional partial melting
Giant impact hypothesis
Harker diagram
Heterogeneous accretion
Ionic potential
Liquidus
Incompatible elements
In situ crystallization
Homogeneous accretion
LIL elements
Liquid immiscibility
Liquid line of descent
Lithosphere
Magma ocean
Magma series
Mantle
Meteorites
Modal partial melting
Moho
Neutron capture
Nonmodal partial melting
Planetesimals
Plate tectonics
p process
Primitive mantle
Nucleosynthesis
Oceanic crust
Pyrolite
Rayleigh equation
r process
rp process
s process
Solar Nebula
Solar System
Solidus
Spider diagram
Tectonomagmatic discrimination diagram

Computation techniques

- Concentration of incompatible trace elements in melts formed by partial melting or in melts remaining during crystallization of a melt (magma).
- Harker-type variation diagrams.
- REE patterns.
- Tectonomagmatic discrimination diagrams.
- Chondrite-normalized spider diagrams.

12.7 Questions

1. Construct a chart showing the importants events, in chronological order, related to the evolution of the Earth during the first billion years or so after its birth.
2. In the Sun's core, each second about 700,000,000 tons of hydrogen are converted to about 695,000,000 tons of helium, and the excess mass is converted into energy. Calculate the energy output per second by this process of thermonuclear fusion, using the famous Einstein equation $E = mc^2$.
3. Show that the predominant form of hydrogen gas at the Sun's surface ($T = 5800$ K, $P = 1$ bar) is atomic hydrogen (H), not molecular hydrogen (H_2). The value of the equilibrium constant for the reaction $H_2 \Leftrightarrow H + H$ is given by $\log K_T = 6.16 - 23{,}500/T$ (T in Kelvin) over the temperature range 1000–4000 K. Assume the gases to be ideal, and $P_H = P_{H_2} = 1$ bar.
4. Extract from Appendix 5 the standard free energy data for the oxides and sulfides of the following elements:

   Ca, Mg, Al, Ti, Mn, Si, Mn, K, Na, Sn, Zn, U, W, Mo, Co, Cu, Ni, Pb

   Can you separate the lithophile elements from the chalcophile elements on the list based on free energy of formation? Use an appropriate plot (or plots) to illustrate your conclusion.

5. Consider equilibrium partial melting of a gabbroic source rock composed of 50% plagioclase, 35% clinopyroxene, and 15% olivine by volume. Assume the melting to be modal and the densities of the minerals (in g cm^{-3}) as follows: olivine – 3.6; clinopyroxene – 3.4; and plagioclase – 2.7. Using the distribution coefficient values given in Table 12.9. Construct a graph showing the variation of $C_i^{melt}/C_{0\ (i)}^{rock}$ in the partial melt for the incompatible trace element Rb as a function of F. What is the enrichment factor for Rb in the melt if the degree of partial melting is 1%? [Hint: Remember to convert volume proportion of the minerals to weight fractions].
6. Construct graphs for bulk distribution coefficient values of 0, 0.1, 0.5, 1.0, and 2.0 to show the change in the concentration of a species *i* in the partial melt relative to the source rock ($C_i^{melt}/C_{0\ (i)}^{rock}$) as a function of the fraction of melt remaining (F) for (i) equilibrium crystallization and (ii) fractional crystallization. Comment on the differences, if any, between the two cases.
7. If weighted mean bulk crystal–melt distribution coefficients (D_0) for eclogite (garnet–clinopyroxene) assemblages are taken as 2.0 for Yb and 0.1 for K^+, then:
   (a) How much crystallization of eclogite would be necessary to increase the K^+ content of residual liquids by a factor of two, assuming Rayleigh fractionation?
   (b) How much would the Yb content of the melts have decreased during this process?
   (c) Repeat the calculations assuming equilibrium crystallization.
   (After Wood and Fraser, 1976.)
8. Calculate the REE patterns, normalized to chondrite, for 10% modal batch melting of a garnet peridotite (typical mantle rock) with the following mineralogic composition (in wt%): olivine – 55; orthopyroxene – 20; clinopyroxene – 20; and garnet – 5. Assume that the REE abundances in the garnet peridotite are twice the abundances in chondrites. The chondrite abundances (in ppm) are: La – 0.315; Ce – 0.813; Nd – 0.597; Sm – 0.192; Eu – 0.772; Dy – 0.325; Yb – 0.208; Lu – 0.0323. The mineral–melt distribution coefficients of the REE are listed below:

Element	Orthopyroxene	Clinopyroxene	Plagioclase	Olivine	Garnet
La	0.002	0.066	–	0.002	0.20
Ce	0.003	0.100	0.023	0.003	0.28
Nd	0.006	0.500	0.023	0.003	0.068
Sm	0.014	1.700	0.024	0.003	0.29
Eu^{2+}	0.023	1.600	0.393	0.005	0.49
Yb	0.110	0.715	0.006	0.009	11.5
Lu	0.110	0.610	0.005	0.009	11.9